



8-1991

## **Studies of Mathematical Modelling and Experimental On-line Measurement for the Tubular Film Blowing Process**

Cheng-Chien Liu

*University of Tennessee - Knoxville*

Follow this and additional works at: [https://trace.tennessee.edu/utk\\_gradthes](https://trace.tennessee.edu/utk_gradthes)

 Part of the [Polymer Science Commons](#)

---

### **Recommended Citation**

Liu, Cheng-Chien, "Studies of Mathematical Modelling and Experimental On-line Measurement for the Tubular Film Blowing Process. " Master's Thesis, University of Tennessee, 1991.  
[https://trace.tennessee.edu/utk\\_gradthes/764](https://trace.tennessee.edu/utk_gradthes/764)

This Thesis is brought to you for free and open access by the Graduate School at TRACE: Tennessee Research and Creative Exchange. It has been accepted for inclusion in Masters Theses by an authorized administrator of TRACE: Tennessee Research and Creative Exchange. For more information, please contact [trace@utk.edu](mailto:trace@utk.edu).

To the Graduate Council:

I am submitting herewith a thesis written by Cheng-Chien Liu entitled "Studies of Mathematical Modelling and Experimental On-line Measurement for the Tubular Film Blowing Process." I have examined the final electronic copy of this thesis for form and content and recommend that it be accepted in partial fulfillment of the requirements for the degree of Master of Science, with a major in Polymer Engineering.

Joseph E. Spruiell, Major Professor

We have read this thesis and recommend its acceptance:

Donald C. Bogue, John F. Fellers

Accepted for the Council:

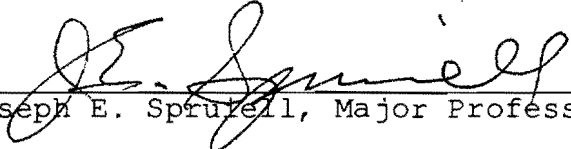
Carolyn R. Hodges

Vice Provost and Dean of the Graduate School

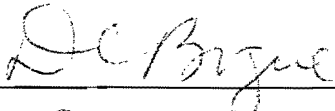
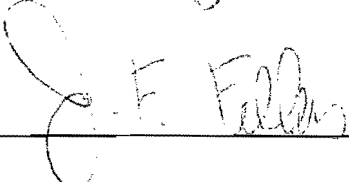
(Original signatures are on file with official student records.)

To the Graduate Council:

I am submitting herewith a thesis written by Cheng-Chien Liu entitled "Studies Of Mathematical Modelling And Experimental On-line Measurement Techniques For The Tubular Film Blowing Process." I have examined the final copy of this thesis for form and content and recommend that it be accepted in partial fulfillment of the requirements for the degree of Master of Science, with a major in Polymer Engineering.

  
\_\_\_\_\_  
Joseph E. Sprutell, Major Professor

We have read this thesis  
and recommend its acceptance:

  
\_\_\_\_\_  
  
\_\_\_\_\_

Accepted for the Council:

  
\_\_\_\_\_  
Associate Vice Chancellor  
and Dean of The Graduate School

STATEMENT OF PERMISSION TO USE

In presenting this thesis in partial fulfillment of the requirements for a Master's degree at The University of Tennessee, Knoxville, I agree that the Library shall make it available to borrowers under rules of the Library. Brief quotations from this thesis are allowable without special permission, provided that accurate acknowledgment of the source is made.

Permission for extensive quotation from or reproduction of this thesis may be granted by my major professor, or in his absence, by the Head of Interlibrary Services when, in the opinion of either, the proposed use of the material is for scholarly purposes. Any copying or use of the material in this thesis for financial gain shall not be allowed without my written permission.

Signature Wang-Chuan Lin

Date July 18 1971

STUDIES OF MATHEMATICAL MODELLING AND  
EXPERIMENTAL ON-LINE MEASUREMENT TECHNIQUES  
FOR THE TUBULAR FILM BLOWING PROCESS

A Thesis

Presented for the

Master of Science

Degree

The University of Tennessee, Knoxville

Cheng-Chien Liu

August 1991

Dedicated to My Parents

Mr. Liang-Sheng Liu (劉亮生)

and

Mrs. Pi-Yun Tsai (蔡碧雲)

## ACKNOWLEDGMENTS

I wish to express my deepest gratitude to my major professor, Joseph E. Spruiell, for his support and guidance in the preparation of this thesis. Special thanks go also to Professor Donald C. Bogue for his invaluable advice and encouragement in this research as well as his serving on my committee. Appreciation is also extended to Professor John F. Fellers, who served on my committee.

Also the author thanks the Dow Chemical Company for financial support and also for the supply of experimental materials and information. Finally, thanks are offered to the staffs of the electronics and machine shops for their help in the experimental work.

Furthermore, I express my sincere appreciation to my friends Jianguo Zhou and Shao-Fang Huang for their assistance and encouragement throughout my graduate studies.

## ABSTRACT

An experimental and analytical study of the process of blown film extrusion was carried out. On-line measuring techniques were used to follow the dynamics and temperature profiles occurring in the process. The applicability of a mathematical model which includes a non-isothermal crystallization rate equation was tested. Subsequently, a new simplified model derived from a modified force balance was proposed and examined.

Linear low density polyethylene, LLDPE, (melt flow index = 1.0) provided by Dow Chemical Company was used in the experimental part of the study. On-line measurements for radius, thickness, velocity and temperature as a function of distance from the extrusion die were carried out, and their reliability was examined. The results indicated that these measuring techniques were sufficiently accurate to make the collection of on-line data a useful analytical tool. The measured profiles of radius, thickness, velocity and temperature were used to test the theoretical model for the tubular film blowing process.

The apparent elongational viscosity, a key parameter for the theoretical simulation, was estimated and calculated from experimental data taken on a melt spinline and an inversion



procedure developed for obtaining apparent elongational viscosities for melt spinning. This gave a Newtonian, temperature-dependent apparent viscosity equation. The heat transfer coefficient was estimated from measured temperature profiles on the blown film process.

A computer simulation for semi-crystalline materials was carried out using the mathematical analysis for film blowing which appears in the literature plus a non-isothermal crystallization rate equation. The analysis was carried out by using the fourth-order Runge-Kutta method to solve the resulting differential equations. The predicted results were in qualitative agreement only with the experimental data. At the same time, several unexpected phenomena appeared in the simulation. Some of them have also been reported in the previous literature, but still no satisfactory interpretation is available.

A modified physical approach based on a force balance led to the derivation and proposal of a new simplified model. From this modified analysis, an important and useful relationship between the external forces (i.e., the net take-up force and the inflation pressure) and the variation of radius and thickness of the bubble were determined. Based on the same initial conditions as that of the original model, the new model gave predictions which were in fair quantitative agreement with the on-line measurements.

Finally, it was also found that the development of crystallinity strongly influences the final values of radius and thickness of the tubular film, two of the important specifications in industrial film processing. In other words, the effect of crystallization is so significant that it should not be neglected in modelling the tubular film blowing process.

## TABLE OF CONTENTS

CHAPTER	PAGE
1. INTRODUCTION .....	1
2. LITERATURE REVIEW.....	5
2.1 Tubular Film Blowing Process .....	5
2.2 Kinematics .....	7
2.3 Dynamics .....	13
2.4 Rheology .....	17
<u>Influence of Molecular Structure on</u> <u>Rheological Performance</u> .....	17
<u>Rheological Modelling</u> .....	20
2.5 Energy Balance .....	23
<u>Heat Transfer Coefficient</u> .....	25
2.6 Crystallization Kinetics .....	28
<u>Nucleation and Growth Under Isothermal</u> <u>Condition</u> .....	28
<u>Overall Transformation Analysis Under</u> <u>Isothermal Condition</u> .....	30
<u>Non-Isothermal Crystallization</u> .....	31
<u>Stress-Induced Crystallization</u> .....	32
2.7 Orientation and Structure Development in Film Blowing Process .....	34
2.8 Instabilities in Tubular Film Blowing ....	36
2.9 Mathematical Modelling of Tubular Blown Film Extrusion .....	38
<u>System Equations of Mathematical</u> <u>Model</u> .....	38

CHAPTER	PAGE
2. (Continued)	
<u>Computer Simulation Based on Various Rheological Models</u> .....	41
3. EXPERIMENTAL MATERIALS, EQUIPMENT, PROCEDURES AND DATA ANALYSIS .....	42
3.1 Resin Identification .....	42
3.2 Resin Processing .....	42
<u>Equipment of Tubular Blown Film Extrusion</u> .....	42
<u>Operating Procedure and Processing Condition</u> .....	46
3.3 On-line Measurement and Data Collection .....	48
<u>Radius</u> .....	48
<u>Thickness</u> .....	50
<u>Velocity</u> .....	52
<u>Temperature</u> .....	56
<u>Inflation Pressure</u> .....	75
<u>Mass Flow Rate</u> .....	77
4. RESULTS AND DISCUSSION .....	78
4.1 On-line Measurement .....	78
<u>Radius</u> .....	78
<u>Velocity</u> .....	81
<u>Thickness</u> .....	84
<u>Temperature</u> .....	88
<u>Overview of On-line Data in the Blown Film Extrusion</u> .....	104

## 4. (Continued)

4.2	Development of Equations for Viscosity and Heat Transfer Coefficient .....	104
	<u>Equation of Viscosity</u> .....	106
	<u>Heat Transfer Coefficient</u> .....	111
4.3	Mathematical Modelling for Tubular Film Blowing Process .....	113
	<u>Continuity Equation</u> .....	114
	<u>Force Balance</u> .....	115
	<u>Energy Balance</u> .....	118
	<u>Viscosity Equation</u> .....	119
	<u>Crystallization Kinetics</u> .....	121
	<u>Numerical Procedures</u> .....	124
	<u>Comparison of Mathematical Prediction and On-line Measurements</u> .....	125
	<u>Behavior of the Mathematical Model for Various Choices of the Parameters</u> .....	131
4.4	Proposed Equations for the Simulation of Tubular Film Blowing Process .....	141
	<u>A Modified Approach to Describe Film Blowing Process</u> .....	141
	<u>Numerical Procedure</u> .....	147
	<u>Comparison of New Mathematical Prediction and On-line Measurements</u> ....	148
	<u>Characteristics of the New Equations</u> ...	154
	<u>Comparison of the Modified Model and the Original One</u> .....	162

CHAPTER	PAGE
4. (Continued)	
4.4 (Continued)	
<u>Predictions of the New Mathematical Model</u> .....	164
5. SUMMARY AND CONCLUSIONS .....	189
<u>Experimental</u> .....	189
<u>Mathematical Analysis</u> .....	190
LIST OF REFERENCES .....	193
VITA .....	202

LIST OF TABLES

TABLE		PAGE
3-1	Identification and properties of linear low density polyethylene .....	43
3-2	Summary of the processing conditions for LL1 .....	47
3-3	Comparison of the measured diameters by the video camera technique and that by a direct measurement .....	51
3-4	Comparison of the measured velocities by the video camera tracing technique and that by the other direct measurements .....	55
3-5	Comparison of the measured temperatures by the on-line technique with that by a thermocouple .....	76

## LIST OF FIGURES

FIGURE		PAGE
2-1	Blown film extrusion process .....	6
2-2	Coordinate systems of a tubular film .....	9
3-1	Schematic diagram of the annular die .....	45
3-2	Video camera system for on-line measurement in the tubular film blowing process .....	49
3-3	Flow chart of the calculation procedures for the on-line velocity profile .....	54
3-4	Schematic diagram of the total thermal radiant energy received by the detector of thermal imaging system .....	59
3-5	$F_e$ -values for different temperatures at the fixed bandwidth (from 2.0 to 5.6 $\mu\text{m}$ ) .....	66
3-6	Schematic diagram of on-line temperature measurement in the tubular film blowing process .....	68
3-7	Flow chart of the procedures for determining on-line temperatures of the film .....	71
3-8	Experimental setup for the test of the on-line temperature measuring techniques .....	73
3-9	Relationship between the measured total radiation energy and the radiation energy of the black body for two static plain films .....	74
4-1	On-line measured radius profile of the bubble and a comparison with the directly measured final diameter .....	80
4-2	On-line measured travelling time interval of the mark for each measured position .....	82
4-3	Relationship between the distance and the time interval beyond the position at $Z = 13.5 \text{ cm}$ .....	83



FIGURE	PAGE
4-4 On-line measured velocity profile of the tubular film and a comparison with the directly measured data .....	85
4-5 Calculated thickness profile of the film by basing on the on-line results and a comparison with the directly measured data .....	87
4-6 Relationship between the measured total radiation energy and the radiation energy of the black body at the positions of $Z = 5.6, 8.6, 11.6$ cm, respectively .....	89
4-7 Relationship between the measured total radiation energy and the radiation energy of the black body at the positions of $Z = 14.6, 17.6, 20.6$ cm, respectively .....	90
4-8 Relationship between the measured total radiation energy and the radiation energy of the black body at the positions of $Z = 23.6, 29.6, 32.6$ cm, respectively .....	91
4-9 Apparent transmissivity profile of the bubble along the machine direction .....	92
4-10 Combination of the profile of the on-line thickness and the apparent transmissivity .....	93
4-11 Emissivity profile of the film along the machine direction .....	96
4-12 Relationship between the emissivity and the thickness of LL1 .....	97
4-13 Values of emissivity under the condition of constant thickness .....	98
4-14 Values of the y-axis intercept from the regression analysis with respect to each measured position .....	100
4-15 Measured apparent black body temperatures of the environment along the machine direction .....	101
4-16 On-line measured temperature profile of the film along the machine direction .....	103

FIGURE	PAGE
4-17	Combination of the profiles of on-line radius, thickness, velocity and temperature, and the experimentally observed frost line ..... 105
4-18	On-line measured temperature profile in the melt spinning process of LL1 ..... 108
4-19	On-line measured diameter profile in the melt spinning process of LL1 ..... 109
4-20	Apparent elongational viscosity calculated from the inversion procedure for LL1 in the melt spinning process ..... 110
4-21	Apparent heat transfer coefficient calculated from the inversion procedure for the tubular film blowing process ..... 112
4-22	Comparison of the predicted and experimental radius profiles ..... 126
4-23	Comparison of the predicted and experimental thickness profiles ..... 127
4-24	Comparison of the predicted and experimental temperature profiles ..... 128
4-25	Comparison of the predicted and experimental velocity profiles ..... 129
4-26	Theoretically predicted on-line crystallinity profile ..... 130
4-27	Comparison of the predicted radius profiles for different $F_L$ values ..... 133
4-28	Comparison of the predicted radius profiles for different $\Delta P$ values ..... 134
4-29	Comparison of the predicted radius profiles for different $T_0$ values ..... 135
4-30	Comparison of the predicted radius profiles for different $a$ values ..... 136
4-31	Comparison of the predicted radius profiles for different $b$ values ..... 137

FIGURE	PAGE
4-32 Experimentally observed relationship of $\Delta P$ and blow-up ratio .....	140
4-33 Schematic diagram of the modified physical approach to describe the tubular film blowing process .....	142
4-34 Comparison of the radius profile predicted by the proposed model with that from experimental measurement .....	149
4-35 Comparison of the thickness profile predicted by the proposed model with that from experimental measurement .....	150
4-36 Comparison of the temperature profile predicted by the proposed model with that from experimental measurement .....	151
4-37 Comparison of the velocity profile predicted by the proposed model with that from experimental measurement .....	152
4-38 On-line crystallinity profile theoretically predicted by the proposed model .....	153
4-39 Radius profiles of the three critical cases of $F/\Delta P$ theoretically predicted by the proposed model .....	156
4-40 Thickness profiles of the three critical cases of $F/\Delta P$ theoretically predicted by the proposed model .....	157
4-41 Temperature profiles of the three critical cases of $F/\Delta P$ theoretically predicted by the proposed model .....	158
4-42 Velocity profiles of the three critical cases of $F/\Delta P$ theoretically predicted by the proposed model .....	159
4-43 Crystallinity profiles of the three critical cases of $F/\Delta P$ theoretically predicted by the proposed model .....	160

FIGURE	PAGE
4-44 Comparison of the radius profiles predicted by the original model and by the proposed model under the condition of $\Delta P = 0$ .....	163
4-45 Comparison of the predicted radius profiles by the proposed model for different F values .....	166
4-46 Comparison of the predicted thickness profiles by the proposed model for different F values .....	167
4-47 Comparison of the predicted temperature profiles by the proposed model for different F values .....	168
4-48 Comparison of the predicted crystallinity profiles by the proposed model for different F values .....	169
4-49 Comparison of the predicted radius profiles by the proposed model for different $\Delta P$ values .....	170
4-50 Comparison of the predicted thickness profiles by the proposed model for different $\Delta P$ values .....	171
4-51 Comparison of the predicted temperature profiles by the proposed model for different $\Delta P$ values .....	172
4-52 Comparison of the predicted crystallinity profiles by the proposed model for different $\Delta P$ values .....	173
4-53 Comparison of the predicted radius profiles by the proposed model for different $T_0$ values .....	175
4-54 Comparison of the predicted thickness profiles by the proposed model for different $T_0$ values .....	176

FIGURE	PAGE
4-55 Comparison of the predicted temperature profiles by the proposed model for different $T_0$ values .....	177
4-56 Comparison of the predicted crystallinity profiles by the proposed model for different $T_0$ values .....	178
4-57 Comparison of the predicted radius profiles by the proposed model for different $b$ values .....	180
4-58 Comparison of the predicted thickness profiles by the proposed model for different $b$ values .....	181
4-59 Comparison of the predicted temperature profiles by the proposed model for different $b$ values .....	182
4-60 Comparison of the predicted crystallinity profiles by the proposed model for different $b$ values .....	183
4-61 Comparison of the predicted radius profiles by the proposed model for different $K$ values .....	184
4-62 Comparison of the predicted thickness profiles by the proposed model for different $K$ values .....	185
4-63 Comparison of the predicted temperature profiles by the proposed model for different $K$ values .....	186
4-64 Comparison of the predicted crystallinity profiles by the proposed model for different $K$ values .....	187

## CHAPTER 1

### INTRODUCTION

The tubular film blowing process is becoming more and more important in the polymer processing industry for producing thin thermoplastic films. The existing blown film lines number about 2000 in North America, and over 80 new processing lines are built every year; that is, there is a 4% annual increase of the present blown film market [1]. The reason why blown film extrusion represents such a developing potential is that tubular film has better physical properties than that of a film produced by the other techniques of fabrication, such as, casting of film. The better performance of blown film is mainly due to its biaxially oriented molecular structure. For example, for the same kind of material, the thickness of a cast film, without being re-oriented, is required to be twice that of a blown film to achieve the same performance [2]. Thus, in order to obtain a further and better understanding of the tubular film blowing process, an experimental on-line study and theoretical analysis are necessary as well as important.

In the past 20 years, a mathematical description, which was first established by Pearson and Petrie [3,4] then

developed by other investigators [5,6], was widely used in the analysis of the blown film process. In the same period, various experimental observations and measuring techniques were reported [7-17]. However, few investigations provided a complete picture of the theoretical as well as experimental aspects of the process. This is probably due to the high complexity of the experimental data collection and the mathematical simulation for this process. Thus, the purpose of the present research is to begin the establishment of a complete on-line experimental database to test and improve the mathematical model of the film blowing process. The main features of this study that distinguish it from the others are stated in the following paragraphs.

(1) Since polyethylenes, which are the most frequently used resins in blown film extrusion, are semi-crystalline polymers, the influence of crystallization while processing must be included. Therefore, a non-isothermal crystallization kinetic equation was used as one of the governing system equations in simulating the film blowing process. This aspect has not been treated adequately in previous literature, which often has simply introduced the crystallization as an afterthought [6].

(2) Because about 70% of linear low density polyethylene (LLDPE) is used in film production [18] and the tubular film

blowing process is a major application for it, LLDPE was chosen as the experimental material in this study.

(3) Since the key material function, the viscosity equation, and the key processing parameter, the heat transfer coefficient, were not well established in most of the earlier literature of mathematical simulation [4,5,10,19-21], the non-isothermal apparent viscosity equation and heat transfer coefficient were generated and estimated from the processing experiments. This provides reasonable values of these important parameters for the present material and experimental conditions.

(4) Based on the above estimated material and processing parameters, a computer simulation including a non-isothermal crystallization rate equation was carried out. Comparisons between the experimental data and the simulated results were made. However, only qualitative agreement was shown in this comparison. A large quantitative discrepancy existed between the experimental observation and theoretically predicted results. Furthermore, after the behavior of the mathematical model appearing in the existing literature was carefully examined, an unexpected effect of the inflation pressure on the radius of the bubble was also found.

(5) Some unsatisfactory results which are similar to the above phenomenon can be found in earlier literature results [5,6,20]. Thus, it seemed necessary to modify the original



model. Hence, a simplified mathematical model which was derived from a modified physical approach was proposed. Also, the results predicted by this proposed model were computed and presented. The evidence showed that the proposed model with the non-isothermal crystallization rate equation provided a huge improvement in simulating the film blowing process for semi-crystalline materials.

(6) Based on the proposed model, the influences of the material parameters (such as the viscosity and the crystallization rate) and the processing parameters (such as the take-up force, inflation pressure and extrusion temperature) on the radius, thickness, temperature and crystallinity of the tubular film were discussed in detail.

## CHAPTER 2

### LITERATURE REVIEW

#### 2.1 Tubular Film Blowing Process

The tubular film blowing process is one of the most important polymer processes and quite complex because of the polymeric melt being subjected to a complicated stress field. A sketch of the blown film process is shown as Figure 2-1. The polymer melt is extruded through an annular slit die by an extruder. The molten polymer exits from the die and is formed into a tubular shape just above the die exit. This tubular melt is drawn upward by a take-up device. At the same time, air from the center of the die is introduced into this melt tube in order to inflate it to form a bubble of thin film. The air being blown into the bubble is adjustable to control the inside pressure, i.e., the pressure difference across the film.

An air cooling ring is installed around the bubble to cool and solidify the tubular film. Thus, the height of frost line (i.e., the position where the melt becomes solidified) is controlled by adjusting the velocity of cooling air which blows both perpendicular and parallel to the machine

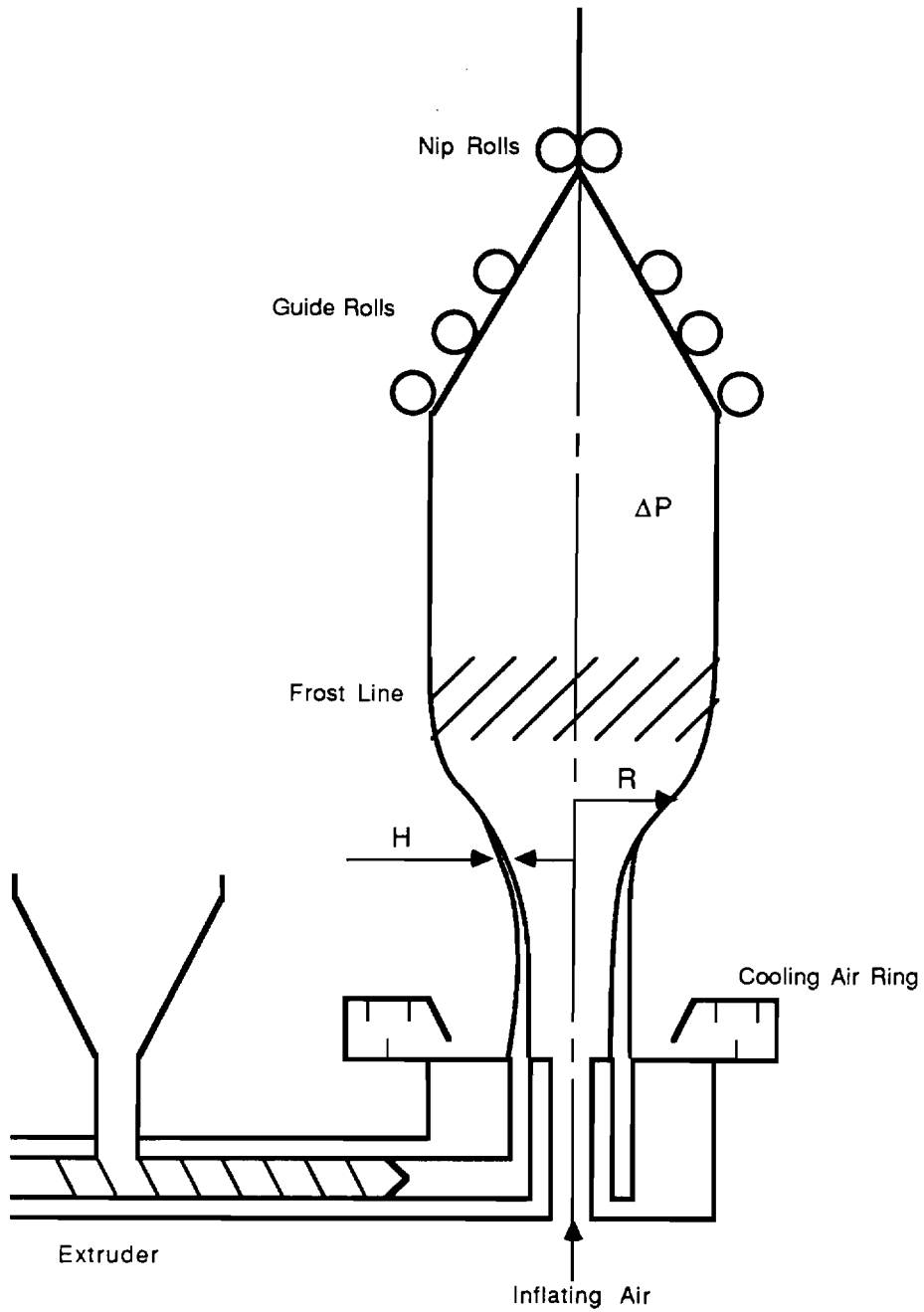


Figure 2-1 Blown film extrusion process.

direction. Another function of the cooling air ring is to help to stabilize the tubular film shape. The inflated tubular film is guided to pass through nip rolls by a series of guide rolls. The nip rolls are controlled by a motor which provides variable speeds to produce different draw-down ratios.

## 2.2 Kinematics

The kinematics of the tubular film blowing process were first analyzed by Pearson [22] and were detailed in a series of studies by Pearson and Petrie [3,4]. The following assumptions were made in their development:

- (1) The polymer melt behaves as a Newtonian fluid.
- (2) There is no occurrence of heat transfer between the film and the environment, i.e., the rheological properties of the melt are independent of variation of temperature.
- (3) Comparing with the other dimensions of the tubular film, the curved film is thin enough to be approximated by a plane film, i.e., thickness  $H \ll R_i$  where  $R_i$  is the radius of curvature of the bubble.
- (4) The tubular film is axisymmetric about the Z axis, which is along the machine direction.
- (5) There is no velocity gradient across the film.

(6) The coordinate system is shown as Figure 2-2, in which "1" is the machine direction (i.e., the direction of flow), "2" is the circumferential (transverse) direction, and "3" is the thickness direction (i.e., the direction normal to the film).

For a point P embedded in the inner surface of the bubble, its rectangular Cartesian coordinates  $(\xi_1, \xi_2, \xi_3)$  can be related to the cylindrical coordinate system  $(R, \theta, Z)$ , as shown in Figure 2-2, where  $\theta$  is the angle between the bubble profile and the Z-axis. The rate-of-strain tensor is written as

$$d = \begin{vmatrix} d_{11} & 0 & 0 \\ 0 & d_{22} & 0 \\ 0 & 0 & d_{33} \end{vmatrix} \quad (2-1)$$

Let  $(V_1, V_2, V_3)$  be the velocity components in the coordinates  $(\xi_1, \xi_2, \xi_3)$ , then from the definition

$$d_{ij} = \frac{\partial v_j}{\partial x_i} + \frac{\partial v_i}{\partial x_j} \quad (2-2)$$

we have

$$d_{11} = 2 \frac{\partial v_1}{\partial \xi_1} \quad (2-3a)$$

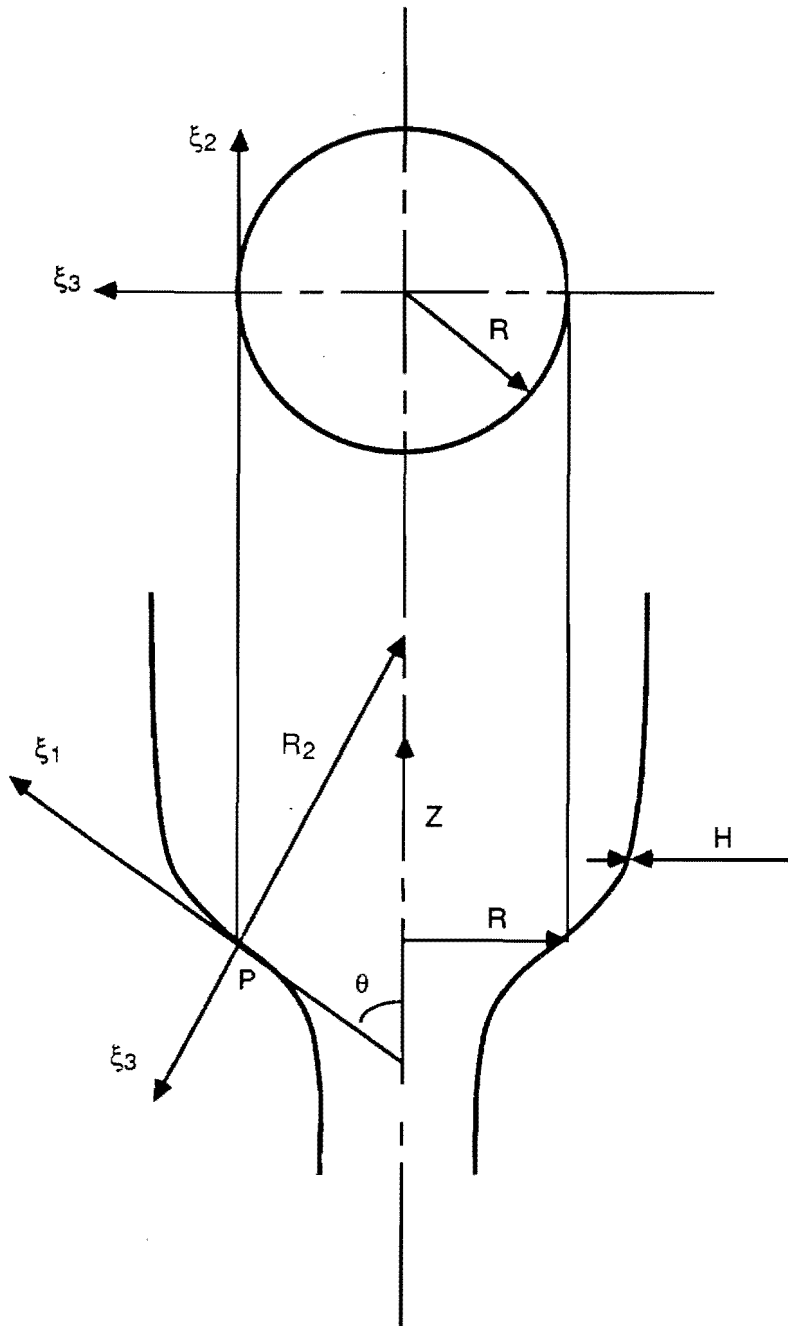


Figure 2-2 Coordinate systems of a tubular film.

$$d_{22} = 2 \frac{\partial v_2}{\partial \xi_2} \quad (2-3b)$$

$$d_{33} = 2 \frac{\partial v_3}{\partial \xi_3} \quad (2-3c)$$

Based on the above assumptions and through the following two relationships:

$$V_1 = \frac{d\xi_1}{dt} \quad (2-4a)$$

$$d\xi_1 = \frac{1}{\cos\theta} dz \quad (2-4b)$$

$d_{22}$  and  $d_{33}$  may be expressed as

$$d_{22} = \frac{2}{R} \frac{dR}{dt} = 2V_1 \cos\theta \frac{1}{R} \frac{dR}{dZ} \quad (2-5)$$

$$d_{33} = \frac{2}{H} \frac{dH}{dt} = 2V_1 \cos\theta \frac{1}{H} \frac{dH}{dZ} \quad (2-6)$$

where  $t$  is the time.

Under the assumption that the polymer is an incompressible fluid,  $d_{11}+d_{22}+d_{33}=0$ , we have

$$d_{11} = -2V_1 \cos\theta \left( \frac{1}{R} \frac{dR}{dZ} + \frac{1}{H} \frac{dH}{dZ} \right) \quad (2-7)$$

Furthermore, the velocity component  $V_1$  can be easily expressed in terms of  $R$ ,  $H$ , and  $Q$

$$V_1 = \frac{Q}{2\pi RH} \quad (2-8)$$

where  $Q$  is the volumetric flow rate. Finally, Equations (2-5), (2-6) and (2-7) are rewritten as:

$$d_{11} = \frac{-Q \cos \theta}{\pi RH} \left( \frac{1}{R} \frac{dR}{dZ} + \frac{1}{H} \frac{dH}{dZ} \right) \quad (2-9)$$

$$d_{22} = \frac{Q \cos \theta}{\pi RH} \frac{1}{R} \frac{dR}{dZ} \quad (2-10)$$

$$d_{33} = \frac{Q \cos \theta}{\pi RH} \frac{1}{H} \frac{dH}{dZ} \quad (2-11)$$

From the above kinematic analysis, Han and Park [11] developed two special cases: (1) uniaxial stretching,  $2d_{22}=2d_{33}=-d_{11}$ , and (2) uniform biaxial stretching,  $2d_{11}=2d_{22}=-d_{33}$ . Furthermore, Choi, White and Spruiell [23] correlated the processing variables, drawdown ratio  $V_L/V_0$  and blow-up ratio  $BUR=R_L/R_0$ , with several special cases of kinematics:

(1) Uniaxial extension

$$d_{22} = d_{33} \quad (2-12a)$$

$$\frac{1}{R} \frac{dR}{dZ} = \frac{1}{H} \frac{dH}{dZ} \quad (2-12b)$$



Integrating Equation(2-12b) from die exit to the take-up position, we have

$$\frac{V_L}{V_o} = \frac{1}{BUR^2} \quad (2-13)$$

where the subscript "L" and "o" represent the positions of take-up device and die exit, respectively.

(2) Planar extension

$$d_{22} = 0 \quad ; \quad \frac{1}{R} \frac{dR}{dZ} = 0 \quad (2-14)$$

Then the following can be obtained

$$BUR = \frac{R_L}{R_o} = 1 \quad (2-15a)$$

$$\frac{V_L}{V_o} = \frac{H_o}{H_L} \quad (2-15b)$$

(3) Equal biaxial extension

$$d_{11} = d_{22} \quad (2-16a)$$

$$\frac{-1}{H} \frac{dH}{dZ} - \frac{1}{R} \frac{dR}{dZ} = \frac{1}{R} \frac{dR}{dZ} \quad (2-16b)$$

Integration of Equation(2-16b) leads to

$$\frac{V_L}{V_0} = \text{BUR} \quad (2-17)$$

That is, under the processing condition of the drawdown ratio being equal to the blow-up ratio, an uniform biaxially stretched film can be obtained.

### 2.3 Dynamics

A precise dynamic analysis for the tubular film blowing process would be very complicated because of the bubble being stretched in two directions. Alfrey [24] may be the earliest one to develop the force balance equations from membrane theory. Nevertheless, a more detailed and deeper discussion was in a series of studies by Pearson and Petrie [3,4,20]. By neglecting inertial, gravitational force and surface tension, they made a mechanical analysis for an isothermal Newtonian flow of a thin tubular film. Then, Petrie [25] reconsidered this tubular film as an Oldroyd type of viscoelastic fluid under an isothermal condition. In a later paper, Petrie [21] carried out the calculation of his model for a non-isothermal Newtonian and an isothermal elastic flow, and he made a comparison with the published experimental results [26-28]. Han and Park [5] argued the importance of the effect of

gravity during processing, and added a term for gravitational force into the force balance equations.

The force balances for blown film extrusion can be split into two directional considerations.

(1) In the machine direction

An overall force balance in longitudinal direction is given by

$$F_{\text{rheo}} = F_L - F_{\text{grav}} - F_{\text{drag}} - F_{\text{surf}} - F_{\text{inert}} - \pi(R_L^2 - R^2)\Delta P \quad (2-18)$$

where

$F_{\text{rheo}}$  = the rheological force in the film,

$F_L$  = the take-up force being applied on the film,

$F_{\text{grav}}$  = the gravitational force due to the film's weight,

$F_{\text{drag}}$  = the drag force between the air and the film  
surface,

$F_{\text{surf}}$  = the surface tension of the bubble,

$F_{\text{inert}}$  = the inertial force required to accelerate the  
fluid,

$\Delta P$  = the pressure difference across the film, i.e.,  $\Delta P =$   
( $P_{\text{inside}} - P_{\text{outside}}$ ).

Comparing with the magnitude of the total force acting in the machine direction, the contributions of surface tension are insignificant, and the inertial and drag force become

unimportant for the reason of low take-up speed. Thus, neglect of the  $F_{drag}$ ,  $F_{surf}$  and  $F_{inert}$  terms is very reasonable, and the rest of the terms in Equation(2-18) are expressed as

$$F_{rheo} = 2\pi RH\sigma_{11}\cos\theta \quad (2-19)$$

$$F_{grav} = 2\pi\rho_m g \int_z^{z_F} RH\sec\theta \, dz + 2\pi\rho_s g RH(z_L - z_F) \quad (2-20)$$

where

$\sigma_{11}$  = the normal stress in the machine direction,

$\rho_m$  = the density of polymer in the molten state,

$\rho_s$  = the density of polymer in the solid state,

$z_L$  = the height of the take-up position,

$z_F$  = the height of the frost line,

$g$  = the standard acceleration of gravity.

(2) In the circumferential direction

Based on the considerations in the above statements and the membrane theory [29], the force balance equation in the transverse direction is given by

$$\Delta P = \frac{\sigma_{11}}{R_1} + \frac{\sigma_{22}}{R_2} - \rho g H \sin\theta \quad (2-21)$$

where  $\sigma_{22}$  is the normal stress in the hoop direction, and  $R_1$  and  $R_2$  are the principal radii of curvature of the film in the direction "1" and "2", respectively. From the geometrical relationships the two principal radii can be expressed as

$$R_1 = \frac{-\sec^3\theta}{\frac{d^2R}{dZ^2}} \quad (2-22a)$$

$$R_2 = \frac{R}{\cos\theta} \quad (2-22b)$$

For an incompressible fluid, the total stress  $\sigma$  can be expressed by two separate terms, the isotropic pressure  $p$  and the deviatoric stress  $\tau$ . Hence the component of total stress is given by

$$\sigma_{ij} = -p\delta_{ij} + \tau_{ij} \quad (2-23)$$

where  $\delta_{ij}$  is the component of the Kronecker delta and  $i$  is 1, 2, or 3. In the tubular film blowing process, the stress at the free surface is equal to atmospheric pressure, and we have

$$\sigma_{33} = -p + \tau_{33} = 0 \quad (2-24)$$

That is, being relative to atmospheric pressure  $\sigma_{33}$  is zero.

Finally, the expression for both of the total stresses acting in the machine and hoop direction are obtained

$$\sigma_{11} = \tau_{11} - \tau_{33} \quad (2-25)$$

$$\sigma_{22} = \tau_{22} - \tau_{33} \quad (2-26)$$

## 2.4 Rheology

Shear viscosity and elongational viscosity are two important measures of performance of polymer melt in processing. The main factors that affect the viscosity of melt are molecular structures (e.g. molecular weight, degree and type of molecular chain branching, molecular weight distribution, and as crystallization progresses in the film blowing process, the degree of crystallinity) and the processing conditions (e.g. processing temperature and deformation rate).

### Influence of Molecular Structure on Rheological Performance

Small [30] argued the effects of long chain branching on the viscosity of polyethylene. Bueche [31] established a quantitative relationship between the viscosity of linear polymer and branched polymer

$$\frac{(\mu_0)_{br}}{(\mu_0)_{lin}} = g_r^{3.5} \quad (2-27)$$

where  $(\mu_0)_{br}$  and  $(\mu_0)_{lin}$  are the zero-shear viscosity of a long chain branched polymer and a linear polymer, respectively. The  $g_r$  in the above equation is the ratio of the mean-square radius of gyration of these two types of polymers, and is written as

$$g_r = \frac{\langle s^2 \rangle_{br}}{\langle s^2 \rangle_{lin}} \quad (2-28)$$

With regard to the influence of molecular weight on viscosity, Fox and Flory [32,33] found that the zero-shear viscosity  $\mu_0$  is proportional to  $\bar{M}_w^{3.4}$  under the condition of  $\bar{M}_w > M_c$  (the critical molecular weight for entanglements of chains). Nevertheless, for the sake of practical reason, the effects of molecular weight and long chain branching have to be considered for a typical polydisperse polymer. Atalla and Romanini [34] proposed an empirical equation describing the isothermal behavior of elongational viscosity under the influences of molecular weight and long chain branching

$$\log \eta_E = 2.18 \log \left\{ \left[ \frac{(\eta_0)_{br}}{(\eta_0)_{lin}} \right]^{2.84} \frac{1}{\beta \bar{M}_w} \right\} - 7.87 \quad (2-29)$$

where  $\beta$  is the dimensional polydispersity and  $\eta_0$  is the measured zero-shear-rate viscosity from the molten sample. From this equation, it is found that the effect of long chain branching is to lower the elongational viscosity for the same values of  $\beta\bar{M}_w$ , "molecular weight times polydispersity".

Furthermore the influence of the molecular structure on the melt extensibility and extrusion defects for polyethylene resins were studied by Constantin [35], Acierno et al. [36], and Mantia et al. [37]. Constantin found that the lack of long chain branching leads to a good extensibility, and the phenomenon of melt fracture would cause surface defects on the bubble of the blown film extrusion. Acierno et al. discovered that for different samples, HDPE, LDPE, and LLDPE (i.e., high density, low density, and linear low density polyethylene), the breaking stretch ratio increases with melt index while the melt strength decreases with the increase of melt index. Moreover, Mantia et al. concluded that the substitution of LDPE by the blend of 25% LLDPE with LDPE shows a good performance during processing of the blown film extrusion.

In a series of studies Han et al. [38], Han and Kwack [39], and Kwack and Han [40] established a good understanding of the relationship between rheological properties and processing conditions for polyethylene resins with different molecular structures. They found that the resin with a



narrower molecular weight distribution and less degrees of long chain branching increases the blowability of tubular film, and the lower elongational viscosity leads a larger draw-down ratios.

### Rheological Modelling

In the earliest mathematical analysis for the blown film extrusion, an isothermal Newtonian fluid was assumed [3,22]. Thus, under this assumption, the viscosity value of the polymeric material should keep constant through the whole processing. However, for non-Newtonian fluid, the main factors affecting its viscosity are temperature, deformation rate and the previous kinematic history [41].

In the tubular film blowing process, the kinematics are basically the elongational type rather than the shear one [42]. Hence, Han and Park [11] determined the elongational viscosity by force balance equations. They carried out the experiments under an isothermal condition to eliminate the influence of temperature. By controlling the inside pressure of the bubble, the uniaxial and biaxial elongational flow were investigated. Their experimental results showed that the elongational viscosity may decrease or increase with the elongation rate, and even may be independent of elongational rate. Moreover, they concluded that the data of elongational viscosity obtained from the blown film under the condition of

uniaxial stretching (i.e.,  $\Delta P=0$ ) is consistent with the data of elongational viscosity obtained from the melt spinning process [43-47].

Beside the elongational rate, the variation of temperature may be the dominating factor to effect the value of viscosity in processing. Hence an Arrhenius type equation which describes the temperature dependence of melt viscosity was given as [48]

$$\eta = \eta_0 \exp\left[\frac{E_a}{R_g T}\right] \quad (2-30)$$

where  $R_g$  is the gas constant,  $E_a$  is the viscosity activation energy and  $\eta_0$  is a constant, the reference viscosity, which depends on an arbitrary reference temperature selected. Therefore, in the second part of a series of papers by Han and Park [5], they expressed the elongational viscosity by the Arrhenius-type function of temperature and the second invariant of deformation rate tensor for the non-isothermal blown film extrusion

$$\eta(T, II) = \eta_0 \exp\left[\frac{E_a}{R_g} \left(\frac{1}{T} - \frac{1}{T_0}\right)\right] \left[\frac{II}{2}\right]^{\frac{n-1}{2}} \quad (2-31)$$

where  $\eta_0$  is the elongational viscosity at the reference temperature  $T_0$ ,  $T$  is the temperature of the film,  $II$  is the

second invariant of the rate-of-strain tensor, and  $n$  is the power law index. Equation(2-31) was used in the computer simulation for tubular film blowing process by Han et al. [5] and Yamane [49].

Generally speaking, the materials the most frequently used to produce tubular films are semi-crystalline, e.g. polyethylene and polypropylene [1]. Thus, Kanai and White [6] included a term of crystallinity in the viscosity equation. Considering that the occurrence of crystallization causes a resistance to deformation, the viscosity equation was given by

$$\eta = \eta_0 \exp\left[\frac{E_a}{R_g}\left(\frac{1}{T} - \frac{1}{T_0}\right)\right] \exp(GX) \quad (2-32)$$

in which  $X$  is the fraction of crystallinity and  $G$  is a material constant obtained from experimental results [14]. In a later paper, Kanai [50] used a more complete rheological model to analyze the high molecular weight HDPE tubular film process. The viscosity equation included the factor of temperature, the second invariant of deformation rate tensor, the power law index and the fraction of crystallinity

$$\eta(T, II, X) = \eta_0 \exp\left[\frac{E_a}{R_g}\left(\frac{1}{T} - \frac{1}{T_0}\right) + GX\right] [II]^{\frac{n-1}{2}} \quad (2-33)$$

## 2.5 Energy Balance

The earlier theoretical analysis [3,4,20,22,25] of blown film extrusion lacked any consideration of the influence of temperature, that is, an isothermal condition was assumed. In a later study by Petrie [51], the mathematical modelling of heat transfer in film blowing was qualitatively discussed, and he [21] developed a mathematical model to simulate the flowing behavior of non-isothermal Newtonian fluid merely by adding a temperature term [26-28] into the viscosity and density equation.

Han and Park [5] established a quantitative description of the occurrence of heat transfer in the film blowing process. The following assumptions were made in their theoretical analysis:

(1) The heat transfer between the inner surface of film and the inflating air inside the bubble is negligible.

(2) The heat transfer between the tubular film and the environment is primarily controlled by convection and radiation, and the heat conduction of the film may be neglected.

(3) The heat generation due to the frictional force is small enough to be neglected.

(4) The heat of crystallization is negligible even if the material is semi-crystalline.

Thus, the energy balance equation was given as

$$\rho C_p \left( \frac{Q \cos \theta}{2\pi R} \right) \frac{dT}{dZ} = -U(T-T_{air}) - \epsilon \sigma (T^4 - T_r^4) \quad (2-34)$$

in which

- $\rho$  = the density of material,
- $C_p$  = the specific heat capacity,
- $T$  = the temperature of the film,
- $T_{air}$  = the temperature of cooling air,
- $T_r$  = the room temperature,
- $\epsilon$  = the emissivity of the film,
- $\sigma$  = the Stefan-Boltzmann constant.

As mentioned in the previous section, the semi-crystalline polymers are the most frequently used to produce tubular film. Moreover, some of these semi-crystalline polymers have high values of final crystallinity. Thus, the amount of the crystallization energy, which is released while the crystalline phase appears, would be so large that its influence on the film's temperature is very significant [14]. Hence, Kanai and White [6,14] established the energy balance equation more completely by adding a term of crystallization into Equation(2-34), and it becomes

$$\rho C_p \left( \frac{Q \cos \theta}{2\pi R} \right) \frac{dT}{dZ} = -U(T - T_{\text{air}}) - \epsilon \sigma (T^4 - T_r^4) + \rho \Delta H_f \left( \frac{Q \cos \theta}{2\pi R} \right) \frac{dX}{dZ} \quad (2-35)$$

in which  $\Delta H_f$  is the heat of fusion, and  $X$  is the fraction of crystallinity.

### Heat Transfer Coefficient

In the practical processing condition, the tubular film is cooled by forced convection by the ambient cooling air. Moreover, according to the experimental analysis of Menges and Predohl [15], the amount of heat transfer by radiation is about 15 percent of the total amount of overall heat transfer. Thus, the cooling rate of the film is dominated by the heat convection term in Equation(2-35), and the determination of the overall heat transfer coefficient  $U$  is certainly important.

Menges and Predohl [15,52] proposed an empirical equation to correlate the velocity of cooling air to the heat transfer coefficient

$$U = 3.3 ( V_{\text{max}} )^{1.5} \quad (2-36a)$$

and for heavy sacks

$$U = 3.04 ( V_{\text{max}} )^{1.3} \quad (2-36b)$$

in which  $V_{\max}$  is the characteristic (maximum) air velocity along the machine direction.  $V_{\max}$  is a function of position and can be estimated by

$$V_{\max} = V_{\max, F} \left( \frac{Z_F}{Z} \right)^{0.74} \quad (2-37)$$

where  $V_{\max, F}$  is the maximum air velocity at the position of frost line,  $Z_F$ .

Afterwards, Kanai and White [14] carried out an on-line measurement for temperature, and from the temperature profiles they concluded that

$$Z < Z_c \quad U = k_1 \quad (2-38a)$$

$$Z > Z_c \quad U = \frac{k_2}{Z^\gamma} \quad (2-38b)$$

where  $Z_c$  is a critical position and equal to 8 cm in their study, and  $k_1$ ,  $k_2$  and  $\gamma$  are constants. In other words, the value of heat transfer coefficient remains constant from the die exit to a critical position  $Z_c$ , then starts to decrease along the machine direction. The values of  $k_1$ ,  $k_2$  and  $\gamma$  would vary with cooling air velocity.

Kanai et al. [14] also carried out a dimensionless analysis for the apparent heat transfer coefficient. The correlation between Reynolds number, Nusselt number and Prandtl number was given by [53,54]

$$\frac{UL}{k_{air}} = m_i \left[ \frac{LV_{air}\rho_{air}}{\eta_{air}} \right]^{m_j} \left[ \frac{C_{p,air}\eta_{air}}{k_{air}} \right]^{m_k} \quad (2-39)$$

where  $k$  is the thermal conductivity,  $m_i$ ,  $m_j$  and  $m_k$  are constants, and the subscript "air" refers to the values for air. They found the above equation is more suitable for the case of the lower frost line height, and obtained the following empirical relationship

$$\frac{UL}{k_{air}} = 0.043 \left[ \frac{LV_{air}\rho_{air}}{\eta_{air}} \right]^{0.76} \quad (2-40)$$

Also, Kanai et al. successfully correlated the  $V_{max}$  and  $U$  by the form proposed by Menges et al.

$$U = 2.5 V_{max}^{1.6} \quad (2-41)$$

from the experimental data above the frost line.



## 2.6 Crystallization Kinetics

The mechanism of crystallization and the processing conditions can interact with each other. The appearance of crystalline phase during processing will affect the rheological performance and the actual temperature of the material. On the other hand, the processing conditions, such as, cooling rate and the external forces, will also cause the crystallization behavior to change.

### Nucleation and Growth Under Isothermal Condition

For the case of homogeneous nucleation, Frenkel [55] presented a theory of isothermal heterophase fluctuations. Then, Turnbull and Fisher [56] obtained an equation to describe the nucleation rate from a condensed liquid system

$$N = N_0 \exp\left[\frac{-E_D}{kT} - \frac{\Delta G^*}{kT}\right] \quad (2-42)$$

where  $N_0$  is a constant dependent on the geometry and interface energy of nucleus,  $E_D$  is the activation energy for transport across the phase boundary, and  $\Delta G^*$  is the free-energy to form a nucleus with critical size. The two exponential terms in Equation(2-42) have opposite temperature dependence. Thus, the overall nucleation rate is the result of the competition between the rate of formation of nuclei

and the rate of transport of molecules, and a maximum nucleation rate occurs between  $T_m$  and  $T_g$ .

Generally  $\Delta G^*$  was expressed as [56-59]:

$$\Delta G^* = \frac{q\gamma_s^2\gamma_e}{\Delta G_f^2} \quad (2-43a)$$

and  $\Delta G_f = \frac{\Delta H_f \Delta T}{T_m}$  (2-43b)

where  $q$  is a constant which is related to the geometry of the critical nucleus,  $\Delta T = T_m - T$  is the supercooling,  $\gamma_s$  is the interfacial free energy of the side surface,  $\gamma_e$  is the surface free energy of the end surface, and  $\Delta G_f$  is the free energy between two phases.

With regard to the heterogeneous nucleation, Price [59] and Turnbull [60] introduced a term of interfacial free energy between the impurities (or nucleation agents) and polymer molecules

$$N = C \exp\left[\frac{-E_p}{kT}\right] \exp\left[\frac{-16\gamma_s\gamma_e\Delta\gamma T_m^2}{kT\Delta H_f\Delta T^2}\right] \quad (2-44)$$

where  $C$  is a constant and  $\Delta\gamma = \gamma_{s1} - \gamma_{s2}$ , in which  $\gamma_{s1}$  and  $\gamma_{s2}$  are the interfacial energy between the heterogeneity and the polymer crystal and polymer melt, respectively.

Using a model involving secondary nucleation of chains on a pre-existing crystal, Hoffman and Lauritzen [57] proposed an equation for growth rate

$$G = G_0 \exp\left[\frac{-E_D}{kT}\right] \exp\left[\frac{-4b_0\gamma_s^2\gamma_e\Delta\gamma T_m^0}{kT\Delta H_f\Delta T}\right] \quad (2-45)$$

where  $b_0$  is the thickness of the chain molecules. Since  $E_D$  was considered as being related to segmental mobility of polymer chains [61], its temperature dependence may be described by the Williams-Landel-Ferry equation [62]

$$E_D = \frac{C_1}{C_2 + T - T_g} \quad (2-46)$$

where  $C_1$  and  $C_2$  are constants and equal to 17.4 KJ/mol and 51.6 K respectively.  $E_D$  may be written as [63]

$$E_D = \frac{U^*}{T - T_\infty} \quad (2-47)$$

where  $U^* \approx 1500$  cal/mol and  $T_\infty = T_g - 30$  K.

#### Overall Transformation Analysis Under Isothermal Condition

The original transformation equation was proposed for inorganic material by Avrami [64-66]. Mandelkern [67]

modified the Avrami equation to make it suitable for polymeric material

$$\frac{X(t)}{X_f} = 1 - \exp[-kt^n] \quad (2-48)$$

where  $X(t)$  is the crystallinity at time  $t$ ,  $X_f$  is the ultimate crystallinity,  $k$  is the crystallization rate constant and  $n$  is the Avrami index. However Equation(2-48) seems too simplified. Kawai, Iguchi and Tonami [68] and Wilhelm [69] found that the above equation is unable to describe the phenomenon of secondary crystallization, which occurs in the latter stages of crystallization.

#### Non-Isothermal Crystallization

The theories in the above two sections are only suitable for an isothermal condition, which is too ideal to describe the crystallization behavior under a practical processing condition.

Thus, a lot of studies [70-77] for non-isothermal crystallization have been done. Nakamura [70,71] developed an analysis based on the analysis for isothermal crystallization to analyze the behavior of non-isothermal crystallization. Assuming an "isokinetic" condition, Nakamura presented the following equation

$$X(t) = 1 - \exp\left[-\left(\int_0^t K(T) dt\right)^n\right] \quad (2-49)$$

where  $X(t)$  is the degree of crystallinity at time  $t$ ,  $n$  is the Avrami index based on the isothermal experiments and  $K(T)$  is determined from isothermal crystallization rate  $k(T)$  through the relation  $K(T)=k(T)^{1/n}$ .

Ziabicki [77] proposed an empirical Gaussian relation to describe the temperature dependence of the rate of crystallization

$$K(T) = K_{\max} \exp\left[-4\ln(2)\frac{(T-T_{\max})^2}{D^2}\right] \quad (2-50)$$

where  $K$  is equal to the reciprocal of crystallization half time,  $T_{\max}$  is the temperature at the occurrence of  $K_{\max}$ , and  $D$  is the width at half height of the  $K(T)$  curve. All parameters,  $K_{\max}$ ,  $T_{\max}$  and  $D$ , in Equation(2-50) are obtained from the experiment of isothermal crystallization.

### Stress-Induced Crystallization

For most of the practical processing, the polymer melt is subjected to external forces (or stresses). Hence the appearance of molecular orientation, which is caused by the stresses [78], in the amorphous phase will affect the crystallization behavior.

Ziabicki [77] proposed a rate equation of crystallization in an oriented system by adding a term of orientation into Equation(2-50)

$$K(T, f) = K(T) \exp [ Af^2 ] \quad (2-51)$$

where A is a temperature dependent empirical parameter, and f is a parameter for orientation. In Equation(2-51), the parameter A can be expressed as

$$A(T) = \frac{c_1 + c_2 \Delta T}{\Delta T^3} \quad (2-52)$$

where  $c_1$  and  $c_2$  are constants.

Kobayashi and Nagasawa [79] considered that the stresses would affect the free energy between crystal and melt phase, and they introduced a free-energy term,  $\Delta G_{def}$ , which is caused by deformation of the polymer chains, into the nucleation rate equation

$$\frac{N(\text{stressed})}{N(\text{quiescent})} = \exp \left[ \frac{q\gamma_s^2 \gamma_e}{kT} \left( \frac{1}{\Delta G_{def}^2} - \frac{1}{\Delta G_f^2} \right) \right] \quad (2-53)$$

Afterwards, according to Hoffman-Lauritzen theory [80] and Kobayashi and Nagasawa's study [79], Katayama et al. [81]

and later Zhou [82] incorporate the effect of stress into the crystallization kinetic equation

$$K(T, f_a) = K_0 \exp\left[\frac{-U^*}{R(T-T_\infty)}\right] \exp\left[\frac{-C_3}{T\Delta T + C_0 T^2 f_a^2}\right] \quad (2-54)$$

where  $f_a$  is the amorphous orientation function, and  $C_0$  and  $C_3$  are constants. Zhou also successfully applied the above equation to simulate the melt spinning process for polypropylene.

## 2.7 Orientation and Structure Development in Film Blowing Process

The relationship between the fabrication conditions and the supermolecular structure of polymer is very important. The performance of the blown film product is basically determined by the character of the supermolecular structure, such as, orientation of polymer chains, degree of crystallinity and crystal morphology.

There were several investigators who explored the morphology and orientation in polyethylene films. Holmes and Palmer [83] used flat-plate x-ray diffraction and birefringence to study the blown polyethylene film under various blow-up ratios, and they found that the b-axis is

oriented in the plane perpendicular to the machine direction. Using the analysis of WAXS (wide-angle x-ray scattering) and pole figures, Lindenmayer and Lustig [84] concluded that for tubular LDPE film, the b-axis is perpendicular to the film and a- and c-axis uniformly distribute in the plane of the film. Nagasawa et al. [16] reported the development of birefringence along the machine direction under the processing condition of unit blow-up ratio. Maddams and Preedy [85-87] published a series of papers to discuss the orientation of HDPE blown film. They characterized the orientation by pole figures and presented two types of orientational behavior, which depends on the kinds of samples and the processing variables, such as, blow-up ratio, draw-down ratio and cooling conditions. They also found that the processing conditions of high draw-down ratio and low extrusion temperature would cause the occurrence stress-induced crystallization.

All of the above investigations were qualitative and did not give much consideration to the kinematics and stress fields of the film blowing process. Choi, White and Spruiell [23] presented a quantitative study about the orientational development of tubular film extrusion for atactic polystyrene. The in-plane and out-plane birefringence data were compared and correlated with the kinematics and the applied tensions. Later, Choi, Spruiell and White [88] made



much deeper development to investigate the orientation and morphology of semi-crystalline polymer. They used the wide-angle x-ray scattering pole-figure analysis and birefringence to characterize the orientation and crystallinity of high density polyethylene (HDPE). They found that the crystalline biaxial orientation factors were unique functions of the stresses exerted on the bubble at the position of frost line; moreover, these correlations were the same as those developed by Dees and Spruiell [89] for melt-spun HDPE fibers. Furthermore, a possible morphological model was proposed to interpret the experimental results and the influence of biaxial stresses.

## 2.8 Instabilities in Tubular Film Blowing

Only a few studies investigated the instability of the bubble and the reasons for this phenomenon are still unclear. Most of the investigations focused their attention on the qualitative description. Han and Park [90] experimentally observed that a type of instability similar to draw resonance occurred under uniaxial stretching, and a surface wave-type instability was found in biaxial stretching. Later, Han and Shetty [12] had a further observation that a disturbance from the take-up speed would cause a much more severe instability

than that of inflating air pressure did. Moreover, they also found that the decrease of melt temperature might help the bubble to stabilize itself.

Kanai and White [14] and Minoshima and White [91] studied the relationship between the processing variables, such as, draw-down ratio, blow-up ratio and frost line height, and the materials, such as, different kind of resin, rheological properties and molecular structures. Minoshima et al. proposed a more detailed qualitative description of instabilities by four types of unsteady state behavior.

Apparently only two reports [92,93] deal with the instable phenomena in a quantitative manner. Yeow [93] analyzed the stability of an isothermal Newtonian model by the methods of linear hydrodynamic stability. Cain and Denn [92] made an extensive quantitative analysis to correlate the operation variables with the process stability by two different rheological models, the Newtonian and Maxwell model. They concluded that the increase of melt viscosity by cooling is a significant stabilizing factor, and the process stability depends on the selection of control variables.

## 2.9 Mathematical Modelling of Tubular Blown Film Extrusion

### System Equations of Mathematical Model

Although various considerations and material equations were used in the theoretical simulation for film blowing process, the primary system equations were generally similar in principle. Generally speaking, the governing system equations of non-isothermal tubular film blowing for semi-crystalline material can be derived and shown as follows.

With the assumptions of neglecting the inertial force, surface tension, and drag force, the following two dimensionless differential equations for an Arrhenius-type viscosity equation are obtained from Equations (2-18) - (2-22), (2-25), (2-26) and (2-33):

$$\frac{H^{*'}}{H^*} = \frac{-R^{*'}}{2R^*} - \frac{\eta_0 (F_M + R^{*2} B^*) \sec^2 \theta}{4\eta} \quad (2-55)$$

$$2R^{*2} (F_M + B^* R^{*2}) R^{*''} = \frac{6\eta R^{*'}}{\eta_0} + R^* \sec^2 \theta (F_M - 3B^* R^{*2}) \quad (2-56)$$

where

$$F_M = \frac{R_0}{Q\eta_0} \left[ F_Z - 2\pi\rho_m g R_0^3 \int_{z^*}^{z_F^*} R^* H^* \sec \theta dz^* \right] - B^* \left[ \frac{R_L}{R_0} \right]^2 \quad (2-57)$$

$$F_z = F_L - 2\pi\rho_s g R_L H_L (Z_L - Z_F) \quad (2-58)$$

$$B = \frac{\pi R_o^3 \Delta P}{Q \eta_o} \quad (2-59)$$

and the above dimensionless variables are defined as

$$R^* = \frac{R}{R_o} \quad ; \quad H^* = \frac{H}{R_o} \quad ; \quad Z^* = \frac{Z}{R_o} \quad (2-60)$$

From Equation(2-35) the dimensionless heat transfer equations with the consideration of crystallization is given by

$$T^{*'} = -R^* C^* \sec\theta (T^* - T_{air}^*) - R^* D^* \sec\theta (T^{*4} - T_r^{*4}) + F X^{*'} \quad (2-61)$$

where

$$C = \frac{U T_o}{\frac{\rho C_p Q T_o}{2\pi R_o^2}} \quad (2-62)$$

$$D = \frac{\sigma \epsilon T_o^4}{\frac{\rho C_p Q T_o}{2\pi R_o^2}} \quad (2-63)$$

$$F = \frac{\Delta H_f}{C_p T_o} \quad (2-64)$$

$$T^* = \frac{T}{T_0} \quad ; \quad X^{*'} = \frac{dX}{dZ^*} \quad (2-65)$$

In addition to the above equations, the following equation is obtained from the geometrical relationship:

$$R^{*'} = \frac{dR^*}{dZ^*} = \tan\theta \quad (2-66)$$

Hence, according to the suggestions of Han and Park [5], the four differential equations could be simultaneously solved by the fourth-order Runge-Kutta method incorporating a procedure of trial-and-error (assuming a value for  $F_M$ ) in order to meet the following initial and boundary conditions

(i) at  $Z^*=0$

$$R^*=1.0 \quad ; \quad H^* = \frac{H_0}{R_0} \quad ; \quad T^*=1.0 \quad ; \quad \theta = \theta_0 \quad (2-67)$$

(ii) at  $Z^*=Z_F^* = \frac{Z_F}{R_0}$

$$R^* = \frac{R_L}{R_0} \quad ; \quad H^* = \frac{H_L}{R_0} \quad ; \quad T^* = \frac{T_s}{T_0} \quad ; \quad \theta = 0 \quad (2-68)$$

where  $T_s$  is the temperature at which the polymeric melt is solidified.

### Computer Simulation Based on Various Rheological Models

Some investigators [19,94,95] carried out computer simulation of film blowing based on the fundamental equations described above and various rheological models, such as, the Maxwell model by Wagner [95], the Maxwell and Leonov models by Luo and Tanner [94], and the viscoplastic-elastic model by Cao and Campbell [19]. Luo and Tanner found that the effects of viscoelasticity would stiffen the film, and the convected Maxwell model showed a better performance. They also showed that a numerical instability caused difficulty in predicting the case of BUR (blow-up ratio)  $< 1$ . Cao and Campbell [19] proposed a viscoplastic-elastic model to alter one of the conventional, kinematically based boundary conditions for freeze line,  $dR/dZ=0$ , to a rheologically based constraint. They thought that by defining a plastic-elastic transition zone, the total deformation history through the processing line could be decomposed into an unrecoverable part in which plastic deformation dominated, and a recoverable part in which elastic deformation dominated. Cao et al. concluded that the predicted results were in reasonable quantitative agreement with the literature data [96] below the plastic transition, i.e., below the region of frost line, and qualitatively agreed with data above the plastic transition.

## CHAPTER 3

### EXPERIMENTAL MATERIALS, EQUIPMENT, PROCEDURES AND DATA ANALYSIS

#### 3.1 Resin Identification

The material used in this study was a linear low density polyethylene (LLDPE) resin, which was supplied by Dow Chemical Company. Several properties of this resin, including melt flow index, density, weight-average molecular weight  $\bar{M}_w$ , and number-average molecular weight  $\bar{M}_n$ , are listed in Table 3-1. Because of its low melt flow index (MI=1.0), this resin is specially suitable for use in the tubular film blowing process. Hereafter, this resin will be referred to by its code name, LL1.

#### 3.2 Resin Processing

##### Equipment of Tubular Blown Film Extrusion

A Kissam single screw extruder (manufactured by Kissam Manufacturing, Inc., Mountainside, NJ), shown schematically in Figure 2-1, was used in the film blowing experiments. The

Table 3-1 Identification and properties of linear low density polyethylene\*.

Resin Type	Code Name	Density (g/cm <sup>3</sup> )	Melt Index	$\bar{M}_w$	$\bar{M}_n$	$\bar{M}_w/\bar{M}_n$
LLDPE	LL1	0.935	1.0	113,800	34,500	3.294

\*All the results of resin characterizations reported in this table were performed by Dow Chemical Company and released to the Department of Material Science and Engineering.



diameter of the screw is 3/4 inch ( $L/D=20$ ). Underneath the nitrogen purged hopper, the barrel was fitted with a cooling water sleeve to prevent the resin from melting too quickly and possibly clogging the feed area. An annular blown film die (inside diameter = 1.3970 cm, outside diameter = 1.5875 cm) mounted on the end of the barrel, was designed by Minoshima and Shimomura [97], and a sketch of this die is given in Figure 3-1.

The temperature inside the barrel is maintained by two separately controlled band-type heaters. For the annular die, two band-type heaters and one heating tape are used to keep this die at homogeneous temperature. Also, these heaters are separately controlled by three thermocouples to ensure that the temperature at every position is the same.

An air cooling ring with 5-cm diameter is installed just on the top of the die in order to cool and stabilize the extruded bubble. At the position of 82 cm above the die, a set of nip rolls is used to flatten and seal the bubble to keep the inside pressure constant. In the region between the annular die and nip rolls, there are several guide rolls to make the tubular film pass through the nip rolls smoothly and minimize the sliding motion of the bubble. After the film passes through the nip rolls, two sets of take-up rolls controlled by a motor provide variable speeds to produce

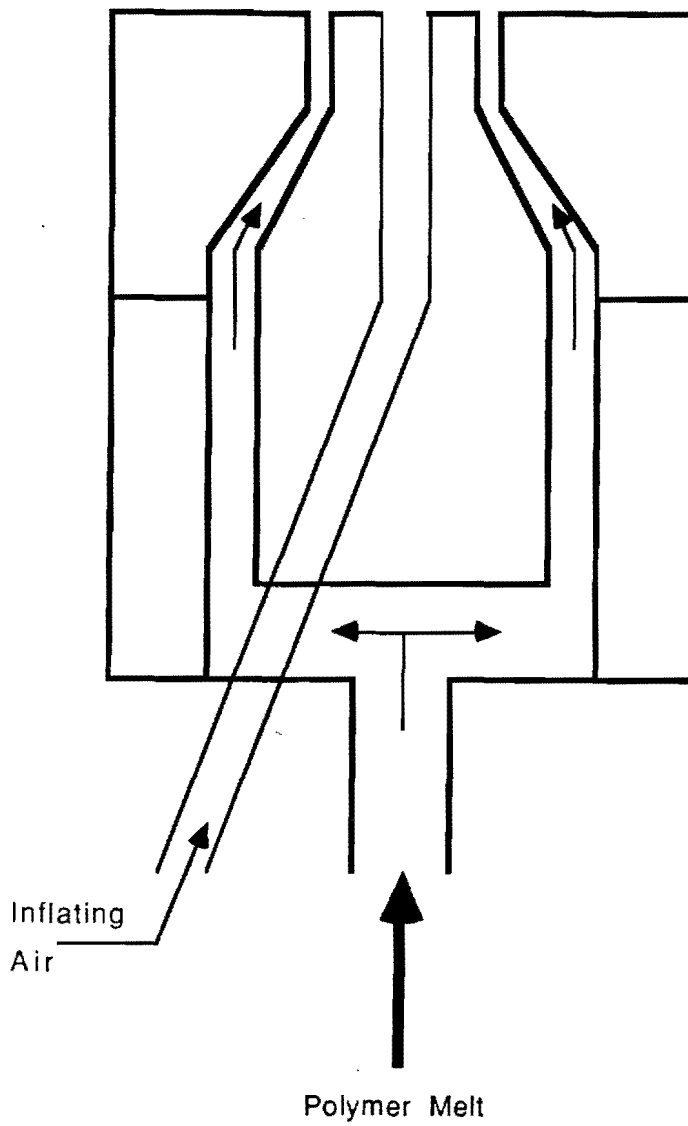


Figure 3-1 Schematic diagram of the annular die.

different draw-down ratios. The maximum take-up speed provided by this device is 9.7 cm/sec.

#### Operating Procedure and Processing Condition

About one and one-half hours before starting the extruder, all the heaters and cooling water were turned on to allow the equipment to be in a stable condition and to ensure that all residual polymer in the system had been melted. At the beginning, the screw speed, cooling air and take-up velocity (without inflating air) were adjusted to make the resin pass through the system continuously and smoothly for 15 minutes. Then gently and gradually the extruded "tube" was inflated with air. After the diameter of the tubular film reached the desired value, the inflating air was turned off.

In order to obtain the desired final products, the operating parameters, such as, the screw speed, extrusion temperature, cooling air, inflation pressure, and take-up speed, were predetermined by trial-and-error method. Thus, several initial runs were required to determine the appropriate processing parameters to obtain an optimum processing condition. The specific operating parameters are summarized in Table 3-2.

Table 3-2 Summary of the processing conditions for LL1.

<u>Temperature Settings</u>			Extruder Screw Speed (RPM)	Mass Flow Rate (g/sec)	Take-up Speed (cm/sec)
<u>Barrel Region</u> I (°C)	II (°C)	Annular Die Zone (°C)			
140	175	190	30	0.1812	2.246

### 3.3 On-line Measurement and Data Collection

#### Radius

It will be very rough and short of accuracy if the on-line diameter measurement is directly carried out by the method of contacting. This inaccuracy is mainly due to the fact that the film bubble is in a dynamic condition, rather than a static state. Since the film is in motion, the friction between the ruler and the bubble will cause this measurement to become inefficient and ineffectual.

The main techniques suggested by the literature are either to photograph the bubble [5] or to record it with a video camera [8,98]. The latter was used in this study, and the experimental setup is shown in Figure 3-2.

A video camera was placed in front of the bubble at a proper distance (i.e., in the focus region of the lens of this camera). Besides recording the bubble shape, it is necessary to photograph a piece of paper with a grid, which was placed at the center position of the bubble, to obtain the so-called "average image expansion factor" [98]. This factor is the ratio of the values of an actual scale to the corresponding values on the monitor screen. Thus, the actual radius of the bubble can be obtained by multiplying the measured value on the screen with the average image expansion factor. For the sake of accuracy, the areas near the edges of

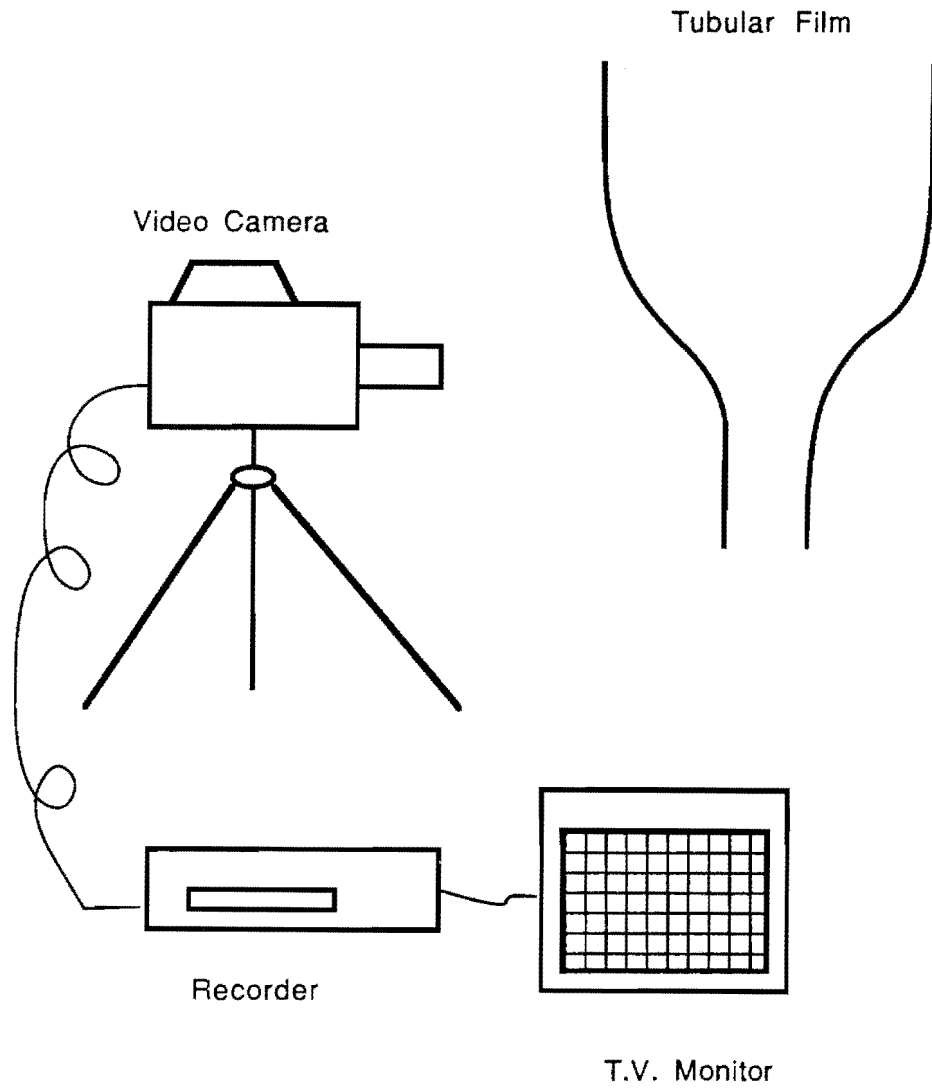


Figure 3-2 Video camera system for on-line measurement in the tubular film blowing process.

the screen should not be used for measurement because of the distortion existing in these regions.

Before proceeding to the practical experimental measurement, it is necessary to measure several static tubular films, whose diameters are known, by this technique to determine the measurement error. The results are listed in Table 3-3; and the average absolute error is  $\pm 0.11$  cm.

### Thickness

Han and Park [11] suggested that after cutting and cooling the tubular film in the region between the annular die and the nip rolls, the distribution of the thickness of film along the machine direction could be obtained by directly measuring it. However, owing to thermal shrinkage and relaxation phenomena, the thickness of the film after being cut and cooled will be different from that during processing, in which stresses and heat are applied to the whole film [15].

Hence, it seems better to obtain the thickness profile by the continuity equation [8]. Inspecting Equation(2-8), the volumetric flow rate, radius, and velocity profile are needed to be measured before calculating the on-line thickness. The radius measurement was made as in the above section, and the techniques for the measurement of the film velocity and the mass flow rate will be given in the following paragraphs.

Table 3-3 Comparison of the measured diameters by the video camera technique and that by a direct measurement.

Measured Diameters By Video-Camera Technique (cm)	Directly Measured Diameters (cm)	Absolute Values Of Error (cm)
7.13	7.28	0.15
7.53	7.57	0.04
6.33	6.44	0.11
6.20	6.35	0.15
5.07	5.00	0.07
5.44	5.28	0.16
<b>Average: 0.11</b>		



## Velocity

A detailed description of the technique for on-line velocity measurement was given by Farber [28], Farber and Dealy [8], and Huang and Campbell [98].

The setup of the video camera system used for the on-line velocity measurement was almost the same as that for the measurement of radius profile shown in Figure 3-2. The lens of the camera was placed more closely to the film and adjusted for the focus on the front surface of the bubble, rather than on the edges of it. After starting the video recording system, a round-shaped label with 5-mm diameter was gently attached on the front surface of the bubble. Thus, this label could be followed and recorded. The initial point at which the label could be observed was the position just above the air cooling ring, i.e., at 5.6 cm above the die.

Monitoring the motion of the label, a transparent plastic film with  $1 \times 1 \text{ cm}^2$  grid was attached on the screen of the television; then the time intervals between the initial point and specified positions on the screen were measured by a stopwatch. After each monitored position on the screen was transferred into the practical scale along the machine direction by multiplying with the average image expansion factor, a plot of distance versus time was obtained. Finally, the velocity profile along the machine direction could be easily determined by differentiating the above distance v.s.

time curve. The detailed calculation procedures are shown as Figure 3-3.

As mentioned above, the reliability of the on-line measuring technique must be tested and specified before it is used in the experimental measurement. Thus several initial experiments in which different throughputs and take-up velocities were set were carried out. Since the actual take-up velocity could be obtained by collecting and measuring the length of the film during a predetermined time interval, it became possible to compare this take-up velocity with the final velocity  $V_L$ , which was measured by the video camera tracing technique at the take-up position. By a similar argument, one can conclude that the value of velocity at the first point ( at  $Z=5.6$  cm) measured by camera tracing technique is reasonable by comparing with the initial velocity,  $V_0$ , at the exit of the annular die. From the measured values of throughput, the die gap and radius, the initial velocity  $V_0$  was calculated by the conservation of mass.

The comparison of the values of velocity from the video camera tracing technique and that from the direct measurement are listed in Table 3-4. The average absolute error of the take-up velocity,  $V_L$  is  $\pm 0.03$  cm/sec.

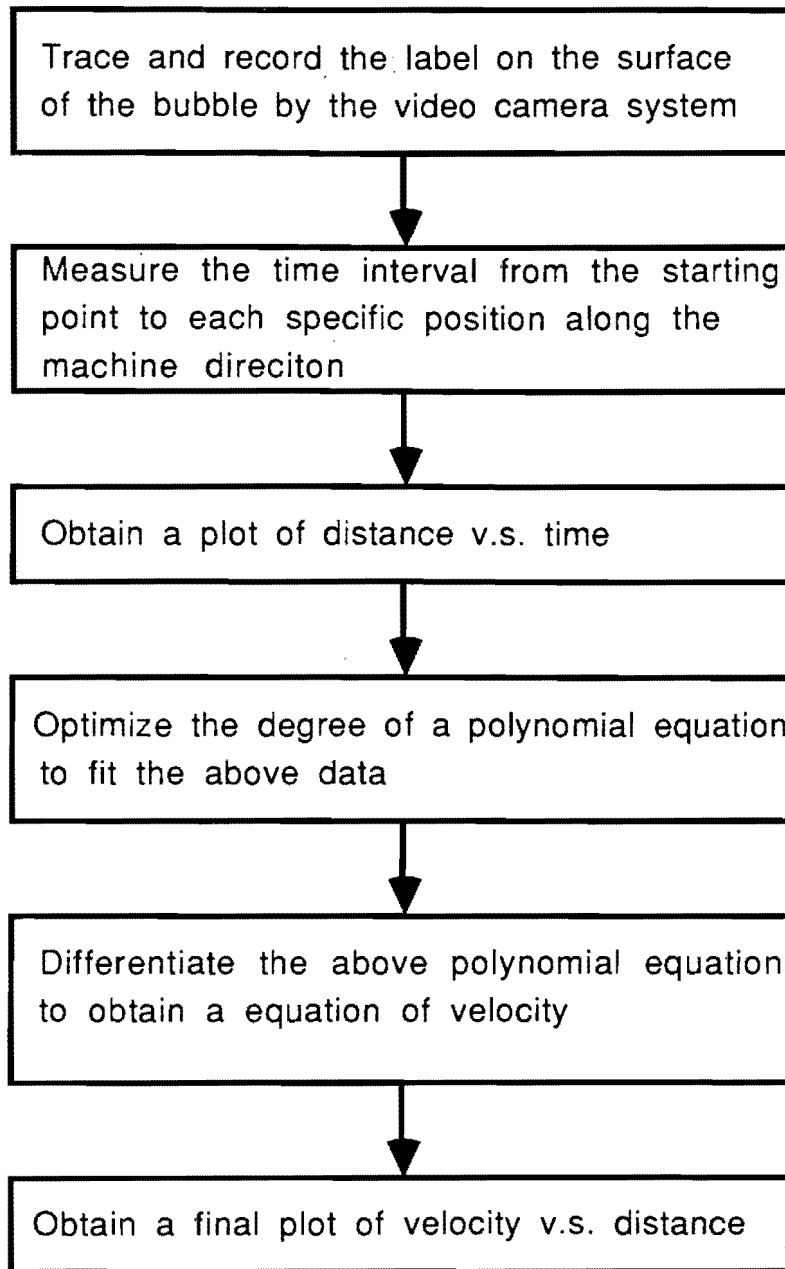


Figure 3-3 Flow chart of the calculation procedures for the on-line velocity profile.

Table 3-4 Comparison of the measured velocities by the video camera tracing technique and that by the other direct measurements.

<u>Calculated By Continuity Equation</u>	<u>Measured By Video-Camera Tracing Technique</u>		<u>Directly Measured At Take- up Position</u>
Initial Velocity $V_0$ (cm/sec)	Velocity At $Z=5.6$ cm (cm/sec)	Velocity Near $Z_L$ (cm/sec)	Take-up Velocity $V_L$ (cm/sec)
0.43	0.81	2.27	2.24
0.30	0.67	1.76	1.78
0.24	0.50	1.57	1.53
Average Absolute Error Of $V_L$ : 0.03 (cm/sec)			

## Temperature

For the on-line temperature measurement, there were two methods suggested by Fischer [9]: "Method I", in which a black body is placed behind the bubble, and "Method II", in which a black tube is vertically placed within the bubble. Since "Method II" would cause much more experimental difficulty, "Method I" was chosen in this study.

### (A) Theoretical Analysis

According to Fischer's analysis, for the "Method I" the total radiant energy,  $R_{total}$ , received by an infrared thermometer is given by

$$\begin{aligned} R_{total} = & [ \epsilon + \epsilon\tau + \epsilon\tau\rho + (\rho^2 + \rho^3 + \rho^4 + \rho^5 + \dots) ] R_f \\ & + [ \tau^2 + \tau^2(\rho^2 + \rho^4 + \dots) ] R_b \\ & + [ \rho + \rho\tau^2 + \tau^2(\rho^3 + \rho^5 + \dots) ] R_e \quad (3-1) \end{aligned}$$

in which the subscripts "f", "b" and "e" respectively denote the film, black body and environment; and  $\epsilon$ ,  $\tau$  and  $\rho$  are the emissivity, transmissivity and reflectivity of the film, respectively.

However, Cao, Sweeney and Campbell [7] thought of the whole bubble as one film, and considered that the total amount of thermal radiation,  $R_{total}$ , received by the detector is composed of the radiation directly emitted from the bubble

itself  $\epsilon^*R_f^{(b)}$ , the radiation of black body transmitted through the film,  $\tau^*R_b$ , and the ambient radiation reflected by the film  $\rho^*R_e$ . Cao et al. proposed the following equation for the total thermal radiation,  $R_{total}$

$$R_{total} = \epsilon^*R_f^{(b)} + \tau^*R_b + \rho^*R_e \quad (3-2)$$

where  $R_f^{(b)}$  is thermal radiation from an absolute (ideal) black body at temperature of the film;  $\epsilon^*$ ,  $\tau^*$  and  $\rho^*$  are apparent emissivity, transmissivity and reflectivity of the bubble, respectively. Thus, from the slope and the intercept in the plot of  $R_{total}$  versus  $R_b$ , the temperature of the film can be found. However, since Equation(3-2) was derived by considering the whole bubble as one film, the emissivity obtained from the above equation is an apparent value rather than a value for a single piece of film.

Based on the conceptual approach of Cao et. al., Equation(3-2) can be developed and modified to obtain the emissivity and temperature values for a single piece of film. Comparing with the total surface area of the whole bubble, the area detected by the thermal imaging system, which is used to measure temperature, is small enough to allow us to assume that the bubble is composed of two plain films which are parallel with each other. The distance between these two parallel films is merely equal to the local diameter of the

bubble. One of the two plain films is called "film 1", which is closer to the infrared imager, and the other one is called "film 2", which is closer to the black body. When the focus of the thermal imager is located at the surface of film 1, the total radiation received by the detector is contributed by the following:

(a) the radiation being emitted from the film 1,  
 $\epsilon_1 R_{f1}^{(b)}$ ,

(b) the radiation being emitted from film 1, reflected from film 2 and retransmitted through film 1,  $\tau_1 \rho_2 \epsilon_1 R_{f1}^{(b)}$ ,

(c) the radiation being emitted from film 2 then transmitted through the film 1,  $\tau_1 \epsilon_2 R_{f2}^{(b)}$ ,

(d) the radiation of the black body passing through film 2 and film 1,  $\tau_1 \tau_2 R_b$ ,

(e) the ambient radiation being reflected by film 1,  $\rho_1 R_a$ ,

(f) the ambient radiation passing through film 1 to reach film 2, then being reflected by film 2, and passing through film 1 again,  $\tau_1 \rho_2 \tau_1 R_a$ .

The above contributions are schematically shown in Figure 3-4, and the following equation can be obtained

$$R_{total} = \epsilon_1 R_{f1}^{(b)} + \tau_1 \rho_2 \epsilon_1 R_{f1}^{(b)} + \tau_1 \epsilon_2 R_{f2}^{(b)} + \tau_1 \tau_2 R_b + \rho_1 R_a + \tau_1^2 \rho_2 R_a \quad (3-3)$$

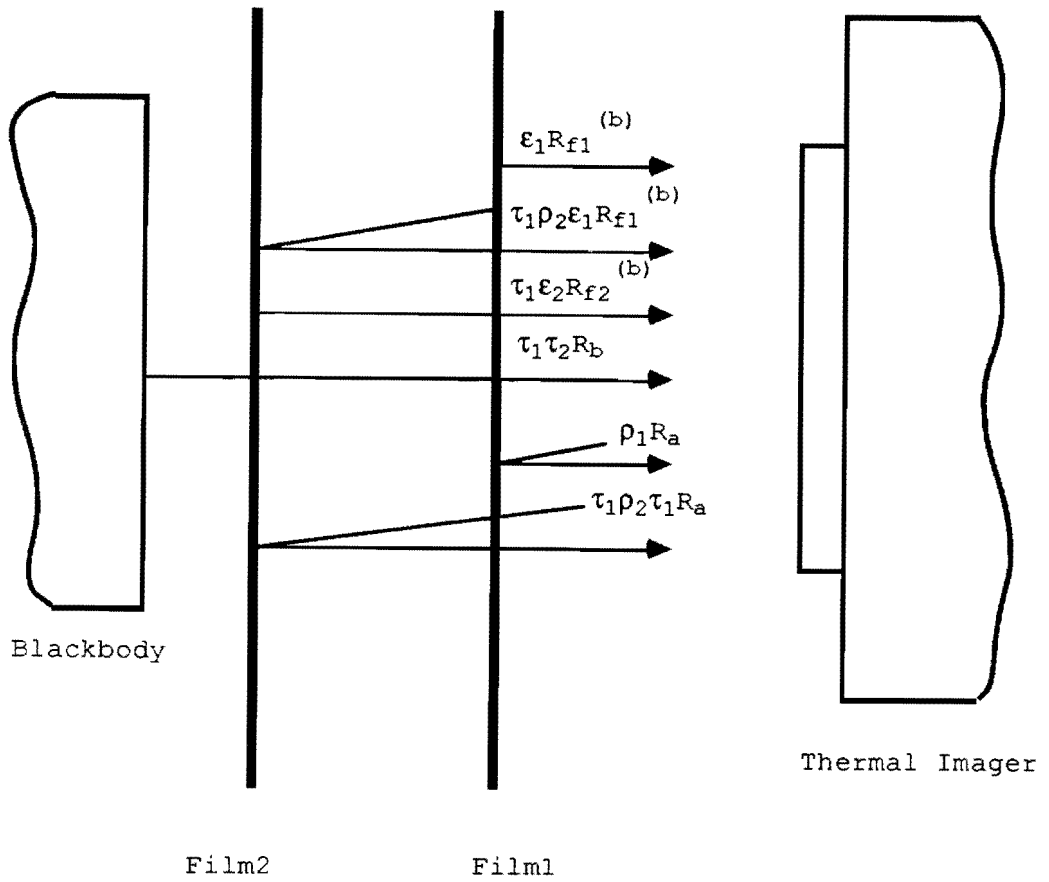


Figure 3-4 Schematic diagram of the total thermal radiant energy received by the detector of thermal imaging system.



If we assume that the bubble is axisymmetric, and its thickness and temperature are homogeneous and only depend on the position in the machine direction, i.e., both the film 1 and the film 2 are identical, we have

$$\epsilon = \epsilon_1 = \epsilon_2 \quad (3-4a)$$

$$\tau = \tau_1 = \tau_2 \quad (3-4b)$$

$$\rho = \rho_1 = \rho_2 \quad (3-4c)$$

$$R_f^{(b)} = R_{f1}^{(b)} = R_{f2}^{(b)} \quad (3-4d)$$

Combining Equations(3-4a) - (3-4d) with Equation(3-3), it can be shown that

$$R_{\text{total}} = \epsilon(1+\tau+\tau\rho)R_f^{(b)} + \tau^2R_b + \rho(1+\tau^2)R_a \quad (3-5)$$

Furthermore, a detailed comparison of Equation(3-5) with Equation(3-1), which was used by Fisher [9], shows that Equation(3-5) is an approximate form of the latter. Equation(3-5) neglected the secondary (minor) reflection in the closed bubble, i.e., the serial terms within each parentheses of Equation(3-1). Since the reflectivity of polyethylene is very small ( $\rho=0.04$ ), the secondary reflection

becomes insignificant when compared with the other primary terms. As a matter of fact, only a very small difference (about 1.15 °C, which will be shown in the next section,) exists between the temperatures of the film computed by Equation(3-1) and Equation(3-5). However, this difference is significant enough to make Equation(3-1) more preferable for calculation of the temperature profile of a tubular film.

Equation(3-1) can be rewritten in a more compact form

$$R_{\text{total}} = \epsilon \left( 1 + \frac{\tau}{1-\rho} \right) R_f^{(b)} + \left( \frac{\tau^2}{1-\rho^2} \right) R_b + \rho \left( 1 + \frac{\tau^2}{1-\rho^2} \right) R_a \quad (3-6)$$

If the following apparent quantities are defined as

$$\epsilon^* = \epsilon \left( 1 + \frac{\tau}{1-\rho} \right) \quad (3-7a)$$

$$\tau^* = \left( \frac{\tau^2}{1-\rho^2} \right) \quad (3-7b)$$

$$\rho^* = \rho (1+\tau^*) \quad (3-7c)$$

then, Equation(3-6) is given by

$$R_{\text{total}} = \epsilon^* R_f^{(b)} + \tau^* R_b + \rho^* R_a \quad (3-8)$$

A significant advantage of using Equations(3-6) through (3-8) is that it becomes possible to find out the local emissivity and transmissivity of a single film. Moreover, after these values of local emissivity along the machine direction are combined with the thickness profile, a very useful relationship between thickness and emissivity will be obtained. It will be very helpful and efficient to measure the on-line temperatures by this relationship.

Furthermore, based on Kirchhoff's law

$$\epsilon = \alpha \tag{3-9}$$

and the conservation law of radiation

$$\alpha + \rho + \tau = 1 \tag{3-10}$$

we can obtain the following relationship for the apparent quantities in Equations(3-7a) - (3-7c)

$$\epsilon^* + \tau^* + \rho^* = 1 \tag{3-11}$$

where  $\alpha$  is the absorptivity. That is, the above apparent quantities still follow the law of conservation of energy.

## (B) Data Analysis

The data read from the thermal imaging system, which is used for temperature measurement, are apparent temperature values, which cannot be directly used to obtain the temperatures of the film. These temperature data should be changed to the thermal radiation energy before proceeding to a further data analysis.

As we know, the classical Stefan-Boltzmann law for the total black body radiation,  $E_b$ , is written as

$$E_b = \sigma T^4 \quad (3-12)$$

where  $\sigma = 5.6696 \times 10^{-8} \text{ W/m}^2\text{K}^4$  is the Stefan-Boltzmann constant and  $T$  is the black body temperature in the unit of Kelvin. Equation(3-12) can be derived from Planck's expression for the energy distribution in the wavelength of a black body

$$E_{b\lambda} = \frac{dE_b}{d\lambda} = \frac{m_1}{\lambda^5 \left[ \exp\left(\frac{m_2}{\lambda T}\right) - 1 \right]} \quad (3-13)$$

where  $E_{b\lambda}$  is the spectral or wavelength distribution of black body radiant energy,  $m_1$  and  $m_2$  are constants which are calculated from the speed of light, Boltzmann's constant and Planck's constant. Integrating  $E_{b\lambda}$  with respect to  $\lambda$  at a constant temperature  $T$ , we have

$$E_b = \int_0^{\infty} E_{b\lambda}(\lambda, T) d\lambda = \sigma T^4 \quad (3-14)$$

Thus, it is very clear that the Stefan-Boltzmann constant  $\sigma$  is just a combination of the spectrum constants  $m_1$  and  $m_2$ . Hence, we know that Equation(3-12) is correct only for the condition of the whole spectrum (i.e.,  $\lambda=0 \rightarrow \infty$ ) being under consideration. However, the sensitive spectral range of the thermal imaging system used in the this study is from 2.0 to 5.6 microns. Therefore, a fractional function,  $f_e$ , should be introduced into Equation(3-12) to calculate the black body radiant energy contained within a finite-wavelength band

$$f_e(\lambda, T) = \frac{E_b(0 \rightarrow \lambda T)}{E_b(0 \rightarrow \infty)} = \frac{E_b(0 \rightarrow \lambda T)}{\sigma T^4} \quad (3-15)$$

Knowledge of this function allows us to calculate the blackbody radiant energy emitted in any finite-wavelength band ( $\lambda_1 \rightarrow \lambda_2$ ) at any temperature T by

$$E_b(\lambda_1 T \rightarrow \lambda_2 T) = (f_{e2} - f_{e1}) \sigma T^4 \quad (3-16)$$

where the values of  $f_{e1}$  and  $f_{e2}$  with respect to  $\lambda_1 T$  and  $\lambda_2 T$  are available elsewhere [99].

Since the bandwidth of the wavelength concerned in this study is fixed in the range from 2.0 to 5.6 microns, the fractional function turns into a temperature-dependent function. Hence the Equation(3-16) can be rewritten as

$$E_b = F_e(T)\sigma T^4 \quad (3-17)$$

where  $F_e(T)$  is equal to  $(f_{e2}-f_{e1})$  under the condition of fixed bandwidth. Accordingly, for different temperatures the  $F_e$ -values at the fixed bandwidth (2.0 to 5.6  $\mu\text{m}$ ) can be plotted as Figure 3-5.

Since  $\sigma$  is the Stefan-Boltzmann constant, we can express the thermal radiant energy by the term  $E_b/\sigma$ , that is, by the term  $F_e(T)T^4$ , which can be calculated from the measured temperature data. Hence, inserting Equation(3-17) into Equation(3-8) then dividing it by the Stefan-Boltzmann constant  $\sigma$ , we have

$$F_e(T_{\text{total}})T_{\text{total}}^4 = \epsilon^*F_e(T_f)T_f^4 + \tau^*F_e(T_b)T_b^4 + \rho^*F_e(T_a)T_a^4 \quad (3-18)$$

where  $T_f$  is the actual temperature of the film, and  $T_{\text{total}}$ ,  $T_b$  and  $T_a$  are the apparent black body temperatures of the total radiation, the black body and the environment, respectively. Here the referred apparent black body temperature is defined

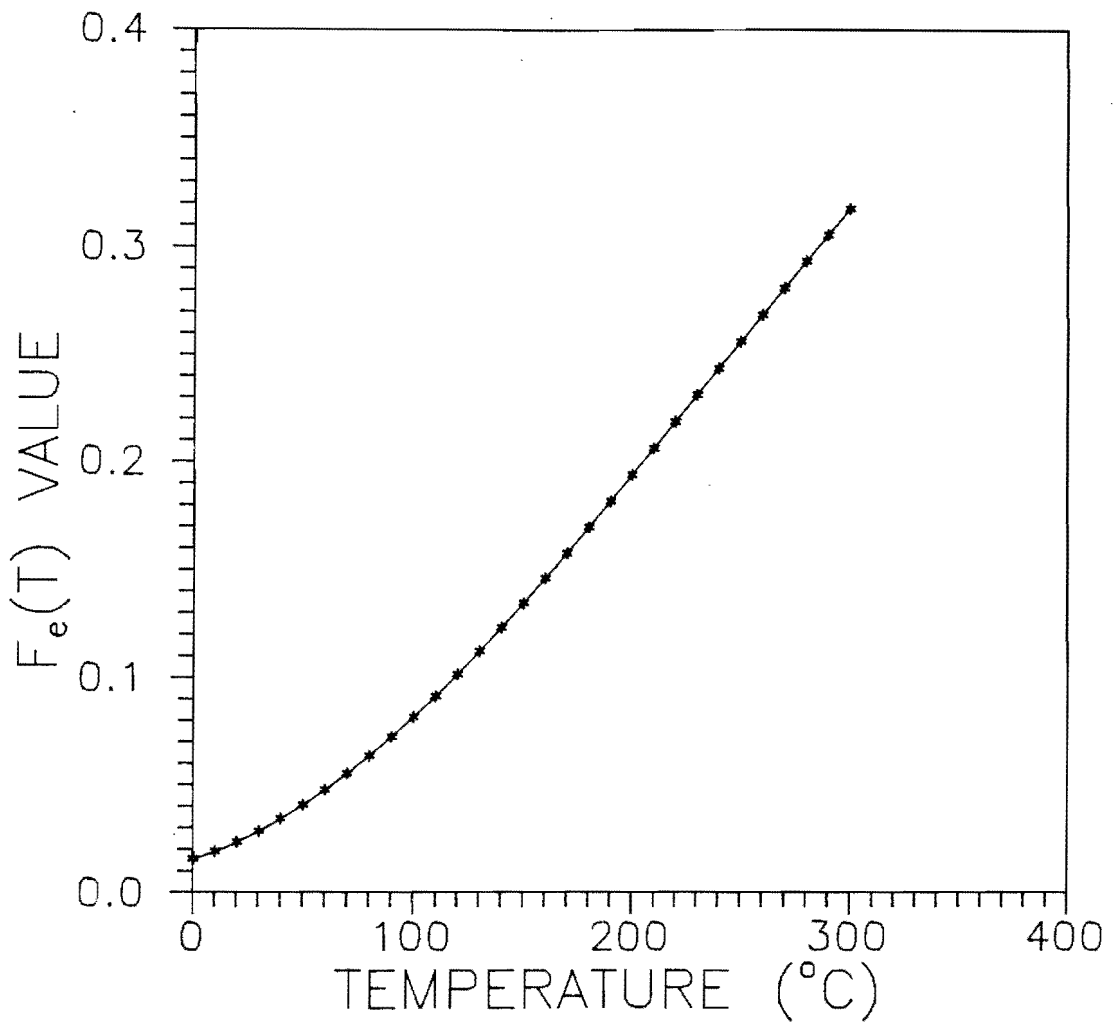


Figure 3-5  $F_e$ -values for different temperatures at the fixed bandwidth (from 2.0 to 5.6  $\mu\text{m}$ ).

as that temperature at which an ideal black body would give the same amount of thermal radiant energy [100].

Inspecting Equation(3-18) we can find that at steady state in which  $T_f$  and  $T_a$  are constant, the term on the left-hand side of this equation has a linear relationship with the second term on the right-hand side of it. That is, by changing the apparent black body temperature of the heater behind the bubble, the term  $F_e(T_{total})T_{total}^4$  has a linear response to that  $F_e(T_b)T_b^4$ . Therefore, in the plot of  $F_e(T_b)T_b^4$  v.s.  $F_e(T_{total})T_{total}^4$ , the slope and y-axis intercept of the straight line are given as

$$\text{Slope} = \tau^* = \frac{\tau^2}{1-\rho^2} \quad (3-19a)$$

$$\text{Intercept at y-axis} = \varepsilon^*F_e(T_f)T_f^4 + \rho^*F_e(T_a)T_a^4 \quad (3-19b)$$

### (C) Experimental Procedure

#### (1) The Experimental Setup

The experimental setup is schematically shown in Figure 3-6. A Hughes, PROBEYE 3300 thermal imaging system was used for the measurement of thermal radiant energy. According to the manufacturer's literature [101], the measuring range of this system is from -20 °C to 950 °C, and the wavelength band of sensitivity for this system is from 2.0 to 5.6



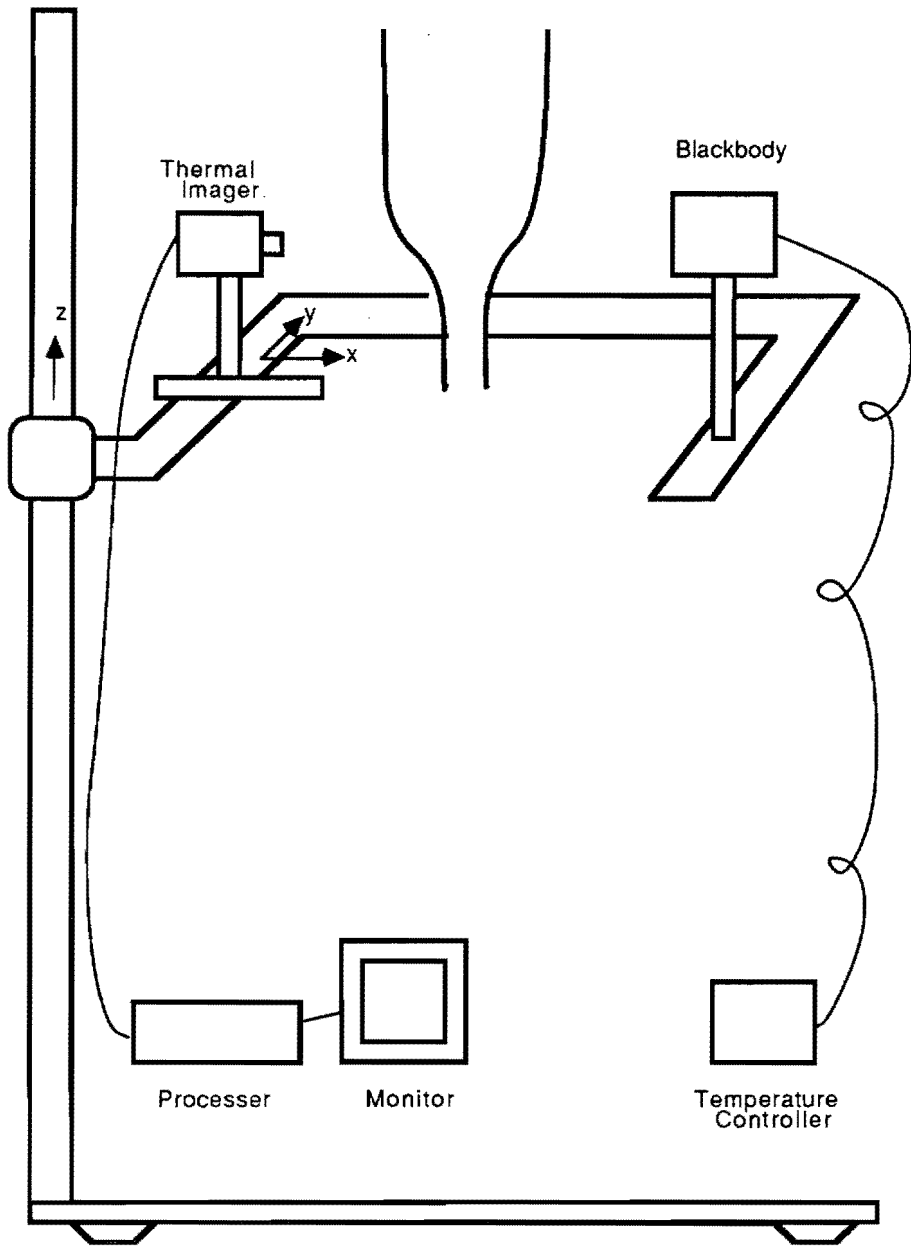


Figure 3-6 Schematic diagram of on-line temperature measurement in the tubular film blowing process.

micrometers. A black body whose temperature could be adjusted and held constant by a controller, was placed behind the bubble. The distance between the thermal radiating surface of the black body and the film is 12 inches and remains constant throughout the whole measurement.

Both the infrared imager and the black body are mounted on the horizontal arm of a stand (a lifter), which allows them to be moved in parallel along the machine direction of the blown film process. Since the radius of the bubble is varied, the base which holds the infrared imager can be adjusted in two directions (i.e., x- and y-direction) on a horizontal plane to optimize its position and the distance between infrared detector and the film.

## (2) Procedures

For the case of steady state, it is assumed that the values of temperature, emissivity, transmissivity and reflectivity of the film are only dependent on the position along the machine direction. Thus, from Equation(3-18) it can be found that a linear relationship exists between  $F_e(T_{total})T_{total}^4$  and  $F_e(T_b)T_b^4$ . In other words, the values of  $F_e(T_{total})T_{total}^4$  have a linear response to the various values of  $F_e(T_b)T_b^4$ . Hence, the temperature of film can be obtained by the regression analysis from a series of data of  $F_e(T_{total})T_{total}^4$  and  $F_e(T_b)T_b^4$ .

In order to obtain a better result, the temperature range of the black body was set to cover that of the film at a certain position which was going to be measured. Hence, several initial measurements had to be carried out to know the rough temperature distribution along the machine direction.

While measuring the temperature of film at a certain position, the relative distances between the black body, bubble and the infrared imager were kept constant till the measurement for this position was finished. First, the total radiation, i.e., the radiation contributed by two layers of film, black body and environment, was measured. Then, the black body and the infrared imager were taken aside by pulling the arm of the lifter (in order to maintain a constant distance between them), and the radiation directly from the black body was measured. Changing the black body's temperature and iterating the above steps for about ten times, a linear relationship between the total radiation and the radiation of the black body can be obtained by regression analysis. Finally, under the condition of the reflectivity being known, the apparent emissivity and temperature of the film can be calculated from the slope and intercept of the above straight line. The outline of these procedures are summarized in a flow chart, shown as Figure 3-7.

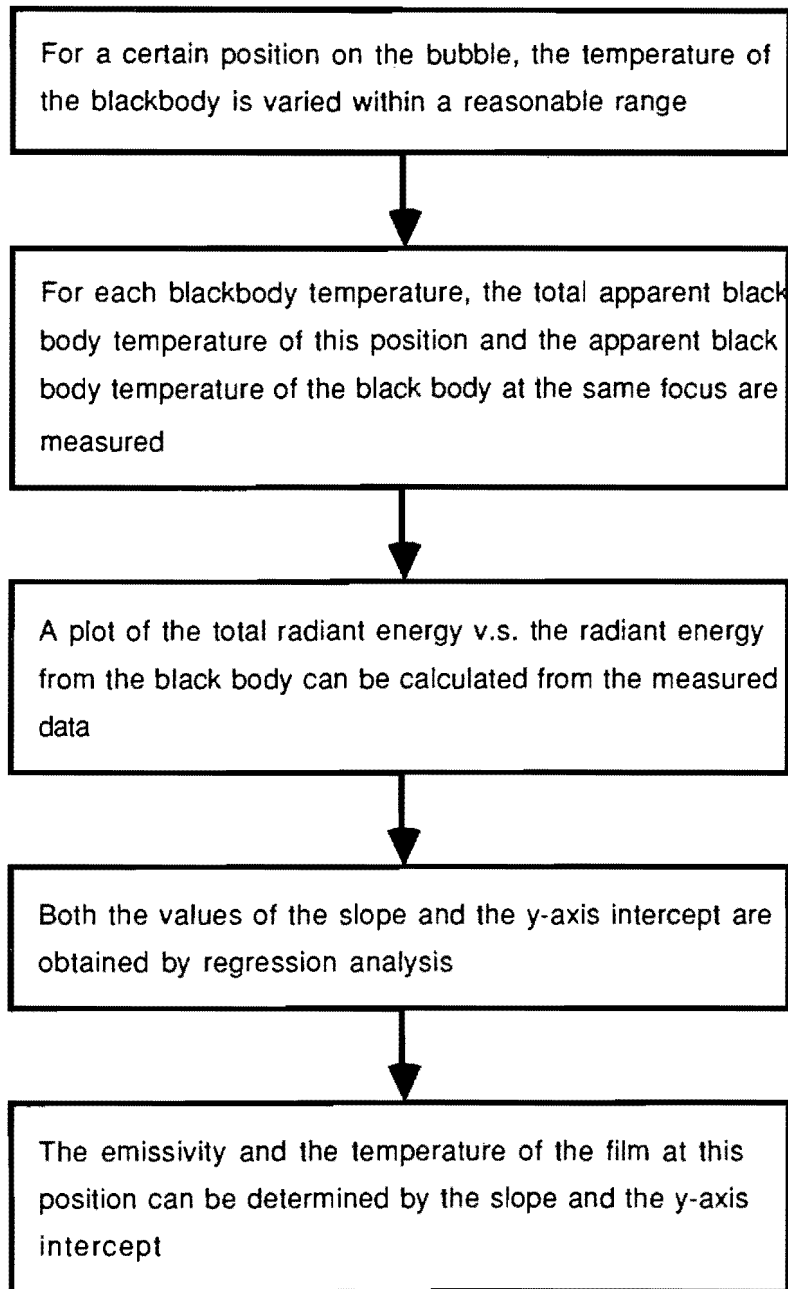


Figure 3-7 Flow chart of the procedures for determining on-line temperatures of the film.

### (3) Calibration

In order to realize the reliability of the above technique, it is necessary to examine the results of the above technique in comparison to other independent measuring methods. The best and most direct way is to measure temperature by a thermocouple. However, owing to the bubble being in motion, it is difficult and inaccurate to use a thermocouple for on-line measurement. Hence, it is necessary to use a substitutional method for the purpose of examining the accuracy.

Measuring the temperature of two static plain films were used for the above purpose. Two flat films with the same thickness were separately hung above a furnace which was used to heat the cold air from its bottom up to a certain temperature. Thus, a mild hot air current with homogeneous temperature came out from the top of this furnace and kept those two small films at a constant temperature. The schematic diagram of this setup is shown as Figure 3-8. A thermocouple was used to directly measure the temperature of the film by contacting. At the same time, the technique of on-line measurement was used to measure the temperature of the position where the thermocouple was measuring, and the data of three trials is plotted in Figure 3-9. Thus, comparing the results from two independent methods becomes possible. The comparison of these measured final results is

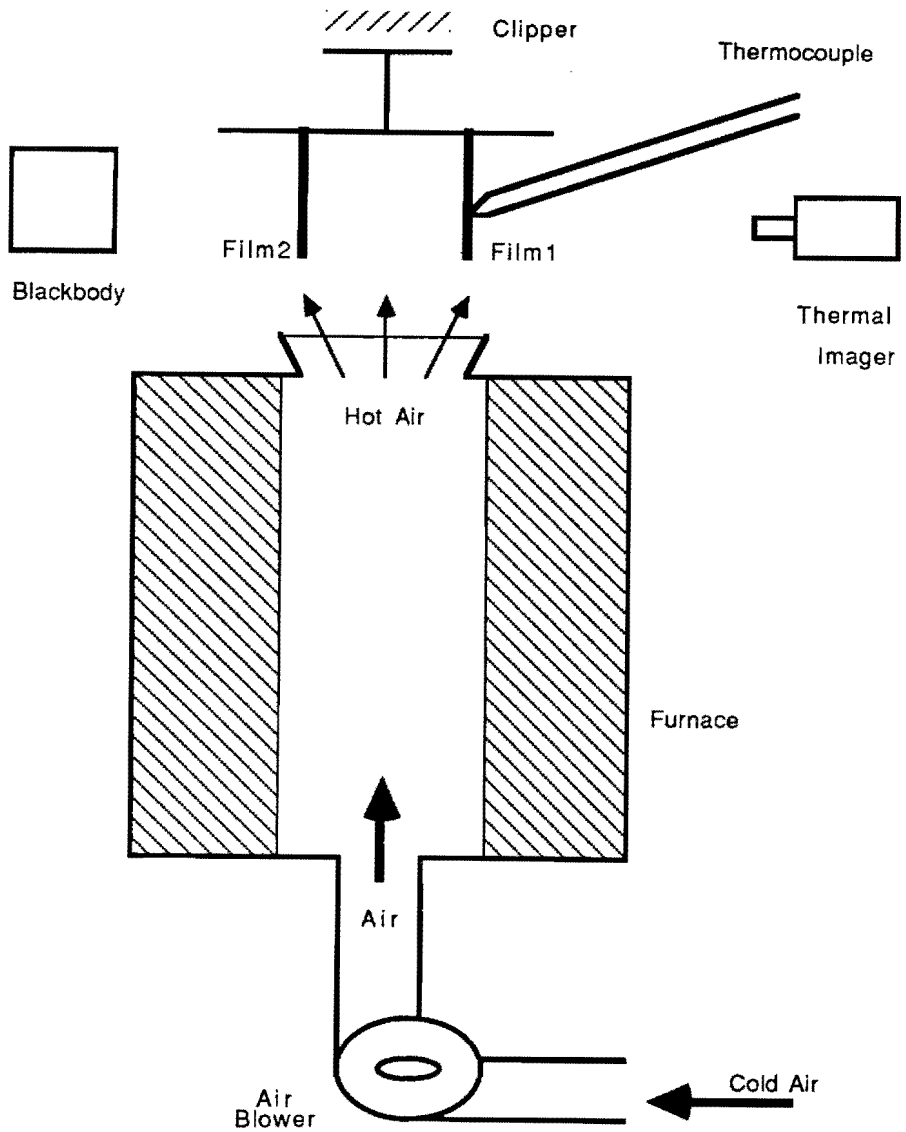


Figure 3-8 Experimental setup for the test of the on-line temperature measuring techniques.

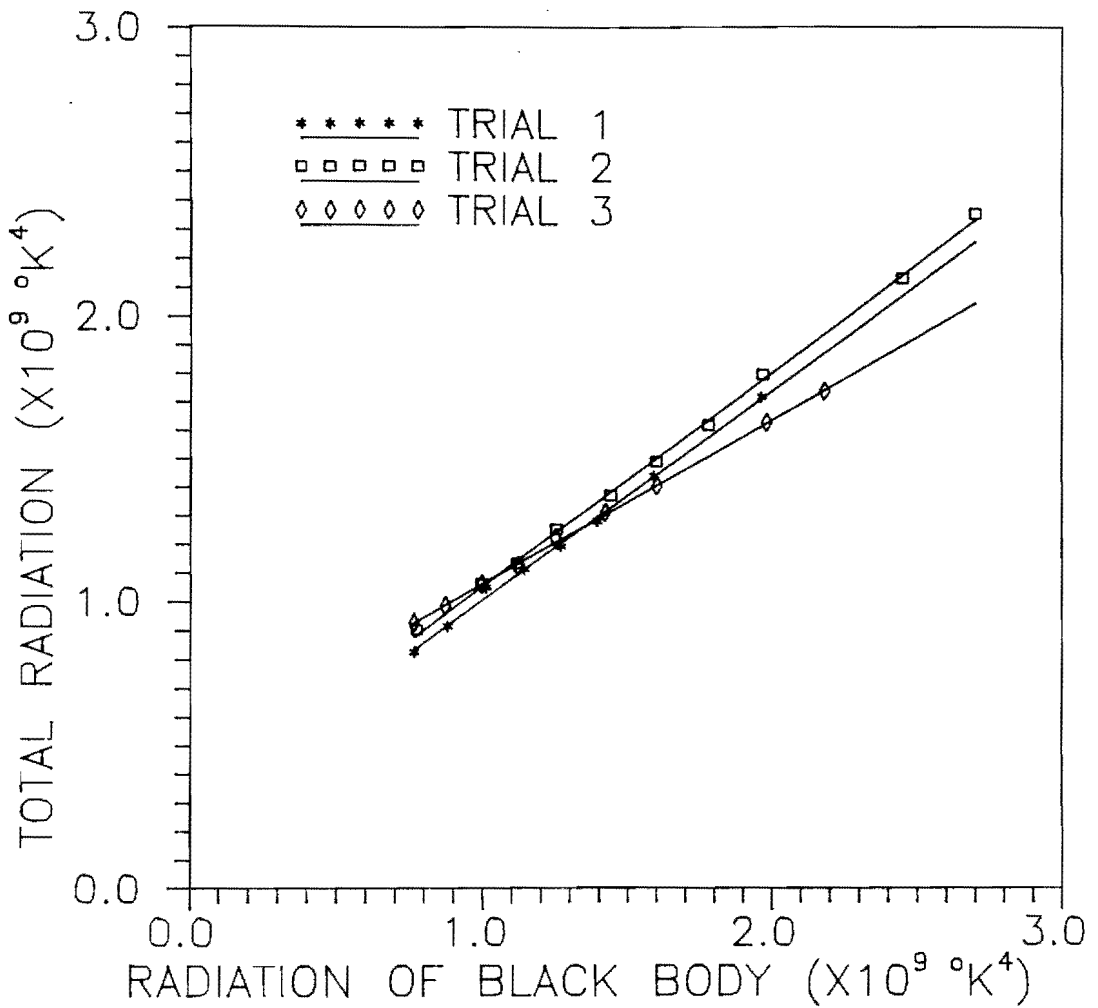


Figure 3-9 Relationship between the measured total radiation energy and the radiation energy of the black body for two static plain films.

summarized in Table 3-5, and the average error are about  $\pm 2.53$  °C.

However, the limitation of this calibration is that we have to carry out the experiment at a temperature lower than the melting temperature of the film. Hence the information for the temperature which is higher than the melting temperature is still unknown.

### Inflation Pressure

The pressure inside the bubble was measured by a water manometer. A rubber tube with a valve connected the manometer and the central part of the annular die. After the bubble reached a steady state, the valve on the tube is fully opened to monitor the inside pressure  $\Delta P$ . Recording the height difference  $\Delta h$  on the manometer, the pressure difference across the film can be calculated by the following equation [102]

$$\Delta P = \rho_w g \Delta h \quad (3-20)$$

where  $\rho_w$ , the density of water at 25 °C, is equal to 0.99708 g/cm<sup>3</sup> [102], and  $g$  is the acceleration of gravity.



Table 3-5 Comparison of the measured temperatures by the online technique with that by a thermocouple.

No. Of Trial	Film Thickness ( $\mu\text{m}$ )	Measured by Online Technique Of Temperature		Directly Measured by Thermocouple ( $^{\circ}\text{C}$ )
		$\epsilon$	$T_f (^{\circ}\text{C})$	
1	49	0.1030	91.5	94.5
2	49	0.0936	100.6	103.1
3	150	0.2002	91.6	89.5

Average of Absolute Error: 2.53  $^{\circ}\text{C}$

### Mass Flow Rate

After all of the processing conditions reached a steady state, the extruded film was collected and weighed for a predetermined time interval to obtain the value of throughput.

## CHAPTER 4

### RESULTS AND DISCUSSION

#### 4.1 On-line Measurement

The blown film extrusion was carried out under the conditions listed in Table 3-2. By adjusting the flow rate of the cooling air, the frost line was controlled at  $Z=13$  cm. Also, by carefully controlling the take-up speed and the inflation pressure, it was possible to keep the final velocity and radius constant. Thus, the final take-up ratio,  $V_L/V_0$ , and the blow-up ratio,  $R_L/R_0$ , were 5.2 and 3.9, respectively.

All on-line measured results will be described and discussed in the following sections.

##### Radius

The radius profile along the machine direction was recorded by a video camera. After calibration, the ratio of the value of a practical scale to the corresponding values on the television screen is 1.25 in both the horizontal and perpendicular direction. In other words, the actual radius of

the bubble is 1.25 times that which was directly measured on the television screen.

Because the air cooling ring was mounted on the annular die, the lowest position which could be measured was 3.6 cm above the die. After converting the measured radii on the screen to the actual values, the radius profile is shown as Figure 4-1. The polymeric melt comes from the annular die in the shape of "tube" and its radius remains approximately constant to a distance of  $Z=7.5$  cm. At  $Z=7.5$  cm, the radius of this "tube" starts to increase, and this tendency to increase ceases after  $Z=13$  cm, which is the so-called "frost line". Observing the blown film process, it was found that the transparent polymeric melt became less transparent around this position (i.e.,  $Z=13$  cm). Thus, the measured results are in a good agreement with the direct observation.

In Figure 4-1, the radius value measured directly from the final film product collected by the take-up device is denoted by a small square, which is located at the end of the radius curve. From Figure 4-1 we find that the final radius measured by the video camera is consistent with this value. However, the final on-line radius is slightly smaller than the final film radius. Neglecting experimental error, this phenomenon may be attributed to the shrinkage and relaxation effects of viscoelastic materials. The on-line measured final radius is for the bubble under the conditions of stress and a

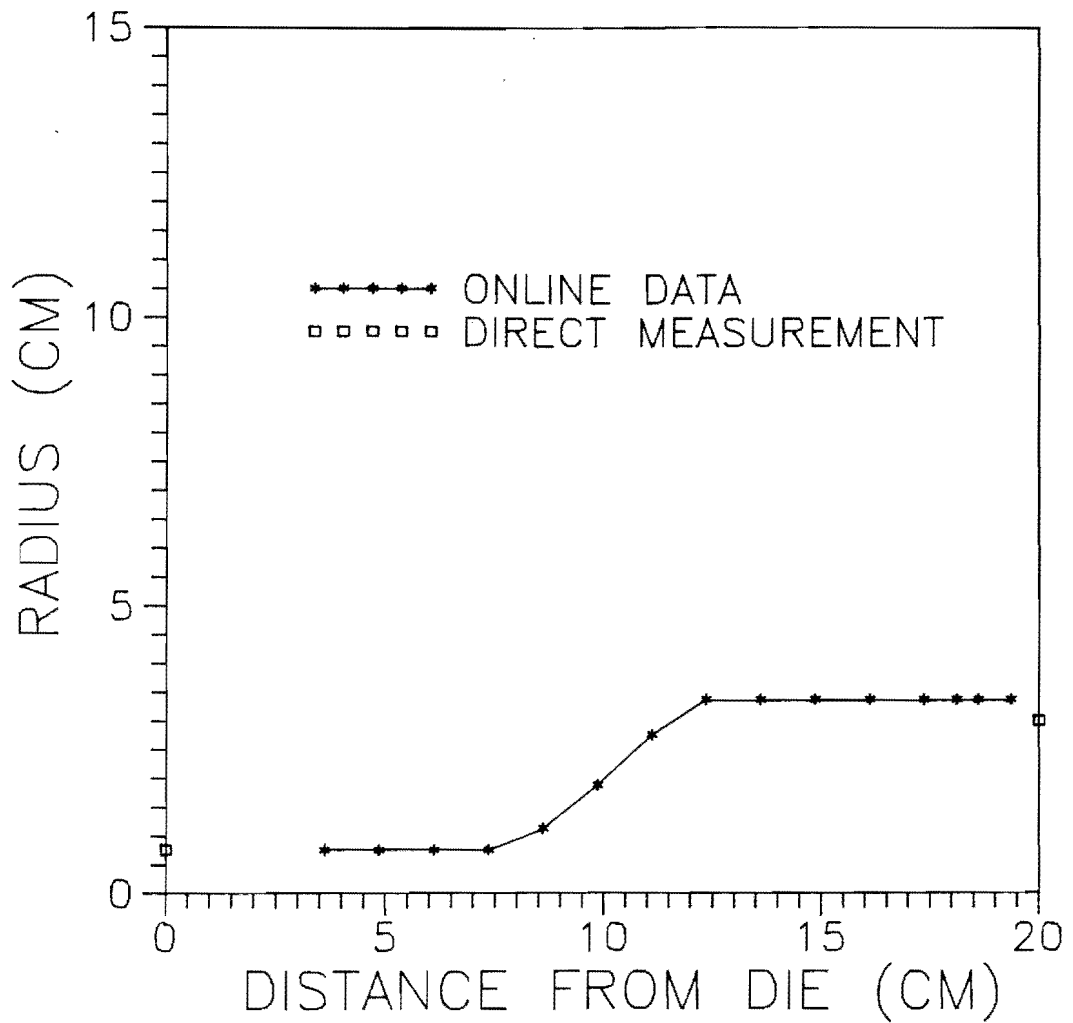


Figure 4-1 On-line measured radius profile of the bubble and a comparison with the directly measured final diameter.

temperature which is higher than the room temperature. After the film passes through the take-up device, its temperature is very close to the room temperature, and no other external forces are acting on the film. Thus, the radius of the final tubular film seems slightly smaller than that during processing.

### Velocity

The velocity profile was measured by the video camera tracing technique described in the previous chapter. The lowest position,  $Z=3.6$  cm, which could be measured, was used as a starting point. On the basis of this point, the time for the mark on the bubble travelling from the starting point to each certain position along the machine direction was measured by a stopwatch. For these certain positions along the machine direction, their vertical distances above the die and their respective travelling time interval are plotted in Figure 4-2. Inspecting Figure 4-2, we can find that a linear relationship, shown as Figure 4-3, between distance and time in the region beyond a specific point,  $Z=13.5$  cm. This means that after the polymeric melt passed this position, the velocity of the film along the machine direction approached a constant value, i.e., the slope of the straight line in Figure 4-3. However, inspecting the curve between  $Z=3.6$  cm and 13.5 cm in Figure 4-2, it is very obvious that the

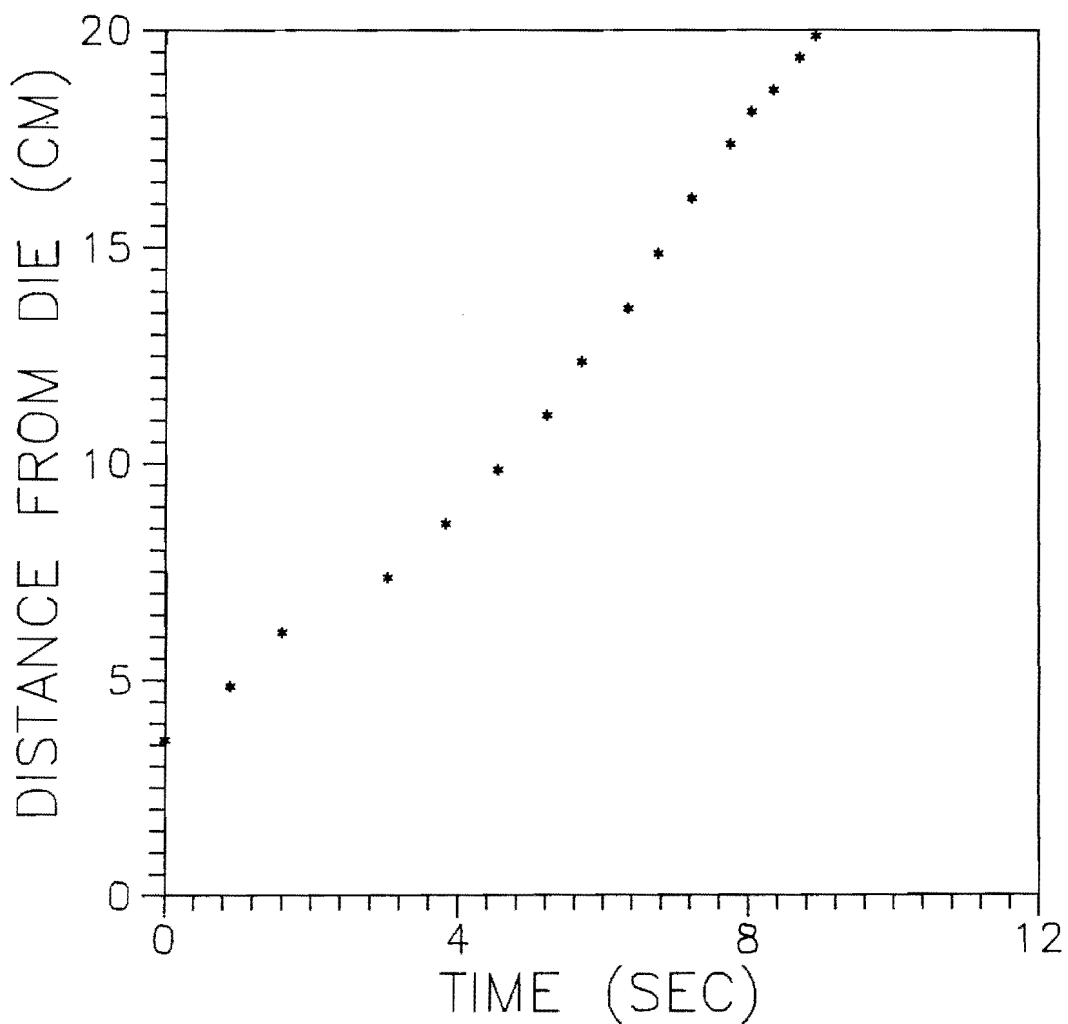


Figure 4-2 On-line measured travelling time interval of the mark for each measured position.

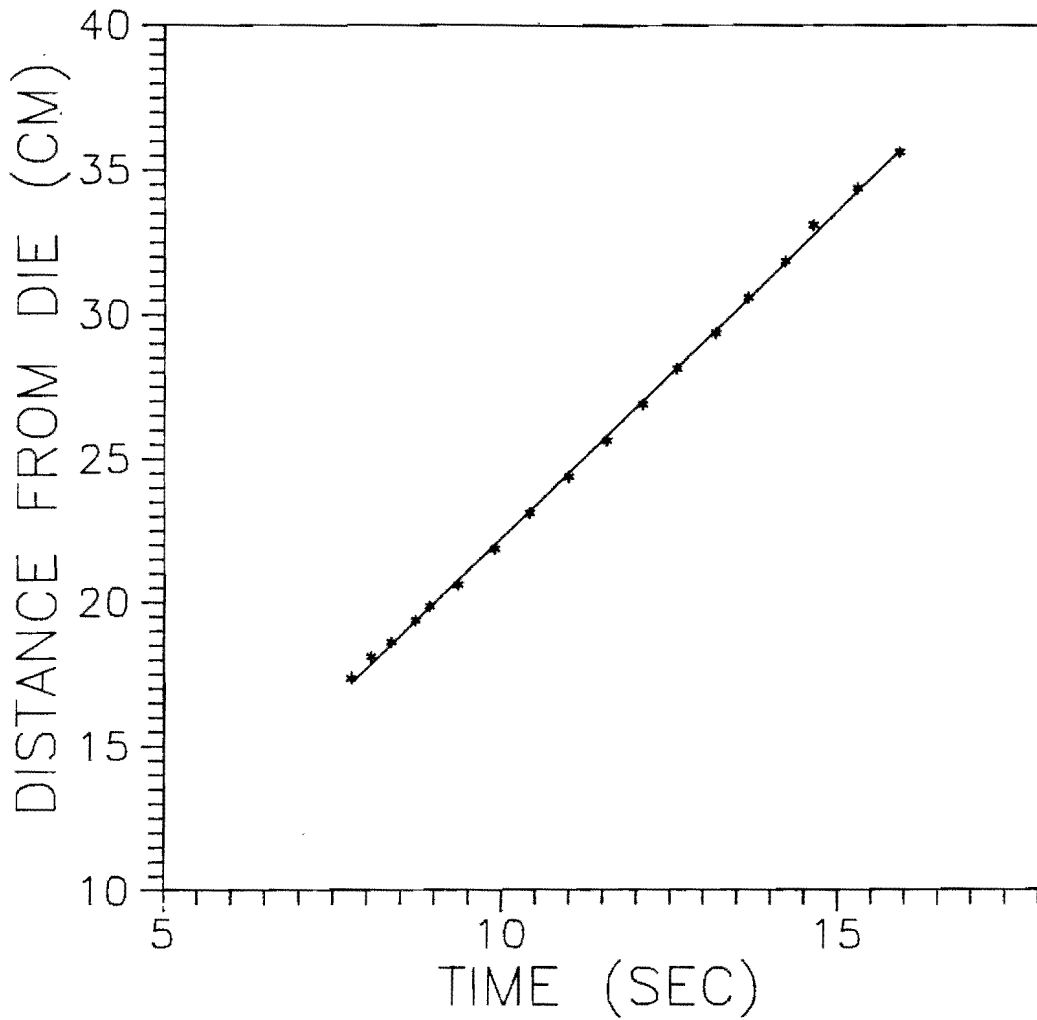


Figure 4-3 Relationship between the distance and the time interval beyond the position at  $Z = 13.5$  cm.



velocity of the film in this region is not constant. Thus, a polynomial equation with an optimum degree is used to fit this segment, and the first derivative of this best-fit equation with respect to each certain position is the local velocity of the bubble.

Hence, combining the above differentiated polynomial equation and the slope of the straight line in Figure 4-3, a complete velocity profile along the machine direction is obtained, and shown as Figure 4-4. From the distribution of the local velocity, we can find that after the polymer melt is extruded from the annular die, the velocity of the melt increases rapidly under the action of the take-up force. After the bubble passed through a critical position, e.g.,  $z=13.5$  cm in this experiment, the velocity does not increase any more and maintains a constant value.

The initial velocity  $V_0$  calculated by mass conservation, and the final velocity  $V_L$  obtained by measuring the length of the film for a predetermined time interval are denoted by two small squares in Figure 4-4. Comparing the values of  $V_0$  and  $V_L$  with the values of the both ends of the velocity profile, it is found that the on-line data is reasonable and reliable.

### Thickness

From the radius and velocity profiles, it is easy to calculate the thickness distribution from the continuity

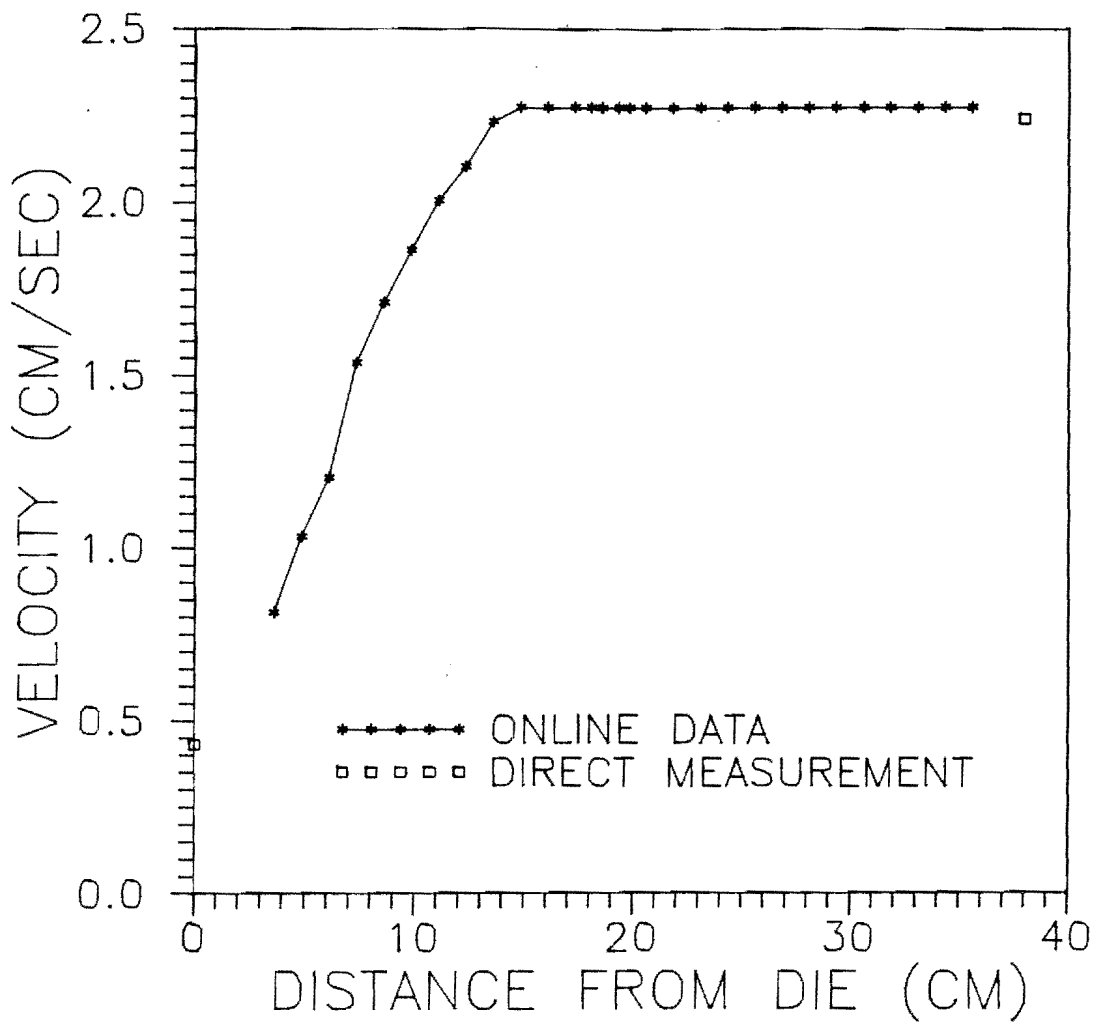


Figure 4-4 On-line measured velocity profile of the tubular film and a comparison with the directly measured data.

equation, Equation(2-8). The on-line thickness profile is shown in Figure 4-5. Under the action of the take-up force and inflating pressure, the thickness of the film decreases along the machine direction very rapidly. This tendency toward decrease in thickness ceases at the position of the observed frost line, i.e., at  $Z=13.5$  cm, then the thickness value holds constant.

There is not sufficient information about the die swell ratio of LL1. However, Lambach [103] observed the die swell ratios of the other octene-based LLDPE with various melt flow indexes in spinning line. The average value of these ratios is about 1.1. Thus it is reasonable to use the die gap (0.0953 cm) as a reference value for the initial thickness  $H_0$ , which is shown as a small square at  $Z=0$  cm in Figure 4-5. Another square in Figure 4-5 is the final thickness which was directly measured by a micrometer after the film passed through the take-up rolls. It should be noted that this measured final thickness value is slightly larger than that calculated from the on-line data. This small discrepancy is probably due to viscoelastic relaxation phenomena which cause the film to increase in thickness when the applied stresses are removed.

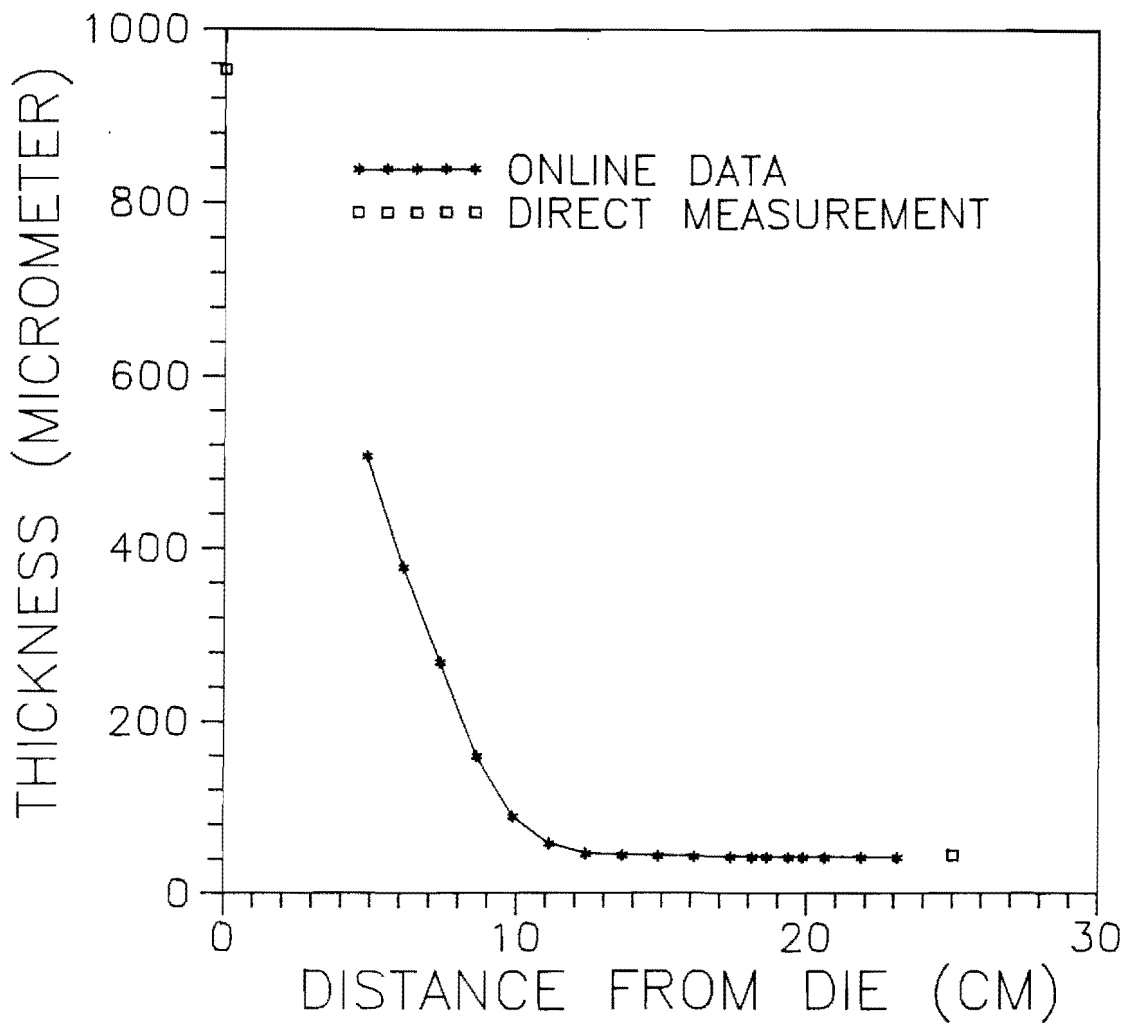


Figure 4-5 Calculated thickness profile of the film by basing on the on-line results and a comparison with the directly measured data.

## Temperature

Following the procedures of on-line temperature measurement described in Chapter 2, the values of  $F_e(T_b)T_b^4$  and  $F_e(T_{total})T_{total}^4$  for each measured position along the machine direction are plotted in Figures 4-6 through 4-8. Obviously, according to Equations (3-7), (3-8) and (3-18), a best-fit straight line can be produced by regression analysis; and the slope and the y-axis intercept of this straight line will be

$$\text{Slope} = \tau^* = \frac{\tau^2}{1-\rho^2} \quad (4-1)$$

$$\text{Intercept at y-axis} = \varepsilon^*F_e(T_f)T_f^4 + \rho^*F_e(T_a)T_a^4 \quad (4-2)$$

Observing from Figures 4-6 through 4-8, the slopes of the best-fit straight lines, i.e., the apparent transmissivity of the bubble  $\tau^*$ , increases with the positions along the machine direction at the very beginning, then holds constant. The values of the apparent transmissivity with respect to the positions along the machine direction are shown as Figure 4-9. Comparing Figure 4-9 with the measured on-line thickness profile, Figure 4-5, it is not surprising that the apparent transmissivity of the bubble is strongly dependent on the thickness of the film. As shown in Figure 4-10, when the thickness of the film stops decreasing after  $Z=13.5$  cm, the

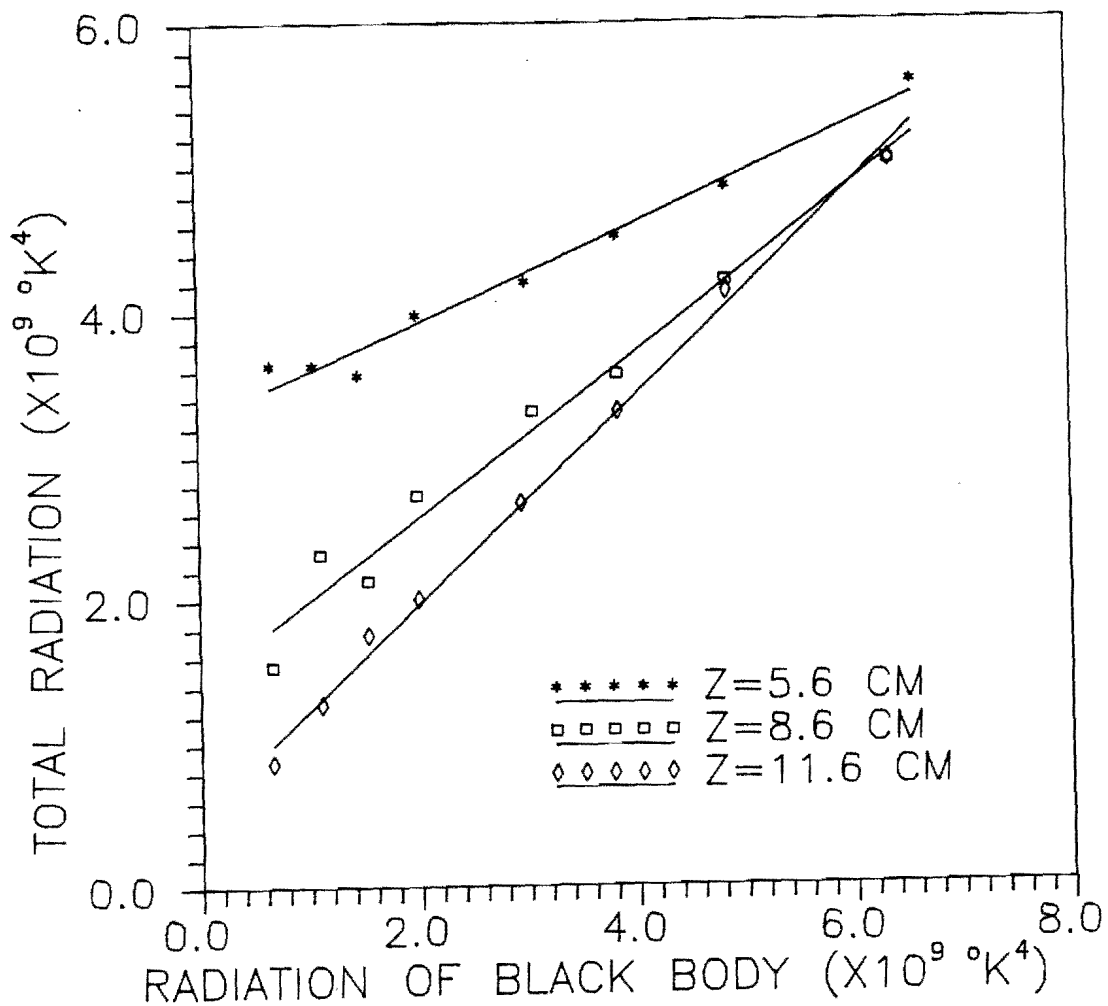


Figure 4-6 Relationship between the measured total radiation energy and the radiation energy of the black body at the positions of  $Z = 5.6, 8.6, 11.6$  cm, respectively.

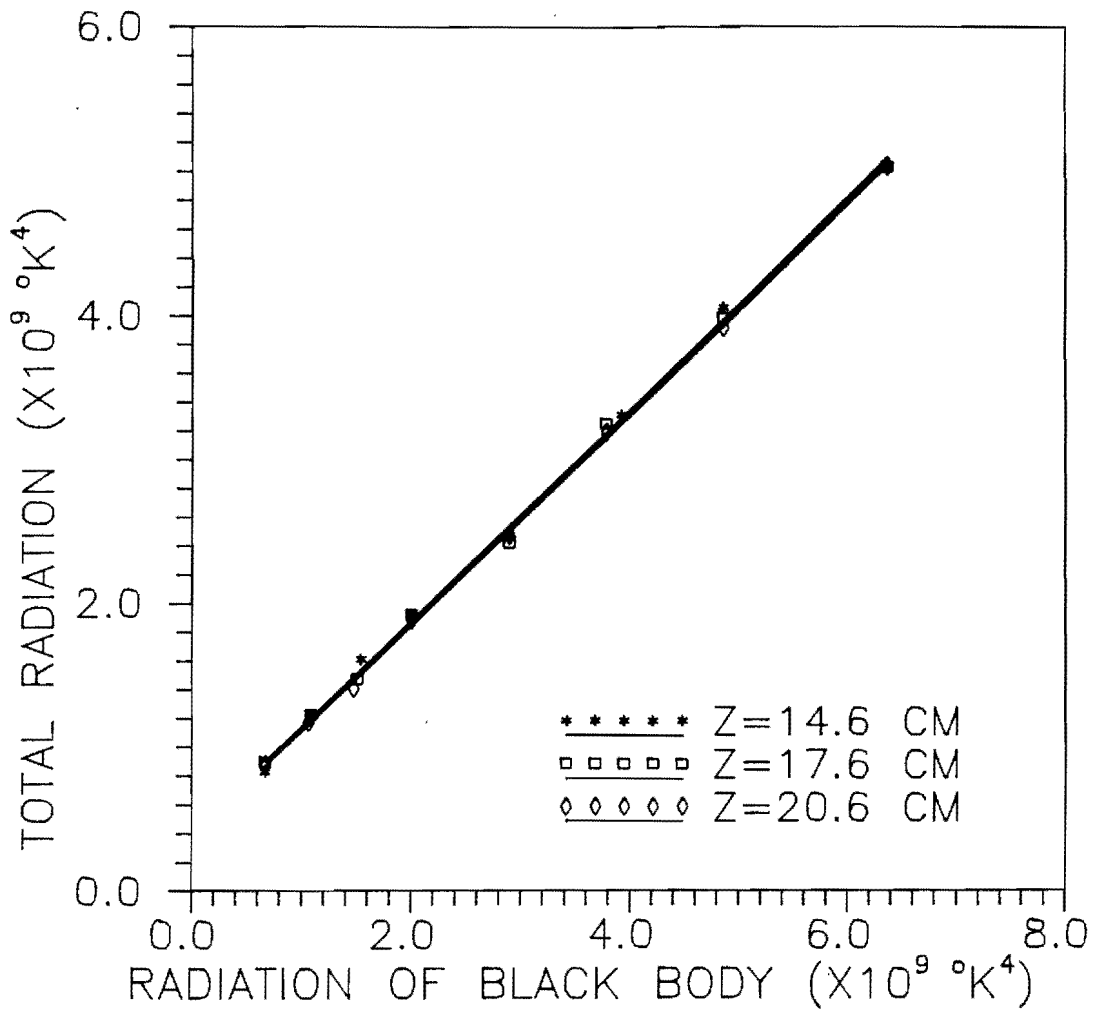


Figure 4-7 Relationship between the measured total radiation energy and the radiation energy of the black body at the positions of  $Z = 14.6, 17.6, 20.6$  cm, respectively.

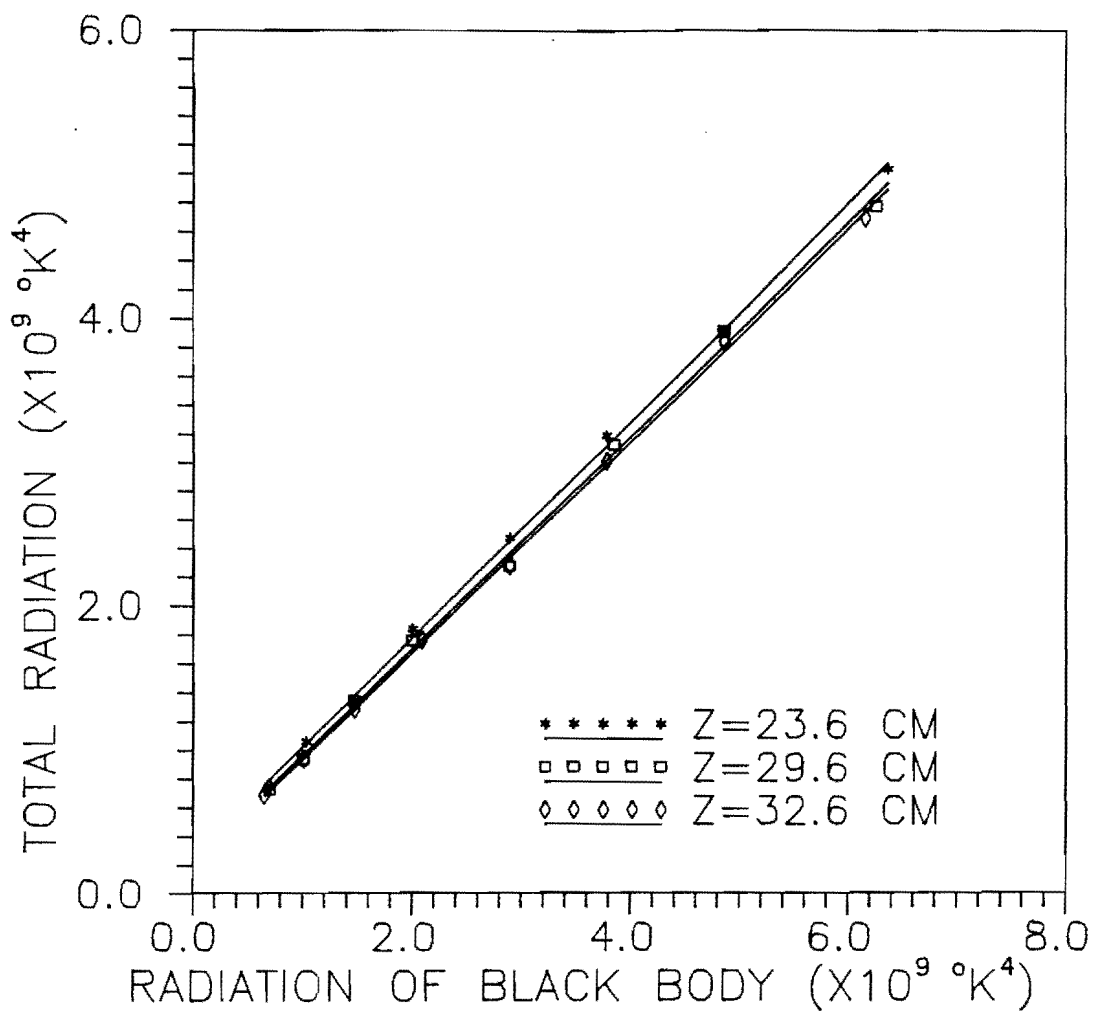


Figure 4-8 Relationship between the measured total radiation energy and the radiation energy of the black body at the positions of  $Z = 23.6, 29.6, 32.6$  cm, respectively.



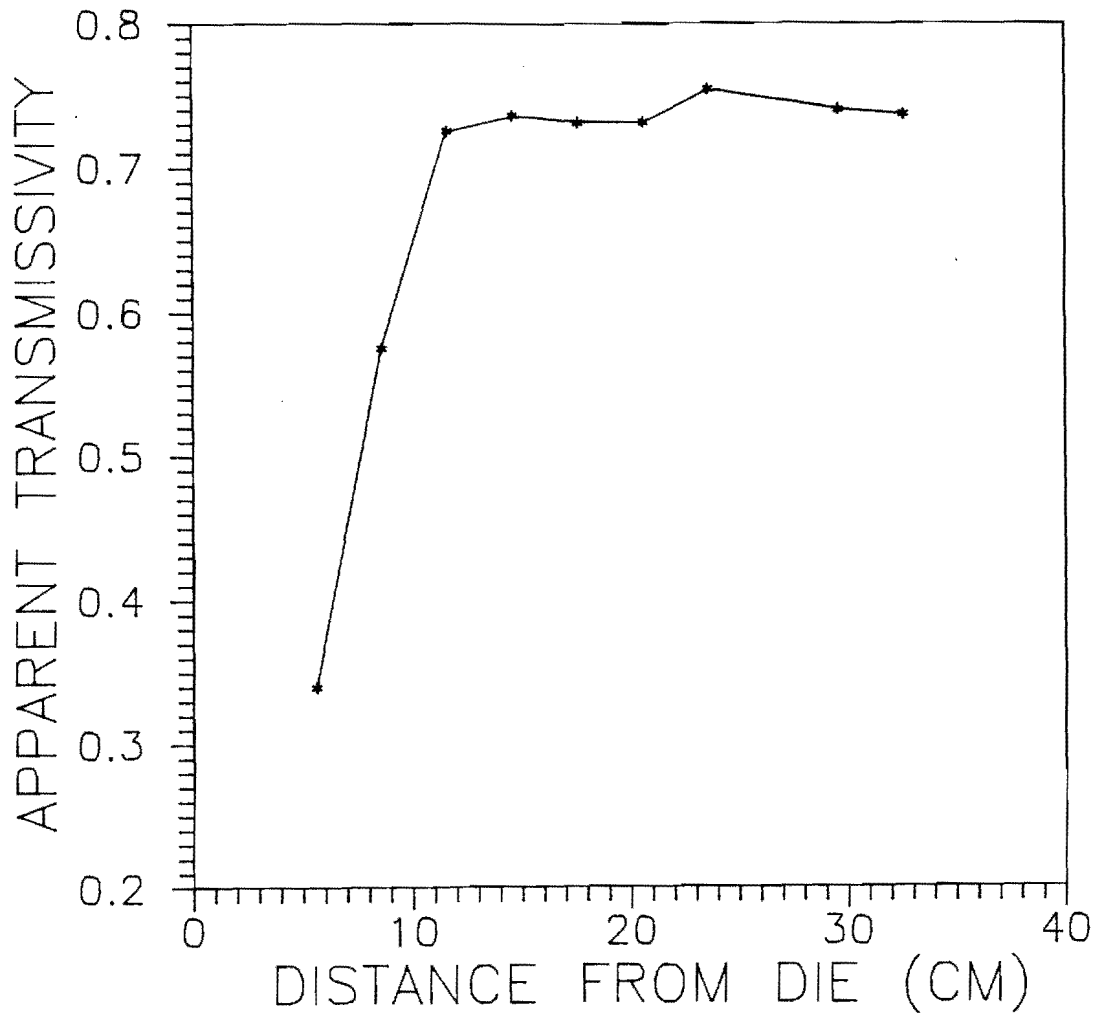


Figure 4-9 Apparent transmissivity profile of the bubble along the machine direction.

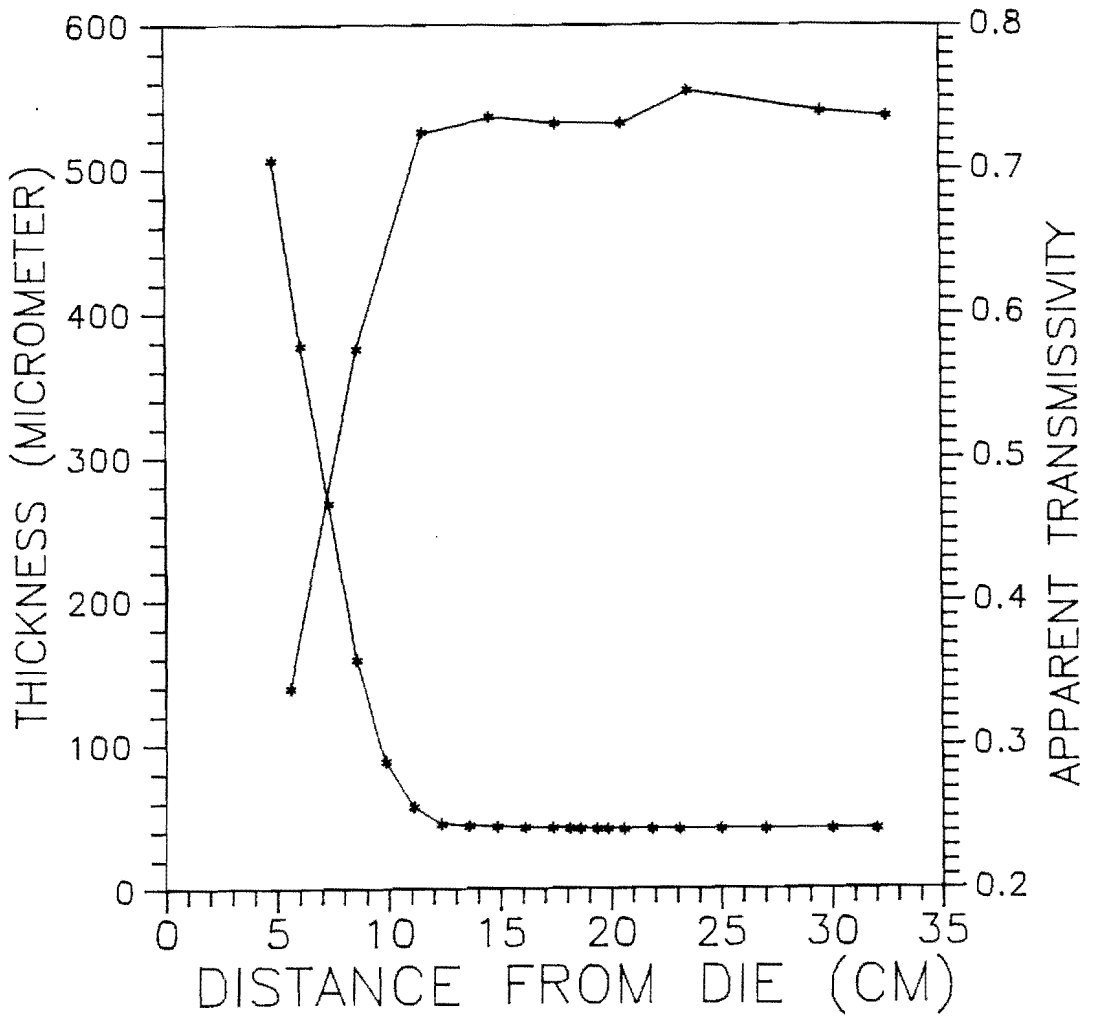


Figure 4-10 Combination of the profiles of the on-line thickness and the apparent transmissivity.

values of the apparent transmissivity also become and hold constant after this position.

Furthermore, the value of emissivity of the film along the machine direction can be obtained from the above apparent transmissivity of the bubble. Once the reflectivity coefficient of the film is specified, the on-line emissivity values can be calculated by Equations (3-7b) and (3-10).

According to the electromagnetic wave theory, the normal specular reflectance for the dielectric materials is given by [104]

$$\rho = \left( \frac{n-1}{n+1} \right)^2 \quad (4-3)$$

where  $n$  is the refractive index. Since most of the general polymeric materials are electric nonconductors, Equation (4-3) is suitable for evaluating the value of reflectivity coefficient. The average refractive index for polyethylene is 1.5 [105]. Then, from Equation (4-3) the reflectivity is equal to 0.04, which was also used in the other literature [7,9,106] for calculating the on-line temperatures. Because the value of reflectivity is not a strong function of temperature and thickness of the film [7,9], this value is taken as a constant ( $\rho=0.04$ ) through the calculation of emissivity and temperature.

Hence, from Equations(3-7b) and (3-10), the values of emissivity for a piece of film along the machine direction are obtained and shown as Figure 4-11. In case of combining Figure 4-11 and Figure 4-5, the on-line thickness profile, very useful information will be produced. The on-line data of thickness and emissivity being plotted in Figure 4-12, we can find that the emissivity is a strong function of the thickness of the film. Moreover, under the condition of the thickness being constant, the corresponding values of emissivity and temperature are plotted in Figure 4-13. Obviously, the emissivity coefficient is hardly affected by the variation of temperature. Thus, a best-fit polynomial equation for Figure 4-12 is given as

$$\epsilon(H) = 0.07558 + 7.209 \times 10^{-4}H \quad (4-4)$$

where the H is between 40 and 450 micrometer. This result is very similar to that of Hajji [100].

Equation(4-4) can be applied to simplify the complicated procedures of on-line temperature measurement for the tubular film blowing process. After the thickness of a bubble is known, the values of the apparent emissivity  $\epsilon^*$  and the apparent reflectivity  $\rho^*$  can be calculated by using Equations(4-4), (3-10), (3-7a) and (3-7c). Then, combining a

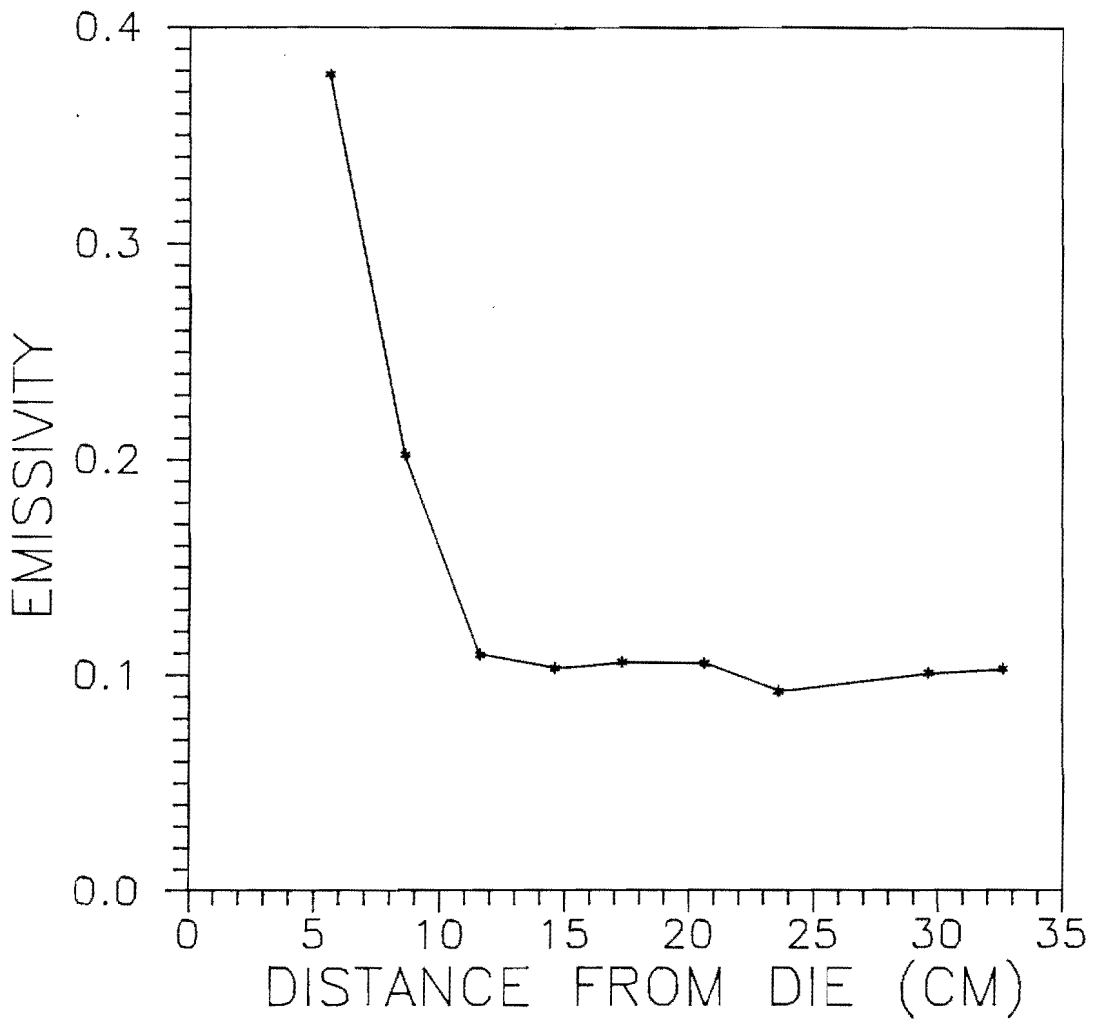


Figure 4-11 Emissivity profile of the film along the machine direction.

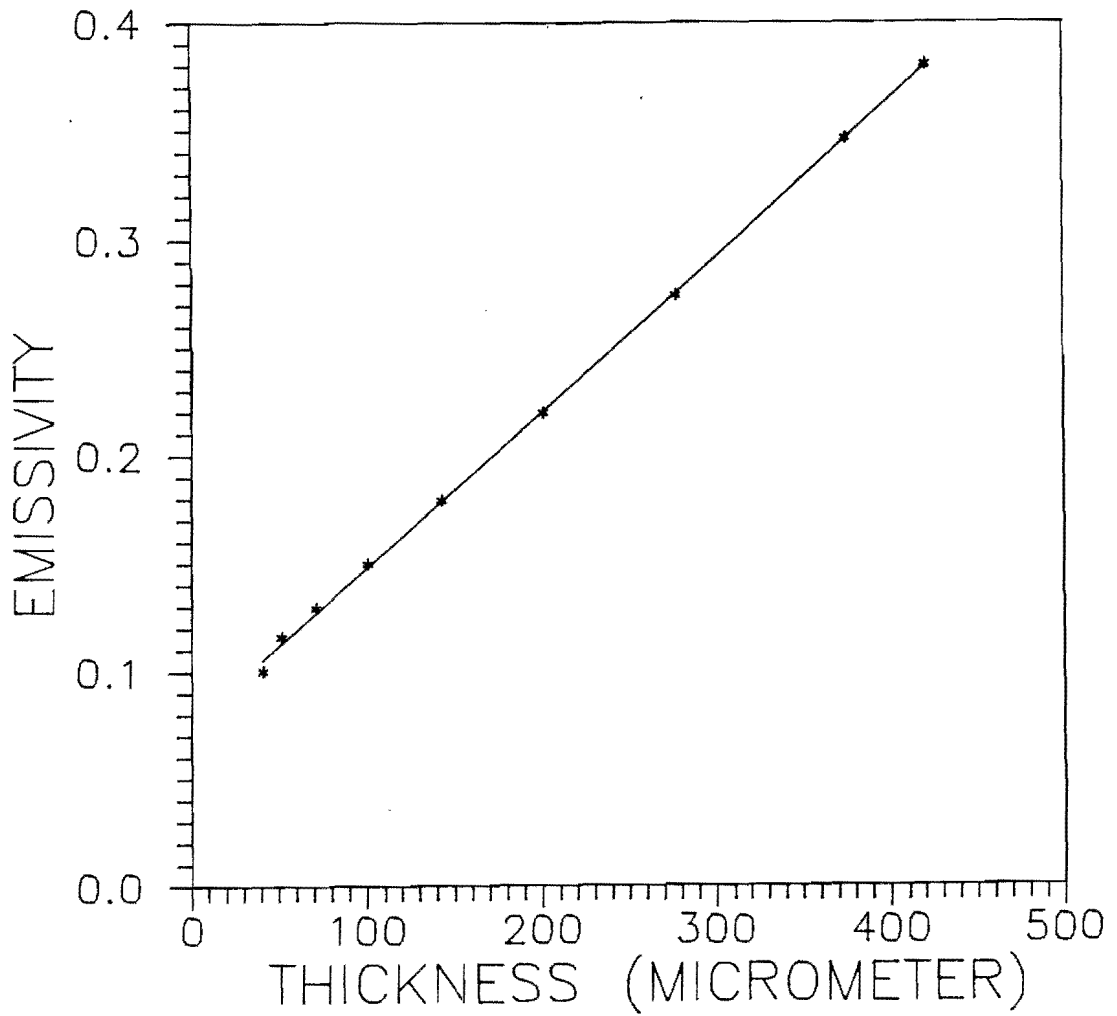


Figure 4-12 Relationship between the emissivity and the thickness of LL1.

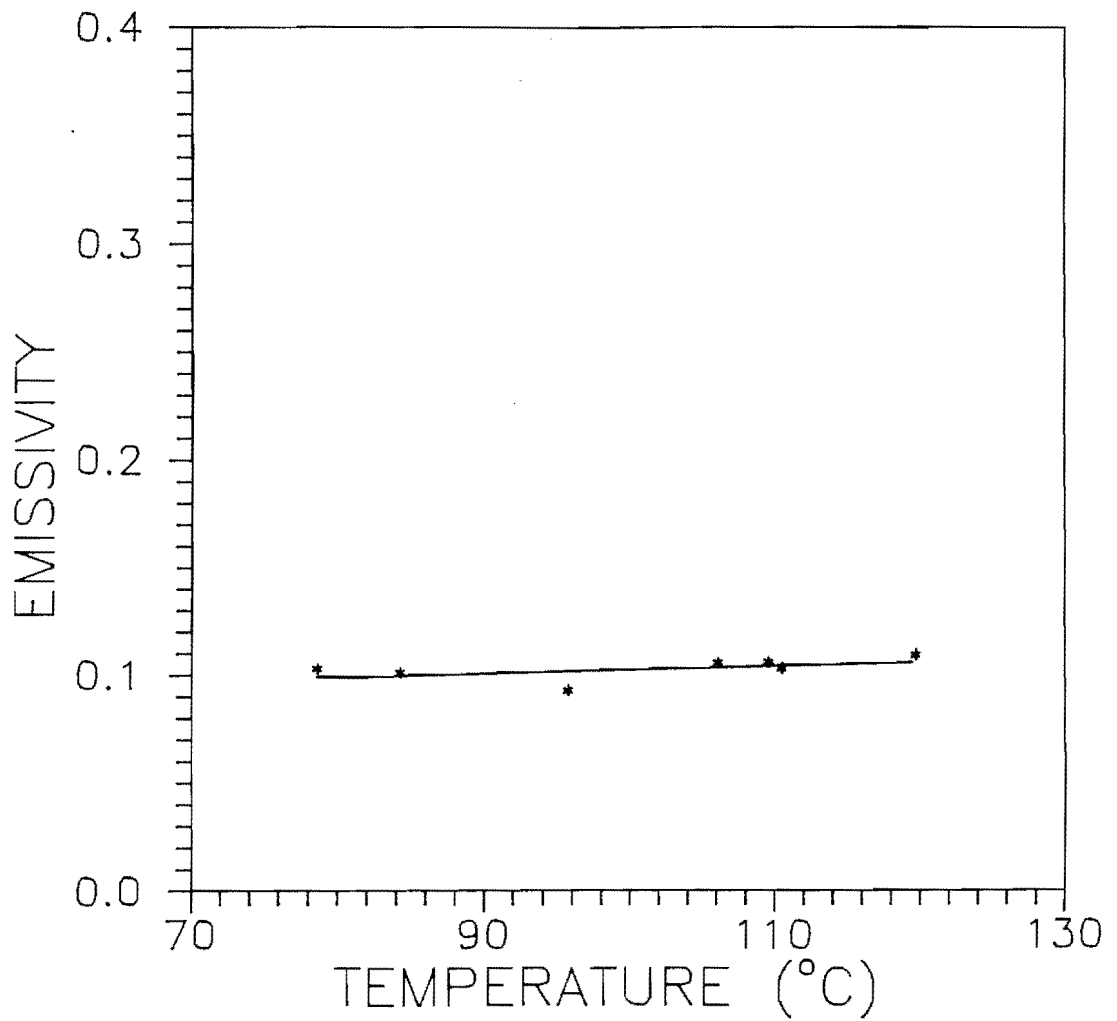


Figure 4-13 Values of emissivity under the condition of constant thickness.

trial-and-error method, the temperature of the film can be quickly obtained by the following equation

$$F_e(T_{ap})T_{ap}^4 = \epsilon^*F_e(T_f)T_f^4 + \rho^*F_e(T_a)T_a^4 \quad (4-5)$$

where  $T_{ap}$  is the apparent black body temperature of the bubble measured directly by the thermal imaging system.

From the above regression analysis for Figures 4-6, 4-7 and 4-8, the intercepts on the y-axis were obtained and summarized in Figure 4-14. According to Equation(4-2), the value of the y-axis intercept includes the contributions of the radiation emitted directly from the films and the reflected ambient radiation from the surface of the bubble. Hence it is necessary to specify the ambient thermal radiant energy before proceeding to calculate the actual temperature of the film.

The measurement of ambient radiation was carried out under the same condition as that of film blowing process. The ambient temperatures in the region above the annular die were measured. The measured apparent black body temperatures of the environment along the machine direction are plotted in Figure 4-15. These apparent temperatures increase sharply when the positions approach to the die exit. The reason why is that the region with high ambient temperatures is very



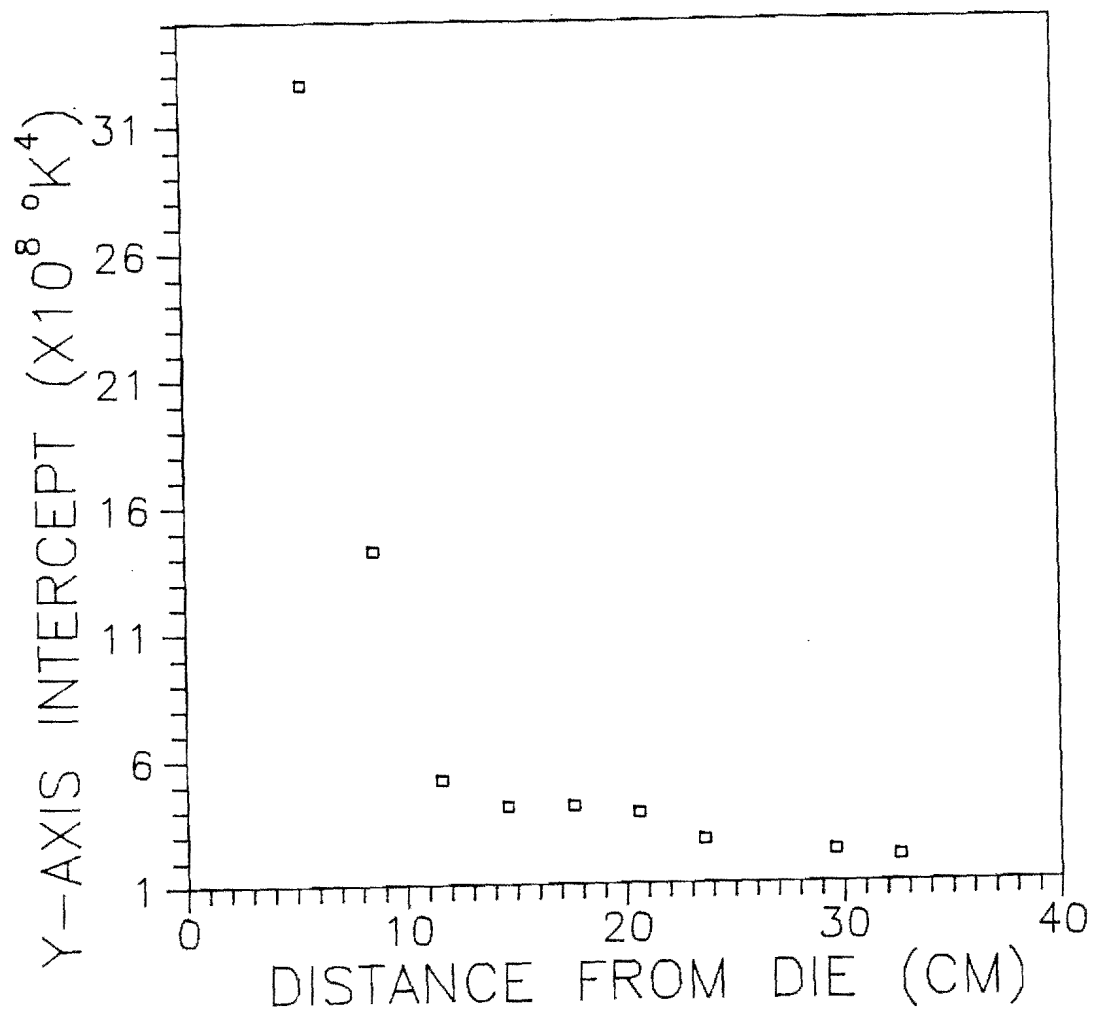


Figure 4-14 Values of the y-axis intercept from the regression analysis with respect to each measured position.

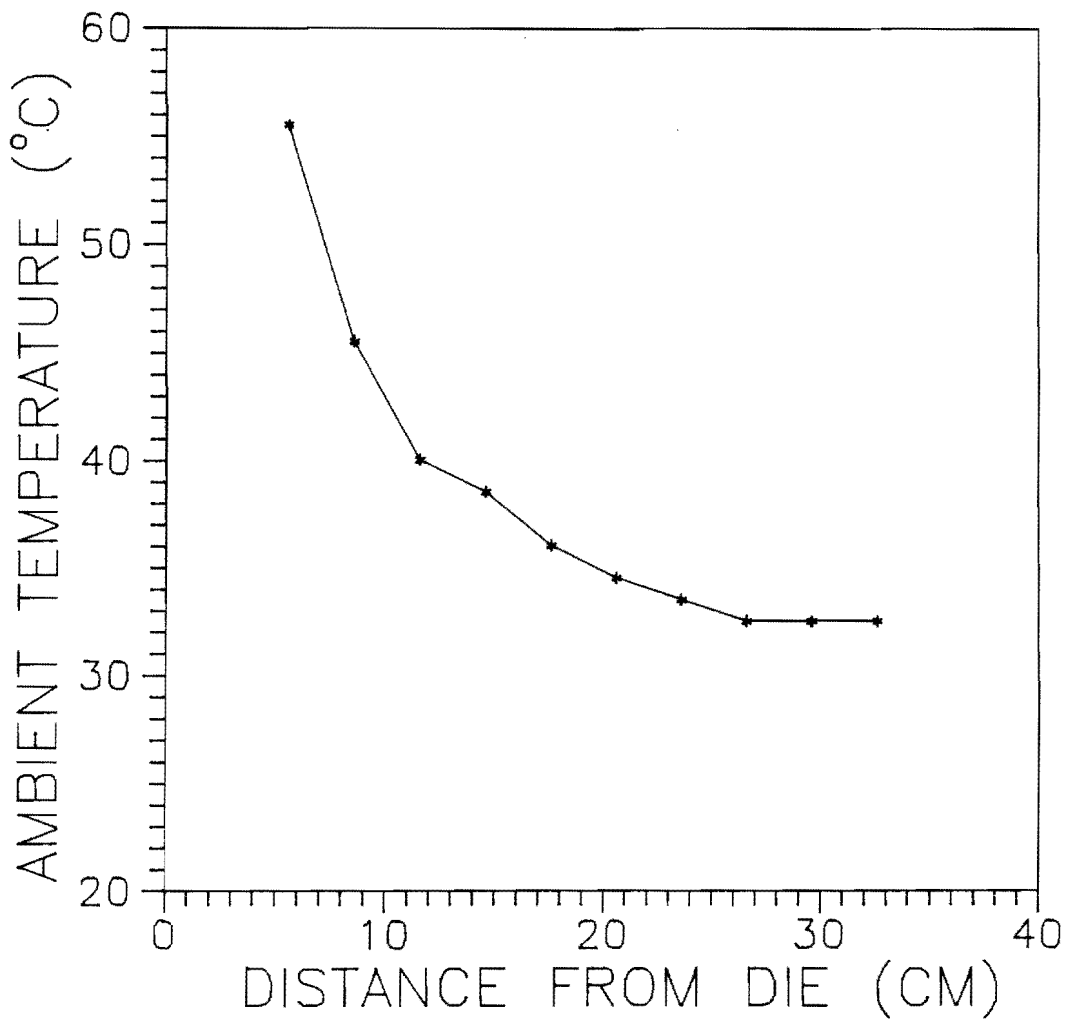


Figure 4-15 Measured apparent black body temperatures of the environment along the machine direction.

close to the extruder and the die, whose heaters are emitting a lot of thermal energy.

Based on the above information of the apparent transmissivity, reflectivity, emissivity and the ambient temperature, the actual temperatures of the film are obtained by using Equation(4-2) with a trial-and-error procedure. The final results of on-line temperature distribution along the machine direction are shown as Figure 4-16.

In Figure 4-16 the square at  $Z=0$  cm represents the initial temperature, i.e., the temperature at the die exit. Inspecting this temperature profile, a temperature plateau occurs during  $Z=14\sim 20$  cm. The occurrence of this temperature plateau is owing to the heat of fusion released from the crystallization process of polymer and it competes with the outside cooling process. Other researchers have also observed a temperature plateau of a similar shape during film blowing of polyethylene [14,98]. The temperature of this plateau is around  $110\text{ }^{\circ}\text{C}$ , which is also similar to the results for LLDPE from the other literature [98].

Moreover, it is interesting to show the insignificance of the "secondary reflection", which was mentioned in the preceding section. Following the above computation procedures, it is found that the temperatures of the film calculated by Equation(3-5) is  $1.0\sim 1.25\text{ }^{\circ}\text{C}$  higher than that by Equation(3-1). Thus, the typical contribution to the

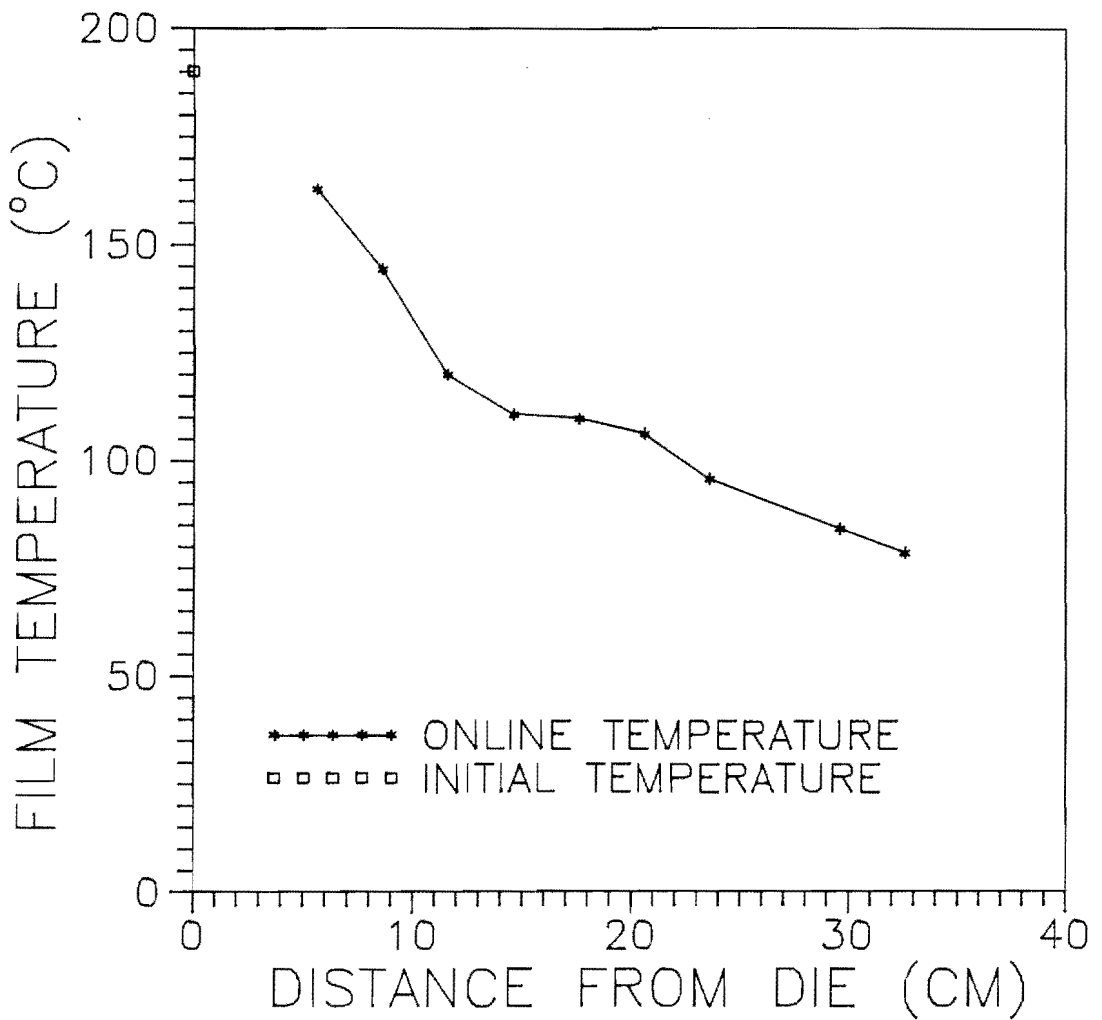


Figure 4-16 On-line measured temperature profile of the film along the machine direction.

temperature of the film by the terms of "secondary reflection" is about 0.8%.

#### Overview of On-line Data in the Blown Film Extrusion

The interaction of the various parameters is not evident when separate consideration of on-line radius, thickness, velocity and temperature data is made. A combination of these four sets of results is shown as Figure 4-17. The vertical dashed line in this figure represents the observed frost line. From Figure 4-17, at the position of the frost line, the radius, thickness and velocity cease changing, and the temperature plateau begins to occur. Furthermore, although the above distinctive behavior comes from the totally different as well as independent measurement techniques, they still occur around the same position and are in a good agreement with the observed frost line. Thus, this is additional evidence for the validity of the on-line measurements.

#### 4.2 Development of Equations for Viscosity and Heat Transfer Coefficient

The determination of viscosity equation for the polymer used and the heat transfer coefficient for the specific

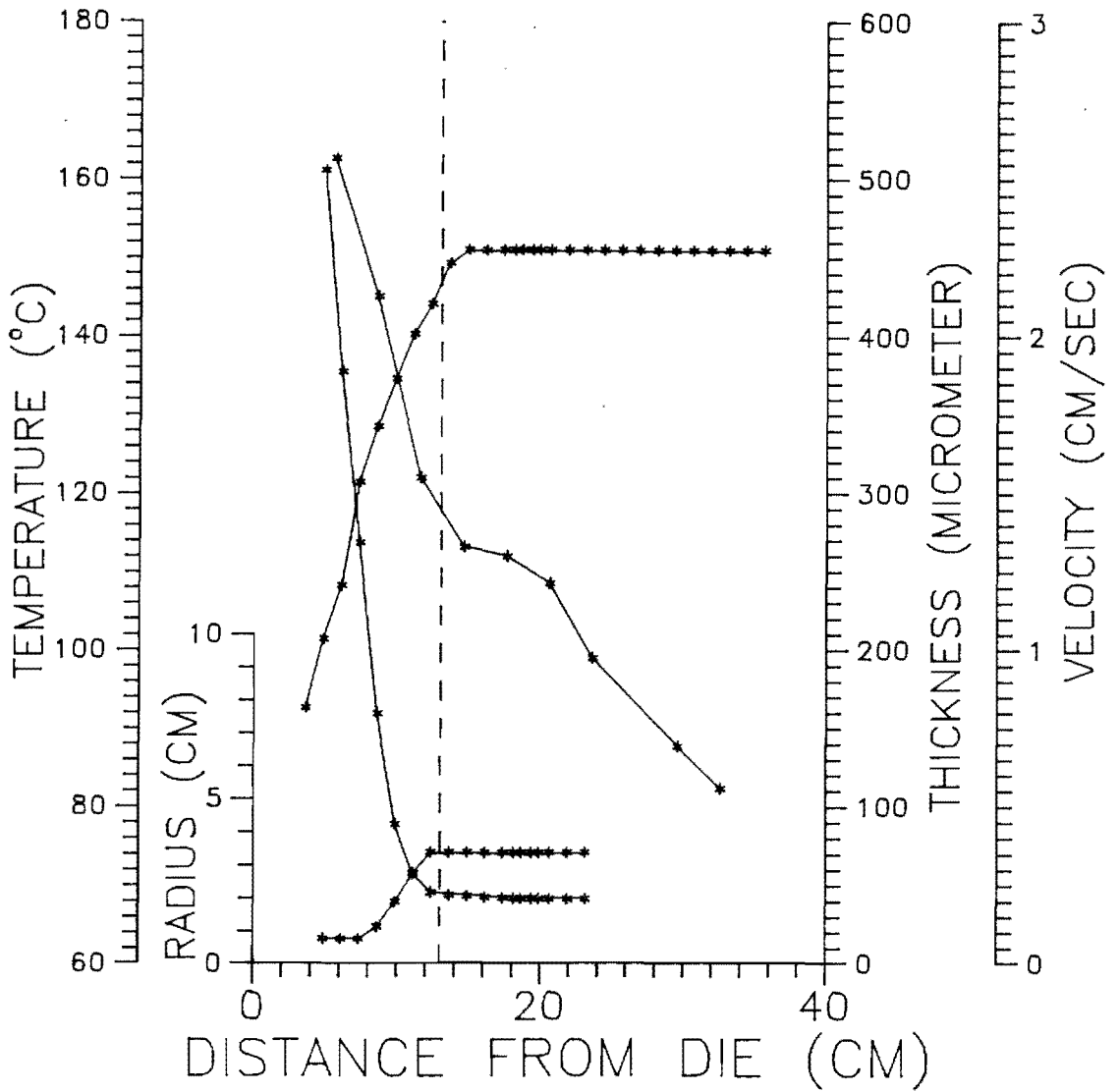


Figure 4-17 Combination of the profiles of on-line radius, thickness, velocity and temperature, and the experimentally observed frost line.

cooling conditions of the process are very important and necessary in the computer simulation of the film blowing process. A method to evaluate the apparent viscosity and heat transfer coefficient, called "inversion of computer model", was proposed by George and Deeg [107]. Thereafter, this method was successfully applied to the experimental data in a series of studies for the melt spinning process in our laboratory [82,103,108,109]. A detailed explanation of the inversion procedure was described by Bheda [108].

#### Equation of Viscosity

According to the inversion procedure, information about the experimental temperature, radius and thickness profiles and the measured tension force is required to obtain the apparent viscosity equation. However a tensionmeter for the film blowing process is not available in our laboratory. Thus, the following approaches are used to estimate the apparent viscosity for LL1, which was used in this study.

The apparent elongational viscosity of LL1 was estimated directly by using the inversion procedure on data taken in the fiber spinning process. During the spinning of LL1, the on-line temperature and diameter and the final tension force were measured by Zhou and Hajji [110]. The detailed measuring techniques and instruments were described by Hood [109]. The measured temperature and diameter profiles are shown as

Figures 4-18 and 4-19. The apparent elongational viscosity can be calculated by a BASIC program for the inversion procedure, which was developed by Patel et al. [111]. Assuming the melt to be a Newtonian fluid, the calculated elongational viscosity with respect to temperature is shown as Figure 4-20. Unfortunately, at some certain positions along the spinning line, the broad distribution of the values of diameter causes a "bump" on the curve in Figure 4-20. Although this viscosity curve is not smooth, these values still represent the right order of the magnitude for the elongational viscosity.

A compromise straight approximation to the data in Figure 4-20 was made such that the subsequent predictions in the blown film modelling will be reasonable. The approximation is shown as the dotted line which can be fitted with the following equation

$$\eta_e = 2491 \exp\left[\frac{2523}{T}\right] \quad (4-6)$$

While the line has been adjusted to give plausible results in the blown film modelling, it is nonetheless in reasonable agreement with the independent melt spinning data shown in the figure.



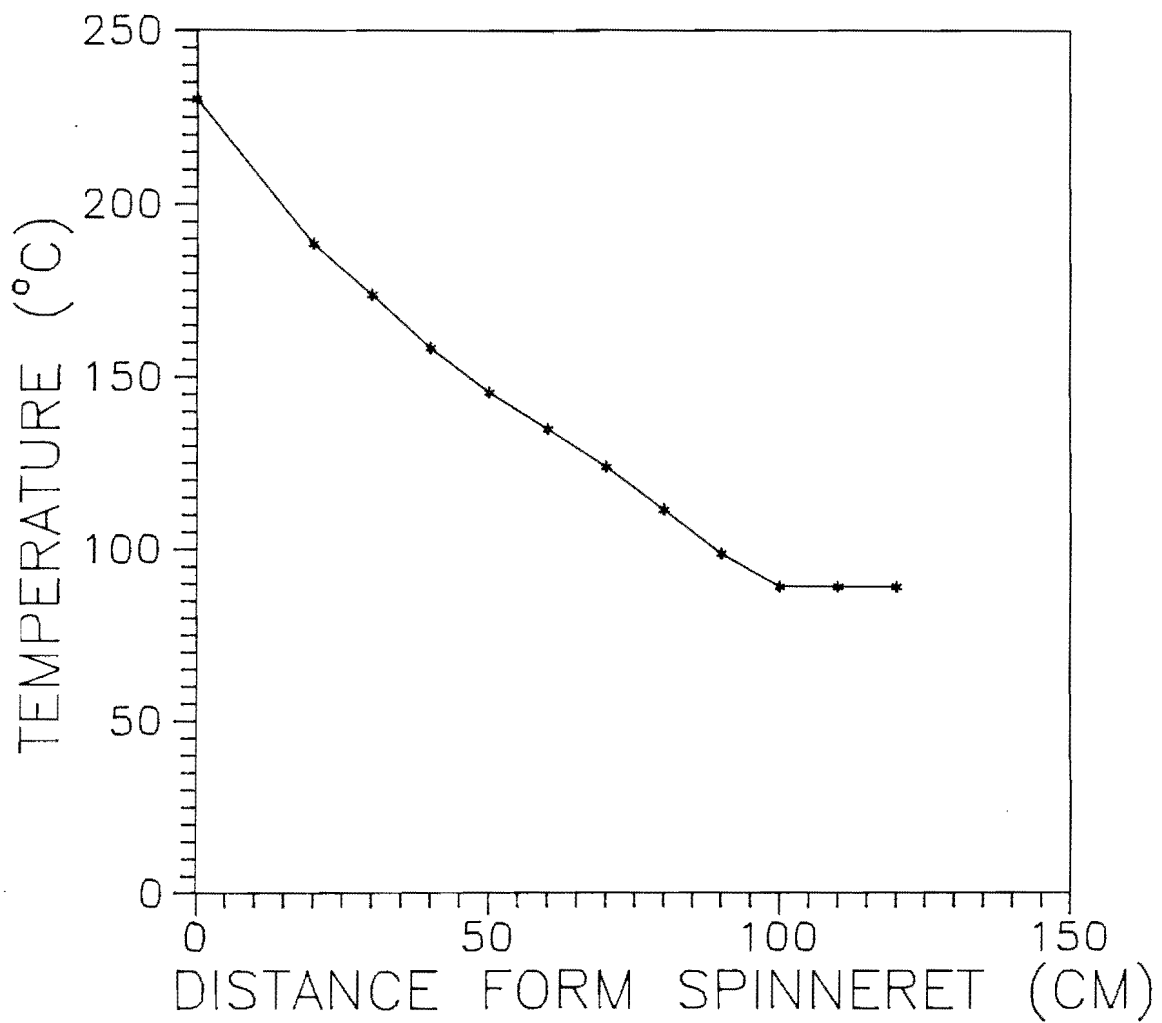


Figure 4-18 On-line measured temperature profile in the melt spinning process for LL1.

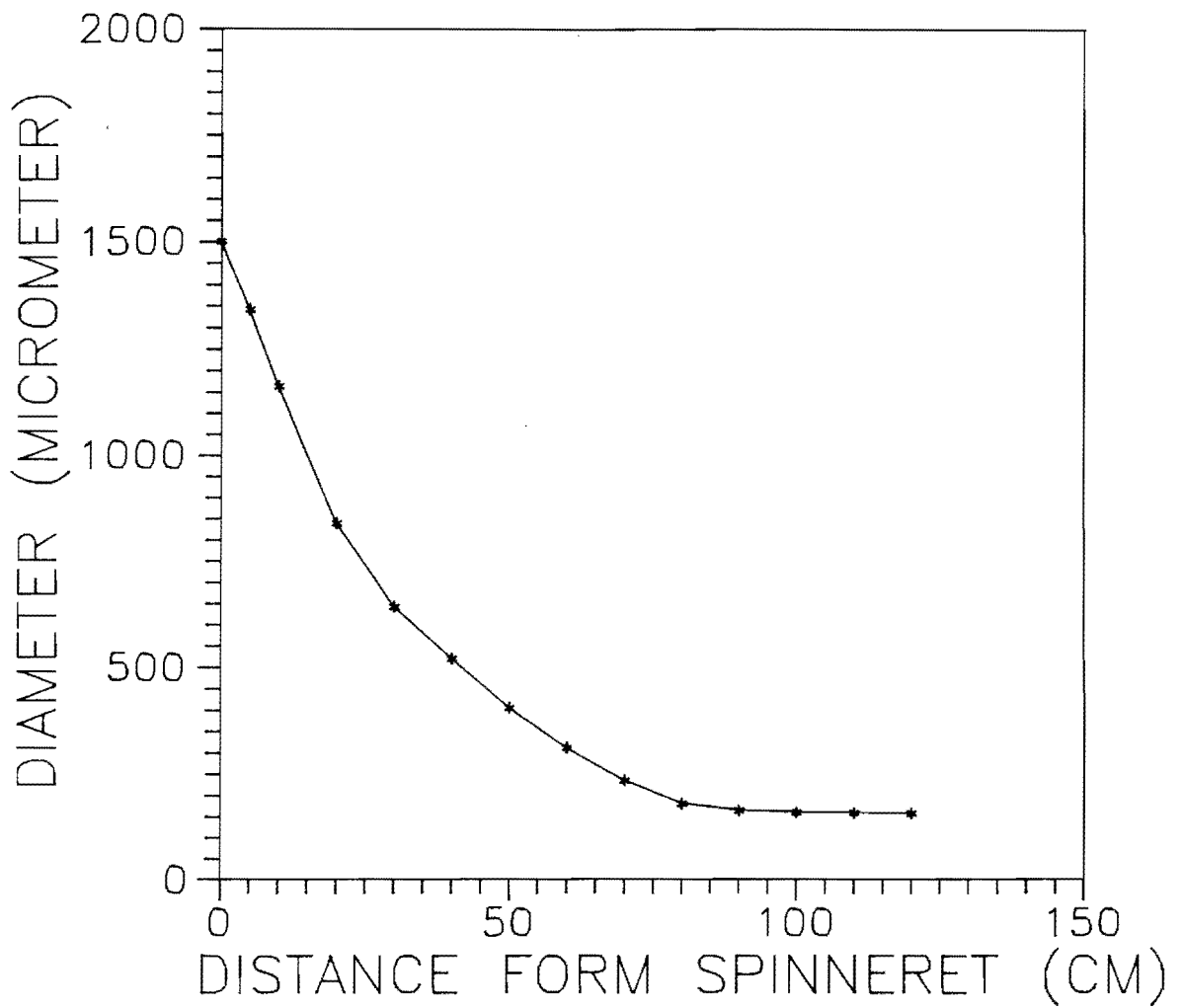


Figure 4-19 On-line measured diameter profile in the melt spinning process for LL1.

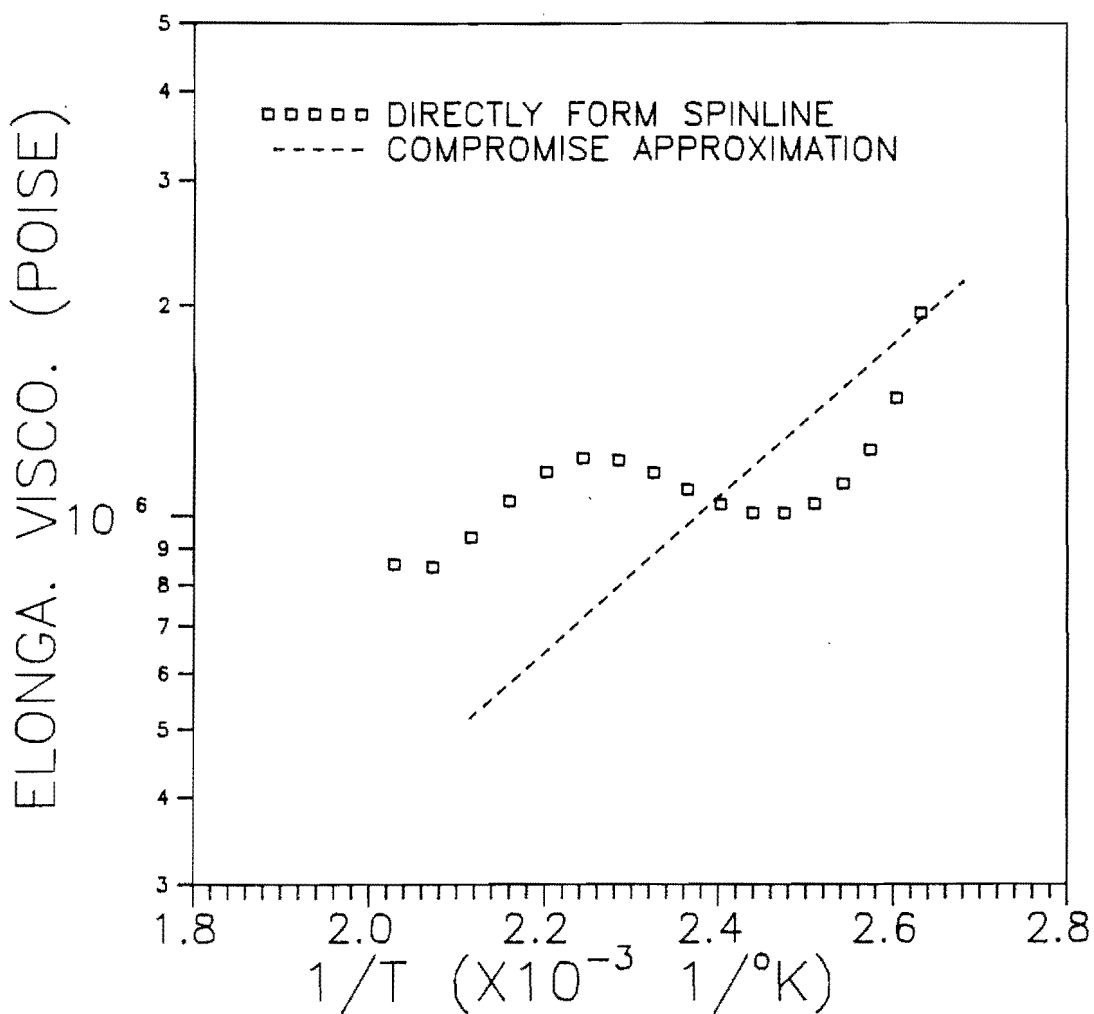


Figure 4-20 Apparent elongational viscosity calculated from the inversion procedure for LL1 in the melt spinning process.

### Heat Transfer Coefficient

Heat transfer coefficient in the region where crystallization does not occur can be calculated by the inversion procedure applied to our experimental temperature profile for the film blowing process. According to Equation(2-34), the energy balance equation without crystallization term is rewritten as

$$\rho C_p V H \frac{dT}{dZ} = - [ U(T-T_{air}) + \epsilon \sigma (T^4 - T_r^4) ] \quad (4-7)$$

where  $V(Z)$ ,  $H(Z)$ ,  $\epsilon(Z)$ ,  $T(Z)$ , and  $\frac{dT}{dZ}(Z)$  can be obtained from the experimental data, Figures 4-4, 4-5, 4-11 and 4-16, by best-curve fitting, and for polyethylene [112-114], we have

$$\rho_{melt} = [ 1.135 + 0.00104(T-273) ]^{-1} \quad (4-8)$$

$$C_p = 0.490 + 0.000867(T-273) \quad (4-9)$$

$$T_{air} = 49 \text{ } ^\circ\text{C} \quad ; \quad T_r = 30 \text{ } ^\circ\text{C} \quad (4-10)$$

Based on Equations(4-7) - (4-10), the apparent heat transfer coefficients with respect to the positions along the machine direction are computed by a BASIC program. From Figure 4-21, the apparent heat transfer coefficient approaches a constant value in the region close to the annular die. After  $Z=8$  cm,

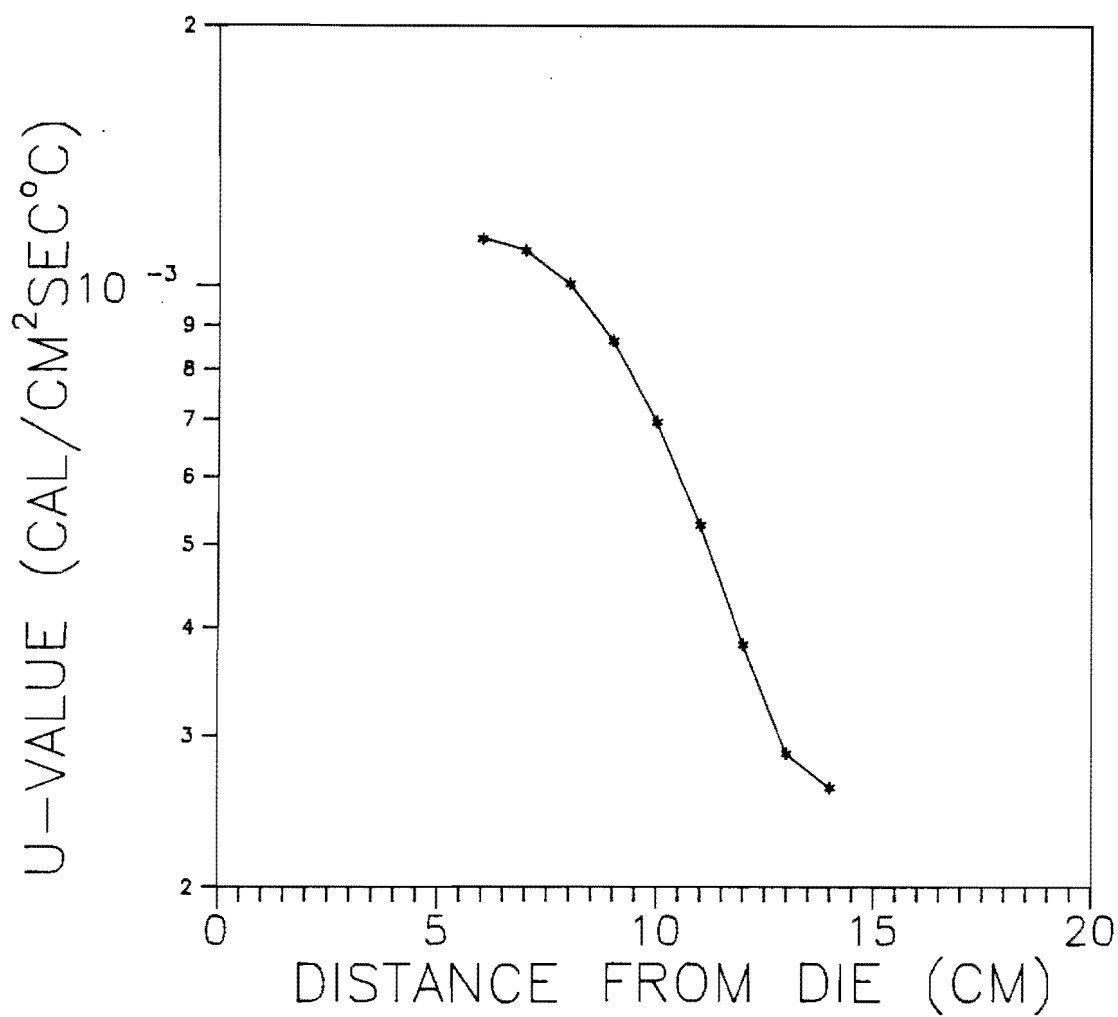


Figure 4-21 Apparent heat transfer coefficient calculated from the inversion procedure for the tubular film blowing process.

the local heat transfer coefficient is related to the 2.5 power of the distance above from the die. Thus the heat transfer coefficient can be expressed as the following empirical equations

$$z < 8 \text{ cm} \quad U = 1.2 \times 10^{-3} \text{ cal/cm}^2 \text{sec}^\circ\text{C} \quad (4-11a)$$

$$z > 8 \text{ cm} \quad U = \frac{0.275}{z^{2.5}} \text{ cal/cm}^2 \text{sec}^\circ\text{C} \quad (4-11b)$$

which are of the same forms suggested by Kanai and White [6,14].

#### 4.3 Mathematical Modelling for Tubular Film Blowing Process

According to the theoretical background in Chapter 2, Pearson and Petrie [3,4] established a mathematical description for the tubular film process under the assumption of an isothermal Newtonian fluid. Thereafter, Han and Park [5] developed the equations of Pearson et al. into a model for a non-isothermal power-law type fluid. However, Han et al. made an energy balance for the blown film process without considering the effects of crystallization of the material. In fact, for a semi-crystalline material the occurrence of crystallization would deeply affect the distribution of

temperature and the performance of rheological properties during processing. Hence, Kanai and White [6] added a crystallization factor into the rheological equation, and also included a term for crystallization energy in the heat balance equation.

Therefore, based on the above development, a non-isothermal crystallization rate equation will be added into the above model in this study, and it will interact with the calculation of the other equations in order to make the mathematical model more complete. Furthermore, in order to compare the mathematical prediction with the on-line measured results, most of the numerical values of physical parameters (e.g.,  $\epsilon$ ,  $C_p$ ,  $\eta$ ,  $U$ ,  $\Delta H_f, \dots$ , etc.) could be specified from the literature and experimental sources.

#### Continuity Equation

When the film blowing process is carried out under steady state conditions, and the incompressibility of the material is assumed, the mass balance equation is given by

$$W = 2\pi\rho RHV \quad (4-12)$$

where  $W$  is the mass throughput,  $R$  is the radius of the bubble,  $H$  is the thickness of the film,  $V$  is the film velocity in the machine direction, and  $\rho$  is the density of

material. It is noticed that all of the variables R, H and V are a function of position, Z, along the machine direction, and the density of the polyethylene film,  $\rho$ , is a function of temperature and crystallinity as shown the following expressions. In the molten state, the density [113,114] is

$$\rho_{am} = [ 1.135 + 0.00104 (T-273) ]^{-1} \quad (4-13a)$$

and the density in the solid state is [115]

$$\rho_{solid} = \left\{ \frac{1}{\rho_{am}} + X \left[ \frac{595-0.837(T-273)}{599-(T-273)} - \frac{1}{\rho_{am}} \right] \right\}^{-1} \quad (4-13b)$$

where the temperature T is in the unit of degrees Kelvin.

#### Force Balance

Under the assumptions that the surface tension of the bubble, the inertial force, the air drag force and the gravitational force are negligible compared to the rheological force, the force balance equation in the machine direction is given as

$$F_L = 2\pi R \sigma_{11} \cos\theta + \pi \Delta P ( R_L^2 - R^2 ) \quad (4-14)$$



where  $F_L$  is the take-up force measured at the take-up position,  $\theta$  is the angle between the tangent direction of the film and the machine direction,  $\Delta P$  is the pressure difference across the film,  $\sigma_{11}$  is the normal stress in "1" direction, and  $R_L$  is the final radius of the bubble. The force balance in the circumferential direction would be

$$\Delta P = \frac{H\sigma_{11}}{R_1} + \frac{H\sigma_{22}}{R_2} \quad (4-15)$$

where  $R_1$  and  $R_2$  are the principal radii of curvature of the film and given as

$$R_1 = \frac{-\sec^3\theta}{\frac{d^2R}{dz^2}} \quad (4-16a)$$

$$R_2 = \frac{R}{\cos\theta} \quad (4-16b)$$

In Equations(4-14) and (4-15), the normal stresses in the machine direction and circumferential direction can be expressed as

$$\sigma_{11} = \frac{-\eta Q \cos\theta}{\pi R H} \left( \frac{1}{R} \frac{dR}{dz} + \frac{2}{H} \frac{dH}{dz} \right) \quad (4-17)$$

$$\sigma_{22} = \frac{\eta Q \cos\theta}{\pi R H} \left( \frac{1}{R} \frac{dR}{dz} - \frac{1}{H} \frac{dH}{dz} \right) \quad (4-18)$$

where  $Q$  is the volumetric flow rate, thus

$$Q = 2\pi R H V \quad (4-19)$$

From the geometrical relationship, we have

$$\frac{dR}{dZ} = \tan\theta \quad (4-20a)$$

and

$$\frac{d^2R}{dZ^2} = \sec^2\theta \frac{d\theta}{dZ} \quad (4-20b)$$

With the aid of Equations (4-16), (4-17), (4-18) and (4-20), the force balance Equations (4-14) and (4-15) may be written as the following differential equations

$$\frac{dH}{dZ} = \frac{-H}{2R} \tan\theta - [A + BR^2] \frac{H \sec^2\theta}{4\eta} \quad (4-21)$$

$$\frac{d\theta}{dZ} = \frac{1}{R(A + BR^2)} \left[ \frac{A - 3BR^2}{2} + \frac{3\eta \sin\theta \cos\theta}{R} \right] \quad (4-22)$$

where

$$A = \frac{F_L - \pi R_L^2 \Delta P}{Q} \quad (4-23)$$

$$B = \frac{\pi \Delta P}{Q} \quad (4-24)$$

### Energy Balance

Assuming that both the heat conduction and heat generation due to the frictional force are negligible, the energy balance equation is given by

$$\rho C_p \left( \frac{Q \cos \theta}{2\pi R} \right) \frac{dT}{dZ} = -U(T - T_{air}) - \epsilon \sigma (T^4 - T_r^4) + \rho \Delta H_f \left( \frac{Q \cos \theta}{2\pi R} \right) \frac{dX}{dZ} \quad (4-25)$$

where  $C_p$  is the specific heat capacity, which is a function of temperature, expressed as Equation(4-9);  $\epsilon$  is the emissivity, which is a function of thickness, and approximate values of  $\epsilon$  are estimated by using Equation(4-4);  $\sigma$  is the Stefan-Boltzmann constant,  $1.355 \times 10^{-12}$  cal/sec $cm^2 \circ K^4$  [116];  $T_{air}$ , 49 °C, is the temperature of the cooling air;  $T_r$ , 30 °C, is the ambient temperature;  $X$  is the local crystallinity; and the heat of fusion,  $\Delta H_f$ , is assumed to be 66 cal/g [117]. Assuming the Avrami index  $n=1$ , the crystallinity change with respect to position  $Z$  is given as

$$\frac{dX}{dZ} = \frac{X_f K}{v} \left( 1 - \frac{X}{X_f} \right) \quad (4-26)$$

The details about the above equation will be discussed latter. Hence with the aid of Equation(4-26), the energy balance equation, Equation(4-25), can also be written as a differential equation

$$\frac{dT}{dZ} = -CR\sec\theta(T-T_{air}) - DR\sec\theta(T^4-T_r^4) + FX_fKRH\sec\theta\left(1-\frac{X}{X_f}\right) \quad (4-27)$$

where

$$C = \frac{2\pi U}{\rho C_p Q} \quad (4-28)$$

$$D = \frac{2\pi\sigma\epsilon}{\rho C_p Q} \quad (4-29)$$

$$F = \frac{2\pi\Delta H_f}{C_p Q} \quad (4-30)$$

### Viscosity Equation

In addition to the Arrhenius temperature dependence, the elongational viscosity is also a function of crystallinity. An empirical factor was used by Kikutani [118] to modify the viscosity equation to account for the development of crystallinity. A similar approach was also used successfully

by Lambach [103] and Hood [109] in the simulation of the melt spinning process for polyethylene resin.

In Equations(4-17) and (4-18), one needs the general viscosity  $\eta$ . The elongational or shear viscosity appropriate to the particular deformation will come automatically out of the mathematical analysis. Thus, we obtain the general viscosity by dividing Equation(4-6) by three in accord with the Trouton viscosity equation [119] and by adding a crystallinity factor; this equation is given by

$$\eta = a \exp\left(\frac{b}{T}\right) \exp\left[\alpha\left(\frac{X}{X_f}\right)^\beta\right] \quad (4-31)$$

where a and b are 830 and 2523, respectively. Based on the melt spinning simulation carried out by Lambach [103] and Hood [109], values of  $\alpha$  and  $\beta$  are chosen to be 13.5 and 0.5, respectively. Moreover, the final weight-fraction crystallinity  $X_f$  in Equation(4-31) can be obtained from density by the following equation

$$X_f = \left(\frac{\rho - \rho_a}{\rho_c - \rho_a}\right) \left(\frac{\rho_c}{\rho}\right) \quad (4-32)$$

where  $\rho_a$  and  $\rho_c$  are the theoretical densities of amorphous and crystalline phases, respectively. At 23 °C,  $\rho_a=0.863$  and

$\rho_c=1.000$  are taken for polyethylene [115]. Finally the value for  $X_f$  is 0.5621.

### Crystallization Kinetics

From the analysis of non-isothermal crystallization, Nakamura [70-72] proposed a modified Avrami equation

$$\frac{X(t)}{X_f} = 1 - \exp \left\{ - \left[ \int_0^t K(T) dt \right]^n \right\} \quad (4-33)$$

where  $X(t)$  is the degree of phase transformation at time  $t$ ,  $X_f$  is the ultimate degree of phase transformation at  $t \rightarrow \infty$ , and  $K$  is the crystallization rate constant. Differentiating the above equation with respect to time, one obtains the crystallization rate equation

$$\frac{\partial X}{\partial t} = X_f n K \left( \int_0^t K dt \right)^{n-1} \exp \left[ - \left( \int_0^t K dt \right)^n \right] \quad (4-34)$$

In order to evaluate the crystallinity change along the machine direction, one converts the time derivative to a position derivative through the relationship,  $(\partial/\partial t)=V(d/dZ)$ , and obtains

$$\frac{dX}{dZ} = \frac{X_f n K}{V} \left( \int_0^Z \frac{K}{V} dZ \right)^{n-1} \exp \left[ - \left( \int_0^Z \frac{K}{V} dZ \right)^n \right] \quad (4-35)$$

In the melt spinning process, Ziemiński and Spruiell [120] found that different values of the Avrami index  $n$  had relatively little effect on the overall progress of crystallization in the calculation. Hence  $n=1$  is assumed, and Equation(4-35) is simplified to the following compact form

$$\frac{dX}{dZ} = \frac{X_f K}{V} \left( 1 - \frac{X}{X_f} \right) \quad (4-36)$$

The temperature and orientation dependence of the rate constant,  $K$ , was proposed by Ziabicki [77]

$$K = K_{\max} \exp \left[ -4 \ln 2 \left( \frac{T - T_{\max}}{D} \right)^2 + A(T) f^2 \right] \quad (4-37)$$

However, this equation is merely an empirical expression. Katayama and Yoon [81] and Zhou [82], based on the assumption, that the rate of crystallization has the same form of temperature dependence as that of the growth rate, obtained a crystallization rate equation with the presence of molecular orientation

$$K(T, f_a) = K_0 \exp \left[ \frac{-U^*}{R(T - T_{\infty})} \right] \exp \left[ \frac{-C_3}{T \Delta T + C_0 T^2 f_a^2} \right] \quad (4-38)$$

where  $U^* \approx 1500$  cal/mol, is the activation energy for segmental jump rate in polymers,  $T_\infty = T_g - 30$  K,  $\Delta T = T - T_m^0$ ,  $K_0$  and  $C_3$  are constants obtained from isothermal analysis,  $f_a$  is the amorphous orientation factor, and the constant  $C_0$  is an adjustable parameter to determine the magnitude of the effect of molecular orientation in the melt. Equation(4-38), the non-isothermal stress-induced crystallization rate equation, was successfully applied to the simulation of melt spinning for polypropylene [82].

Comparing the measured stresses for LLDPE in melt spinning and film blowing process [14,103], it is found that the stress acting on the melt during spinning is much higher (about 50 times) than that in the blowing process. Hence, we decided to omit the orientation term in Equation(4-38).

The values for  $K_0$  and  $C_3$  were estimated from the Hood's study [109] for quiescent crystallization of LLDPEs. The values of  $K_0 = 2.9656 \times 10^5$  sec<sup>-1</sup> and  $C_3 = 1.31 \times 10^5$  K<sup>2</sup> for LL4 in his study were chosen because the resin LL4 (LLDPE with MI=4.0 and  $\rho = 0.935$  g/cm<sup>3</sup>) has an identical density value with that of LL1 used in this study. The above two coefficients were obtained from the data of non-isothermal crystallization carried out by DSC (Differential Scanning Calorimetry). The equilibrium melting point  $T_m^0$  for linear polyethylene is  $141 \pm 0.5$  °C, which was determined by Illers and Hendus [121].



## Numerical Procedures

For simulating the non-isothermal film blowing process with the occurrence of crystallization, this system is governed by the five first-order differential equations, Equations (4-20) - (4-22), (4-27) and (4-36). These five differential equations were integrated by using the fourth-order Runge-Kutta method, which had the advantages of self-starting and providing good accuracy [122]. Numerical integration of the system equations was carried out with the following initial conditions (at  $Z=0$ ):

$$R=R_0 \ ; \ H=H_0 \ ; \ T=T_0 \ ; \ \theta=0 \ ; \ X=0$$

The take-up force  $F_L$  and the internal pressure differential  $\Delta P$  were used as arbitrary input parameters to control the development of the solution. The calculation was stopped when  $R$  reaches the final radius  $R_L$  and  $\theta=0$ . A BASIC computer program, which was successfully used for simulating the melt spinning process [111], was modified to be suitable for the tubular film blowing system.

## Comparison of Mathematical Prediction and On-line Measurements

The integrations of the five system equations were carried out simultaneously based on our best estimates of the material parameters, which were described in the above several paragraphs. Variations in these parameters and the processing variable were also considered. Comparisons of one set of calculated results and the on-line measured data for radius, thickness, temperature and velocity are shown as from Figures 4-22 through 4-25, respectively; and the theoretically predicted on-line crystallinity is also shown in Figure 4-26. The qualitative shapes of the predicted curves are somewhat similar to those of the experimentally measured profiles. As was mentioned above, in this study one of the most distinct features, which distinguish it from the others, is the intention to improve this mathematical model by considering the effects of crystallization during processing. That is, a non-isothermal crystallization rate equation was added into the model in order to make it more complete and suitable for describing the cases of blowing semi-crystalline materials. Thus, the predicted temperature curve, the dashed line in Figure 4-24, exhibits an obvious temperature plateau, which is a common feature in most of the measured temperature profiles for blowing semi-crystalline resins [13,14,17].

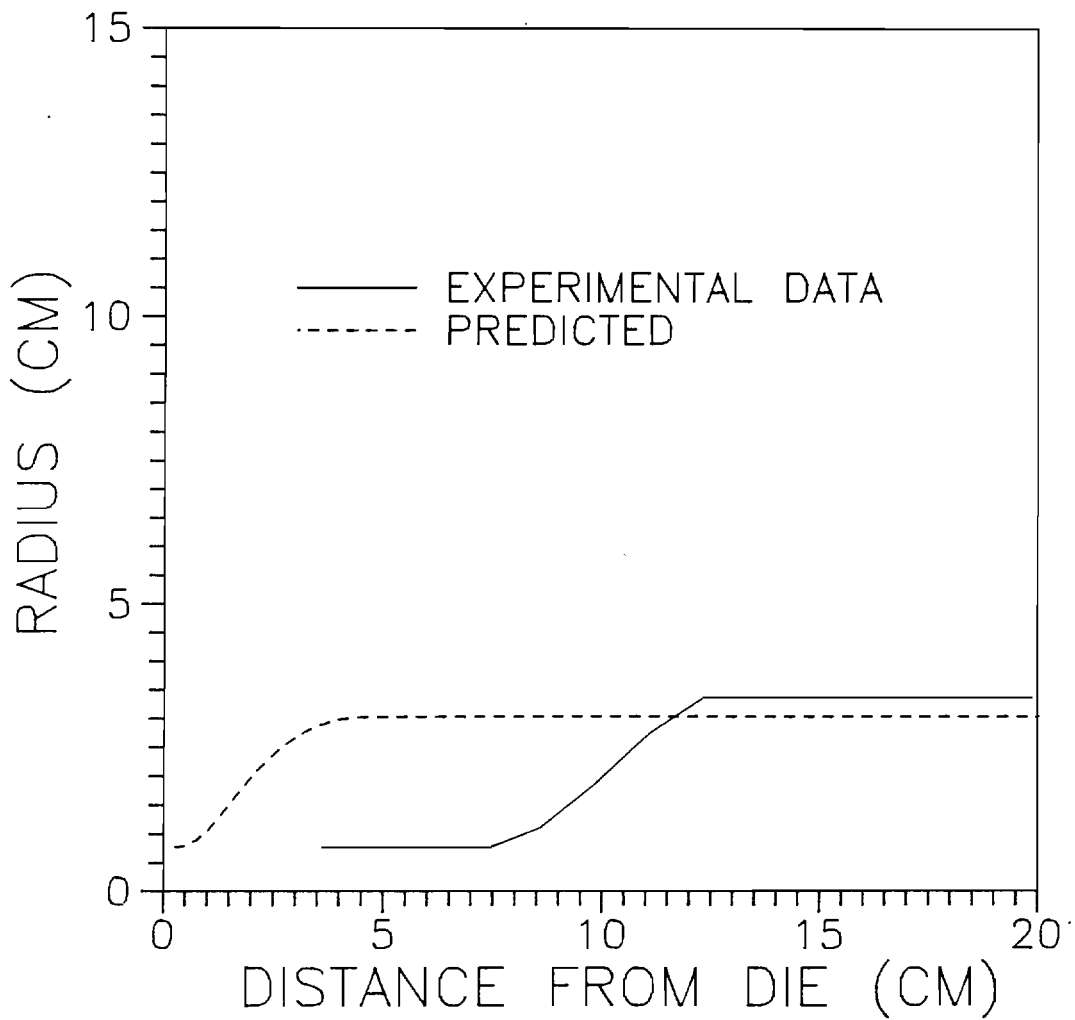


Figure 4-22 Comparison of the predicted and experimental radius profiles.

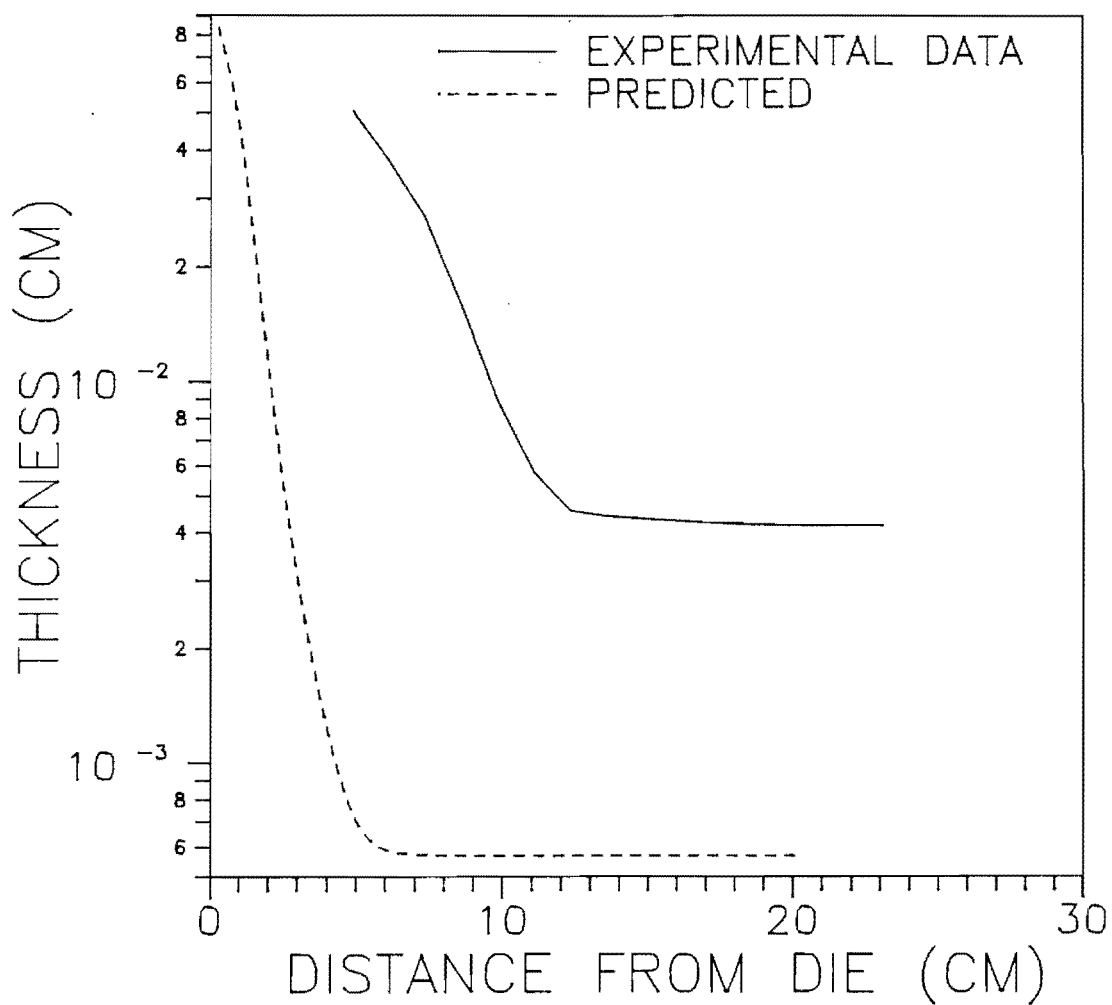


Figure 4-23 Comparison of the predicted and experimental thickness profiles.

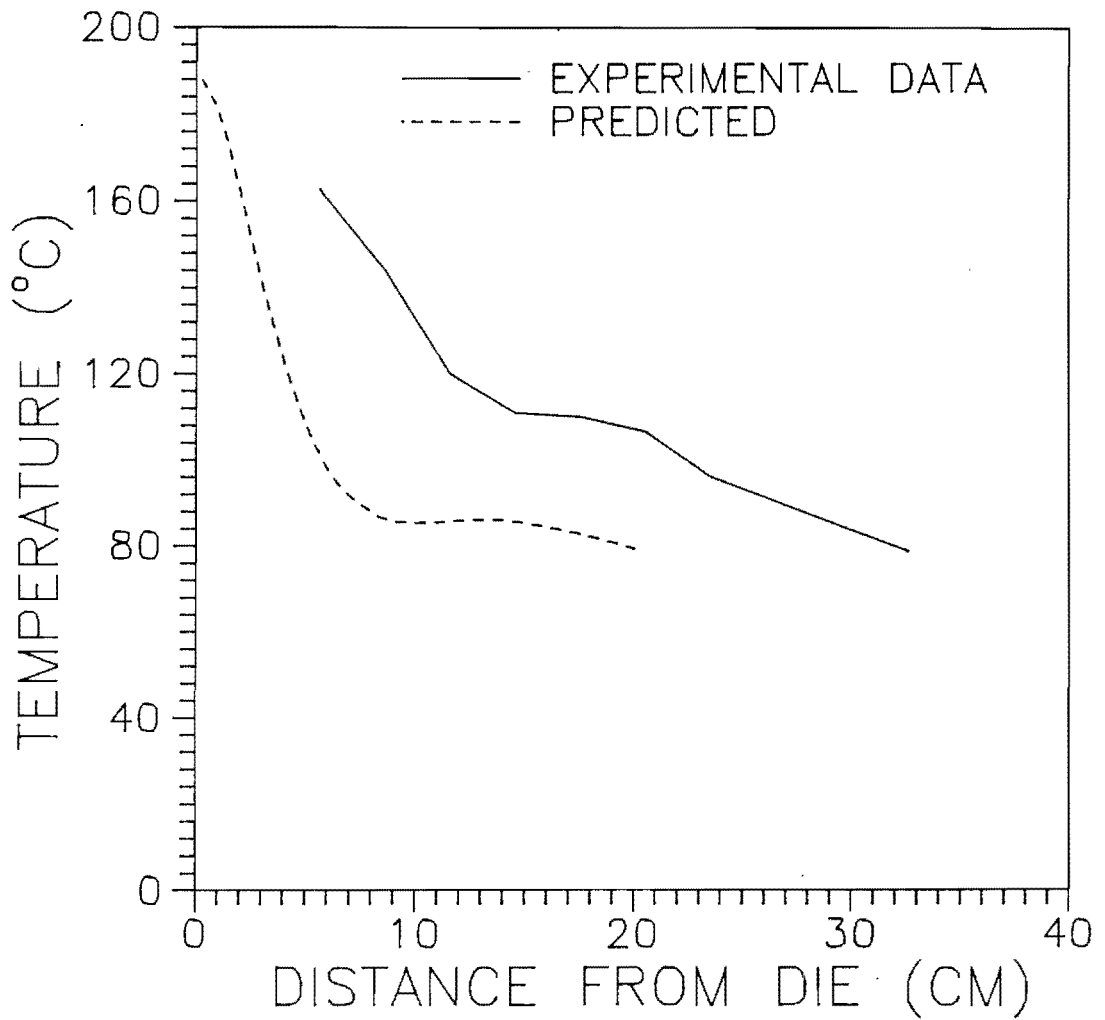


Figure 4-24 Comparison of the predicted and experimental temperature profiles.

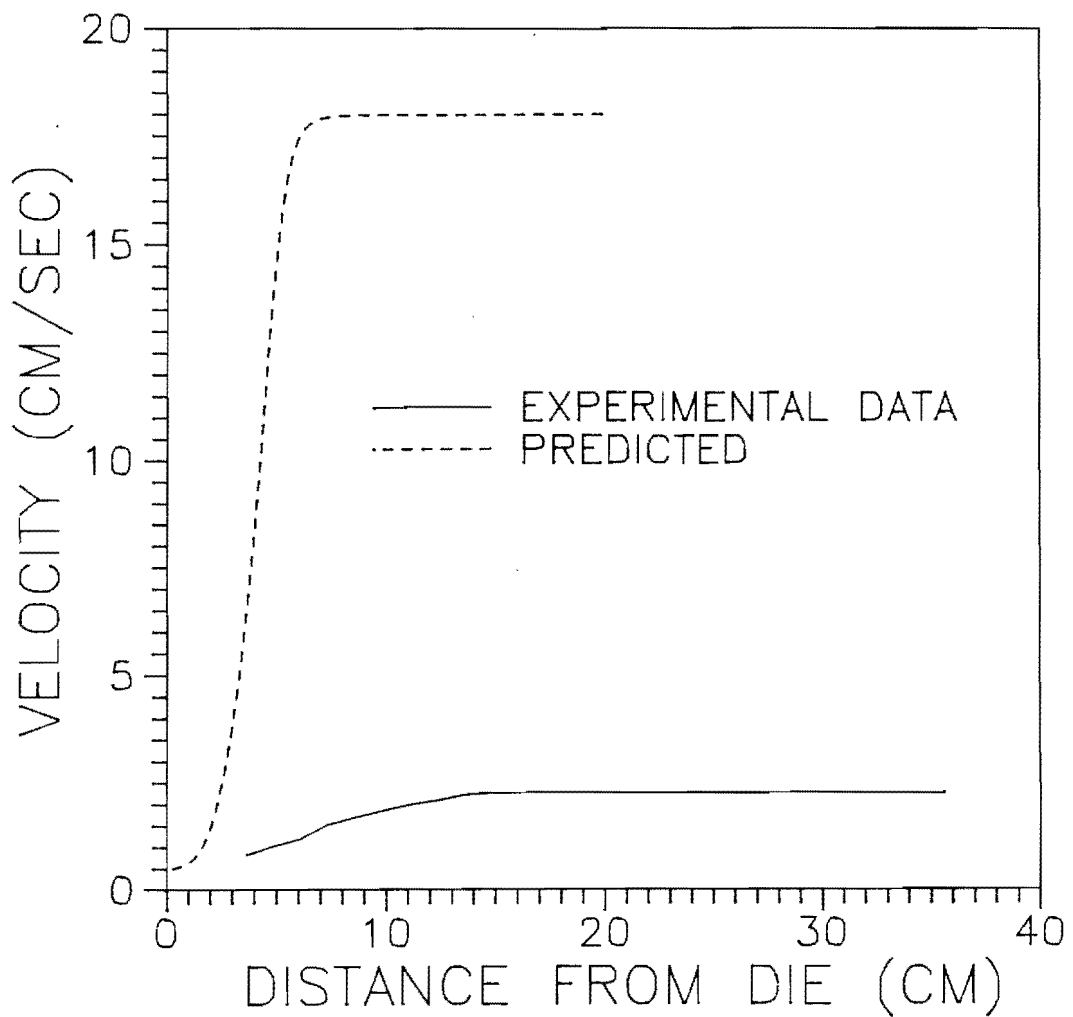


Figure 4-25 Comparison of the predicted and experimental velocity profiles.

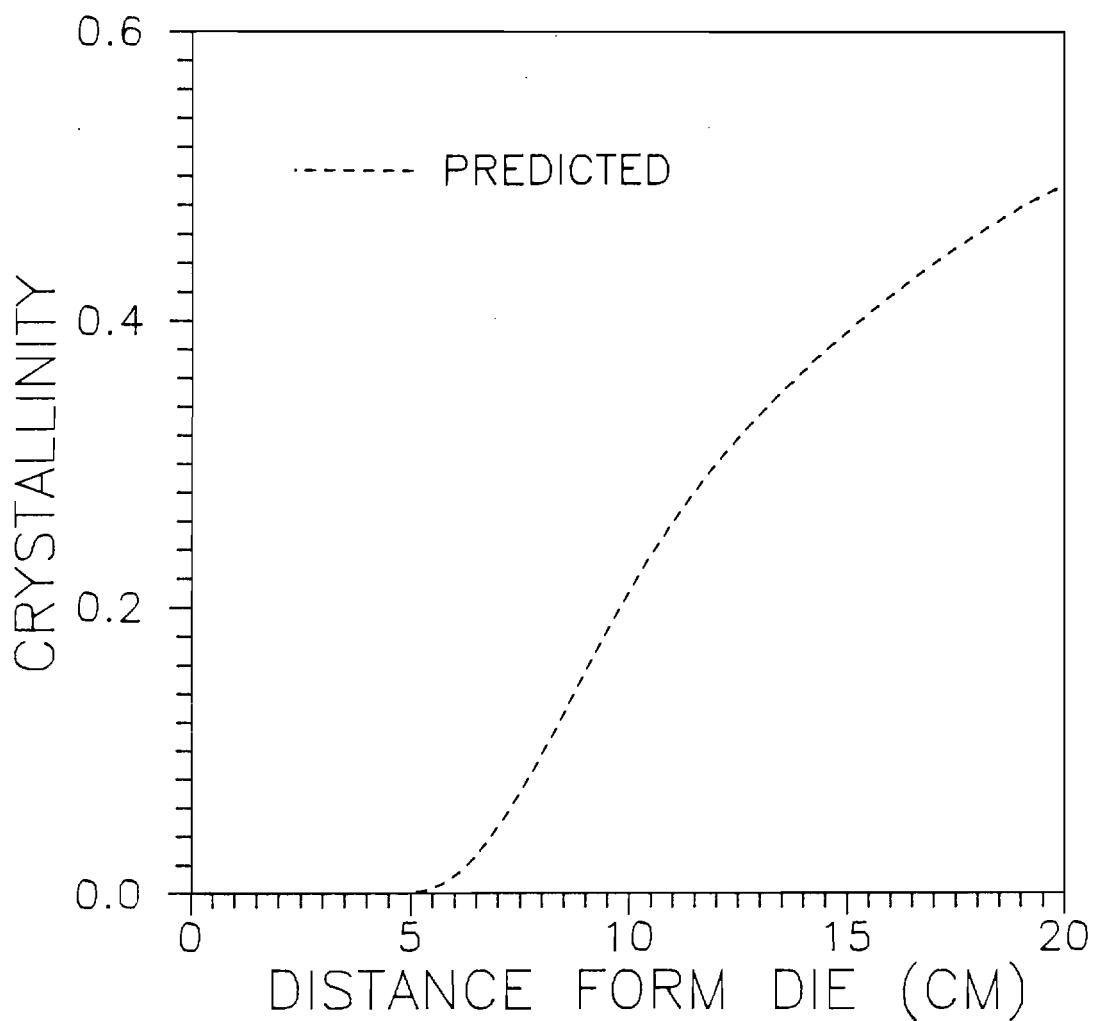


Figure 4-26 Theoretically predicted on-line crystallinity profile.

However, there is, unfortunately, a large quantitative difference between the theoretical and experimental curves. For example, although two force parameters,  $F_L$  and  $\Delta P$ , are adjusted to make the calculated final radius approach to the experimental value, a big difference still exists between the ways the radii change from  $R_0$  to  $R_L$ . From Figure 4-22, the mathematical model predicts that the radius of the tubular film starts to increase at about 1 cm above the die exit. On the other hand, the on-line measured radius profile shows that the position at which the bubble begins to be inflated is around  $Z=7.5$  cm under the identical processing parameters.

Moreover, examining all the primary differential equations, Equations(4-20) - (4-22), (4-27) and (4-36), the five system variables,  $R$ ,  $H$ ,  $T$ ,  $\theta$  and  $X$ , interact with each other. Thus, owing to the poor agreement between two radius curves in Figure 4-22, a successful prediction for the other on-line quantities, thickness, temperature and velocity become impossible as shown in Figures 4-23 through 4-25.

#### Behavior of the Mathematical Model for Various Choices of the Parameters

From the above section, the agreement between the experimental data and the calculated results is very poor. One of the most obvious differences between the calculated and experimental results is in the "neck" region, which is



from the die exit to the position where the radius starts to increase. Examining the predicted radius profile, the length of the "neck" region is very short, i.e., the position where the bubble begins to be inflated is very close to the die exit ( $Z=0$ ). Although the inflating position can be controlled by adjusting the processing conditions, for many cases the length of the "neck" region is about 6-9 cm in the literature [8,14,17] and 7.5 cm in this study.

We decided to examine the sensitivity of this aspect of the model to changes in both processing and material parameters. Although the changes were chosen somewhat arbitrarily, they provided insight into the effects of changing each of the inputs. Some changes resulted in an unstable calculation and these were discarded. The figures shown below illustrate the tendencies found for stable calculations. Here, only the radius profiles for different values of parameters are shown, because the bubble shape is a more intuitively understandable quantity than the others. The other parameters were computed and could be displayed if they were needed.

The key processing parameters,  $F_L$ ,  $\Delta P$  and  $T_0$ , and the material parameter  $\eta$ , were adjusted, and some of the representative results are shown in Figures 4-27 through 4-31. These figures show that changes in these parameters do not provide any rationale for a tubular film with a long

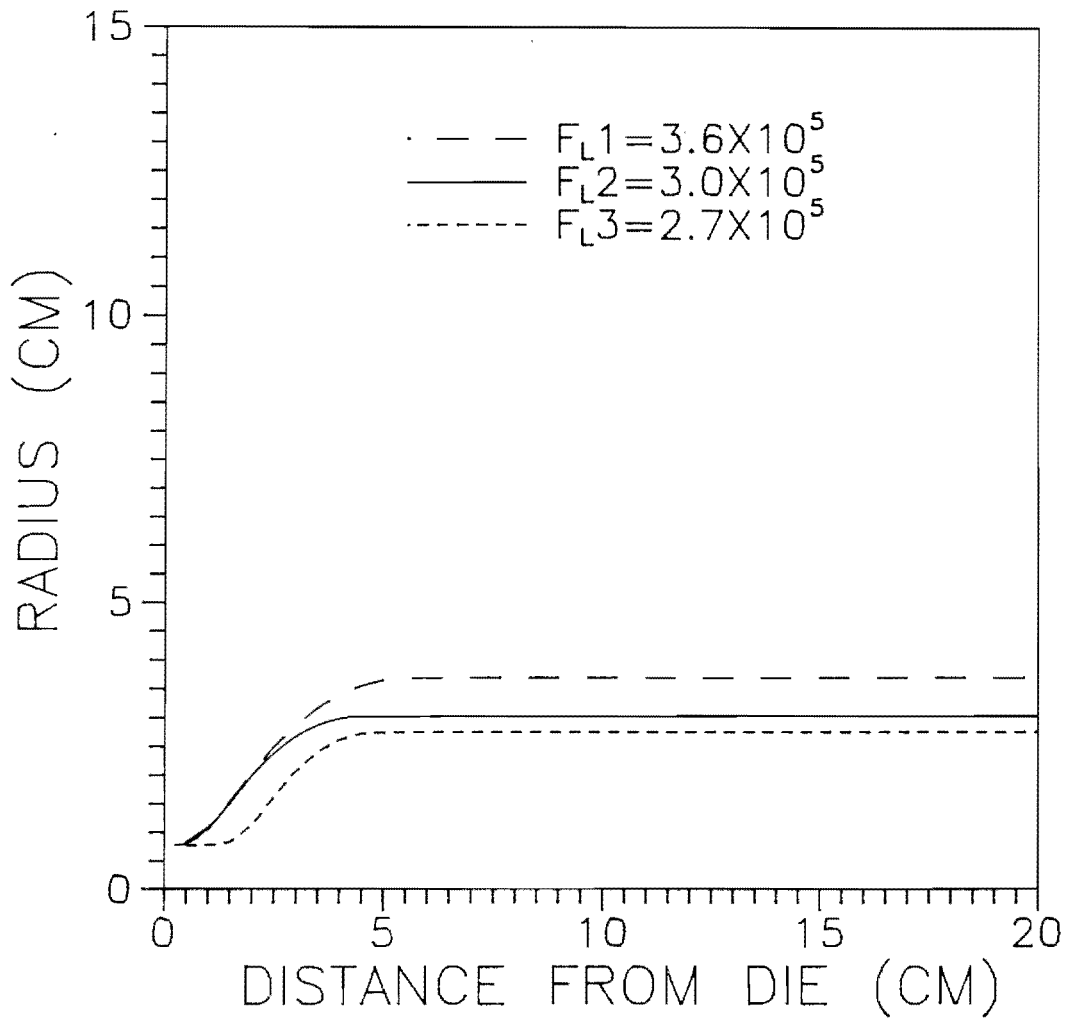


Figure 4-27 Comparison of the predicted radius profiles for different  $F_L$  values.

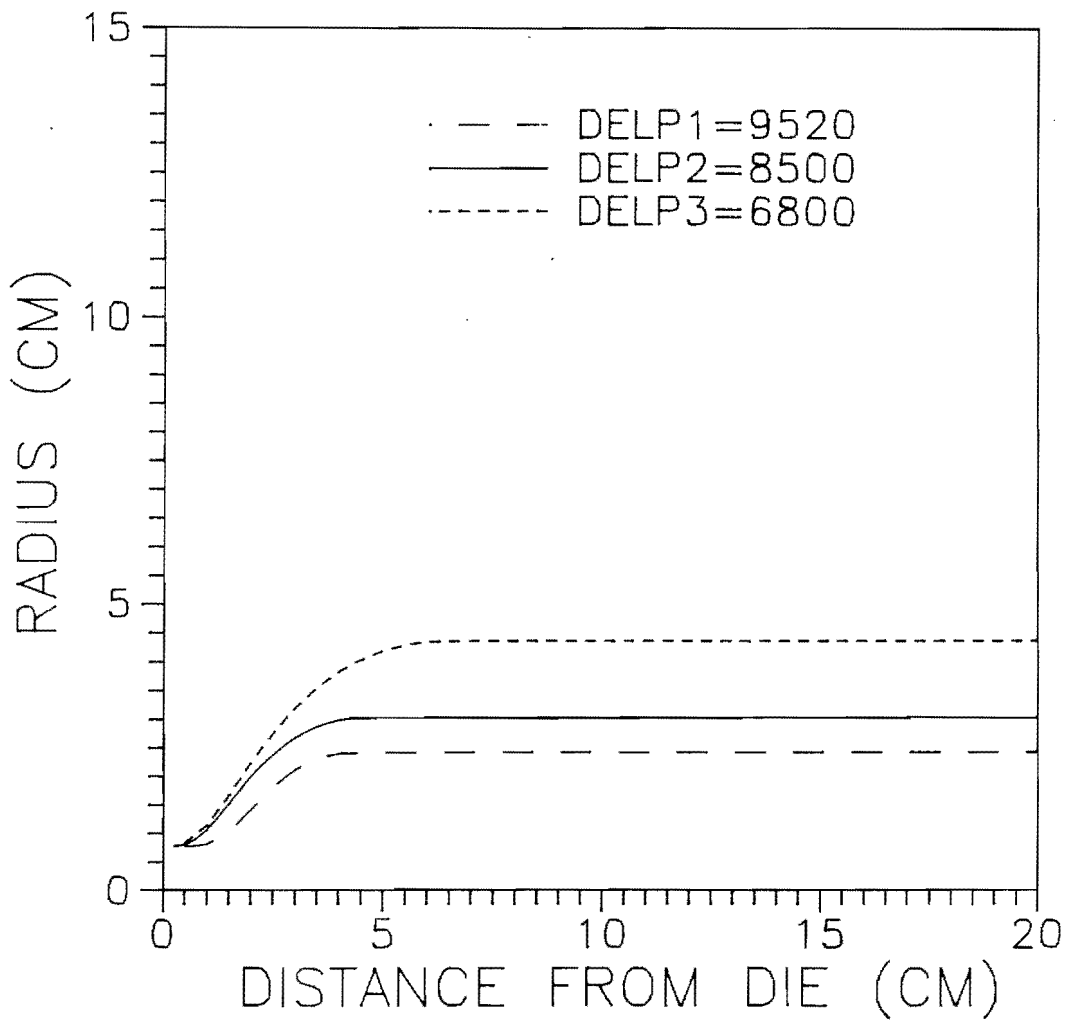


Figure 4-28 Comparison of the predicted radius profiles for different  $\Delta P$  values.

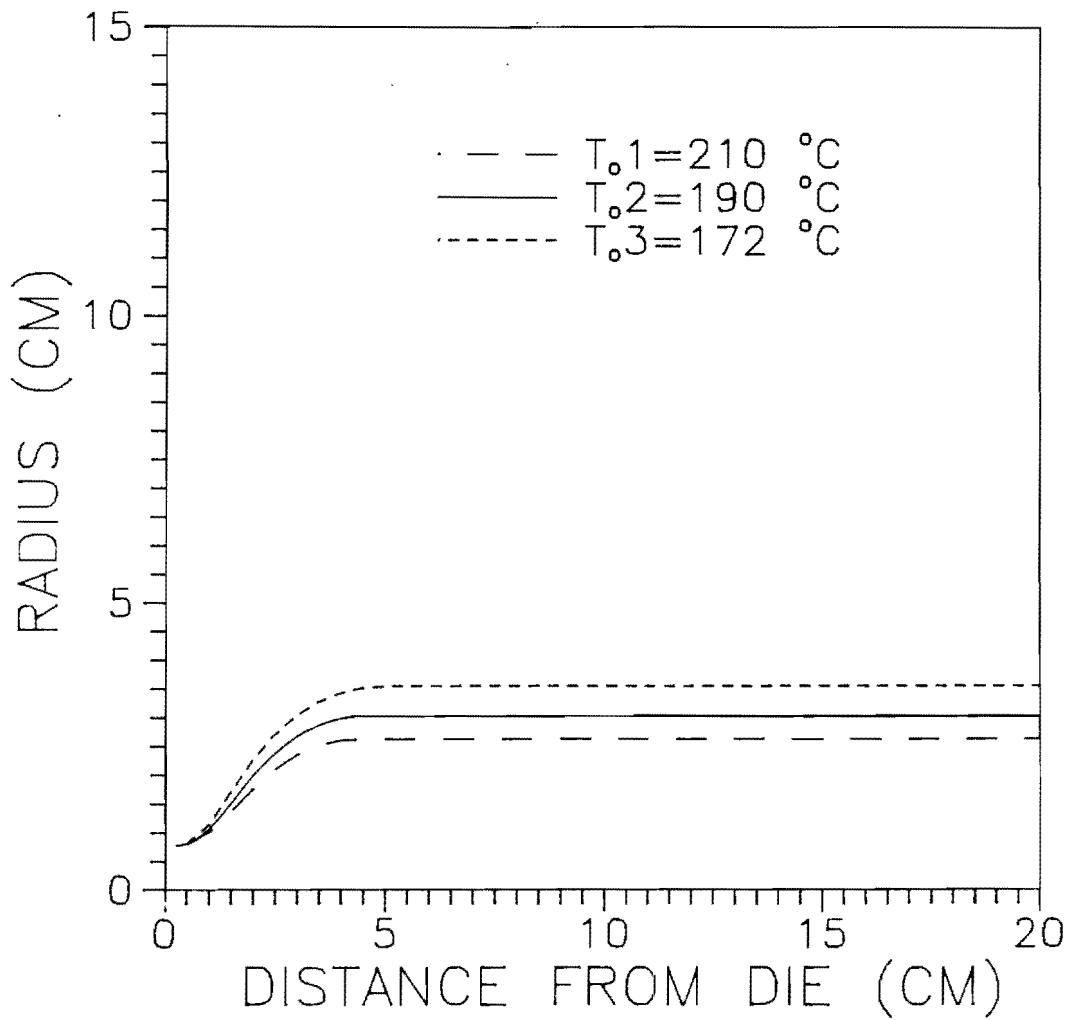


Figure 4-29 Comparison of the predicted radius profiles for different  $T_o$  values.

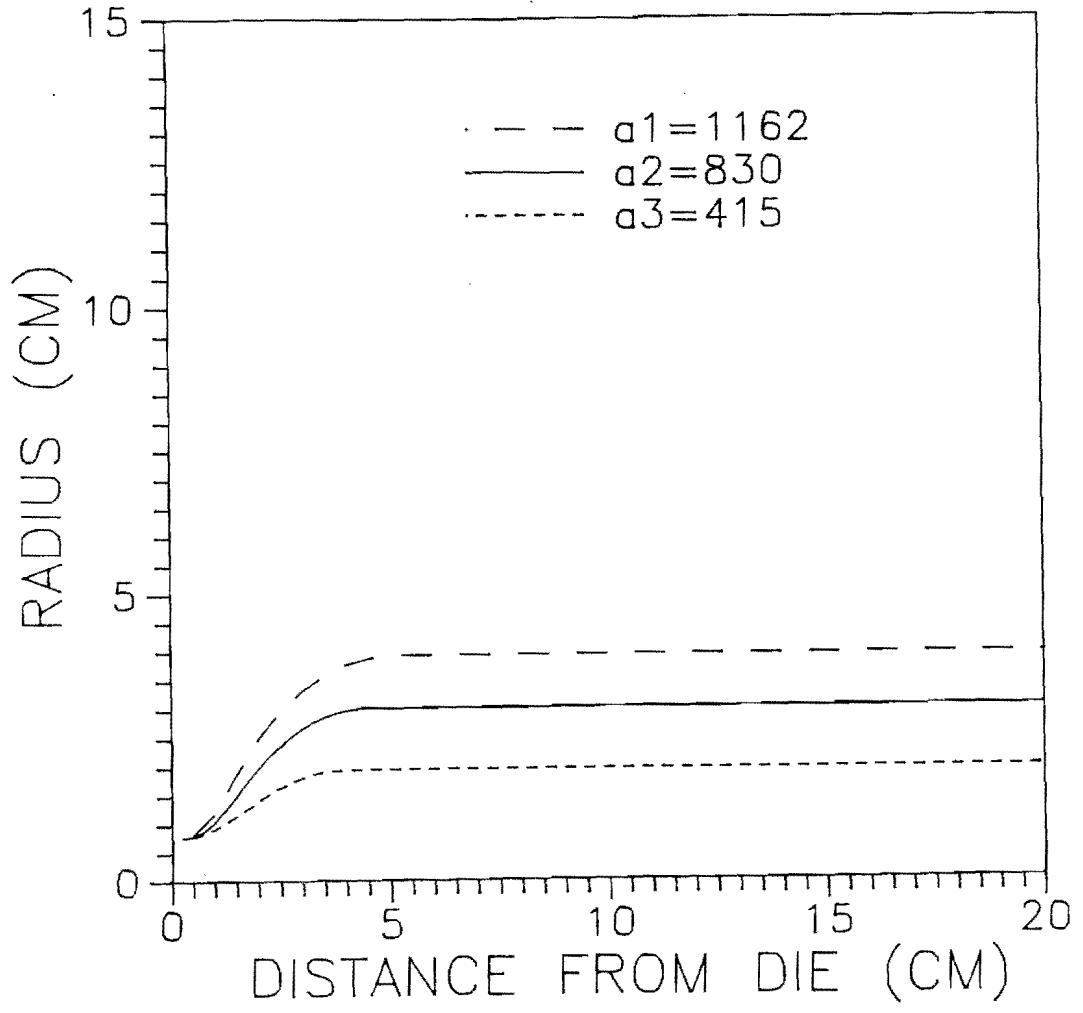


Figure 4-30 Comparison of the predicted radius profiles for different  $a$  values.

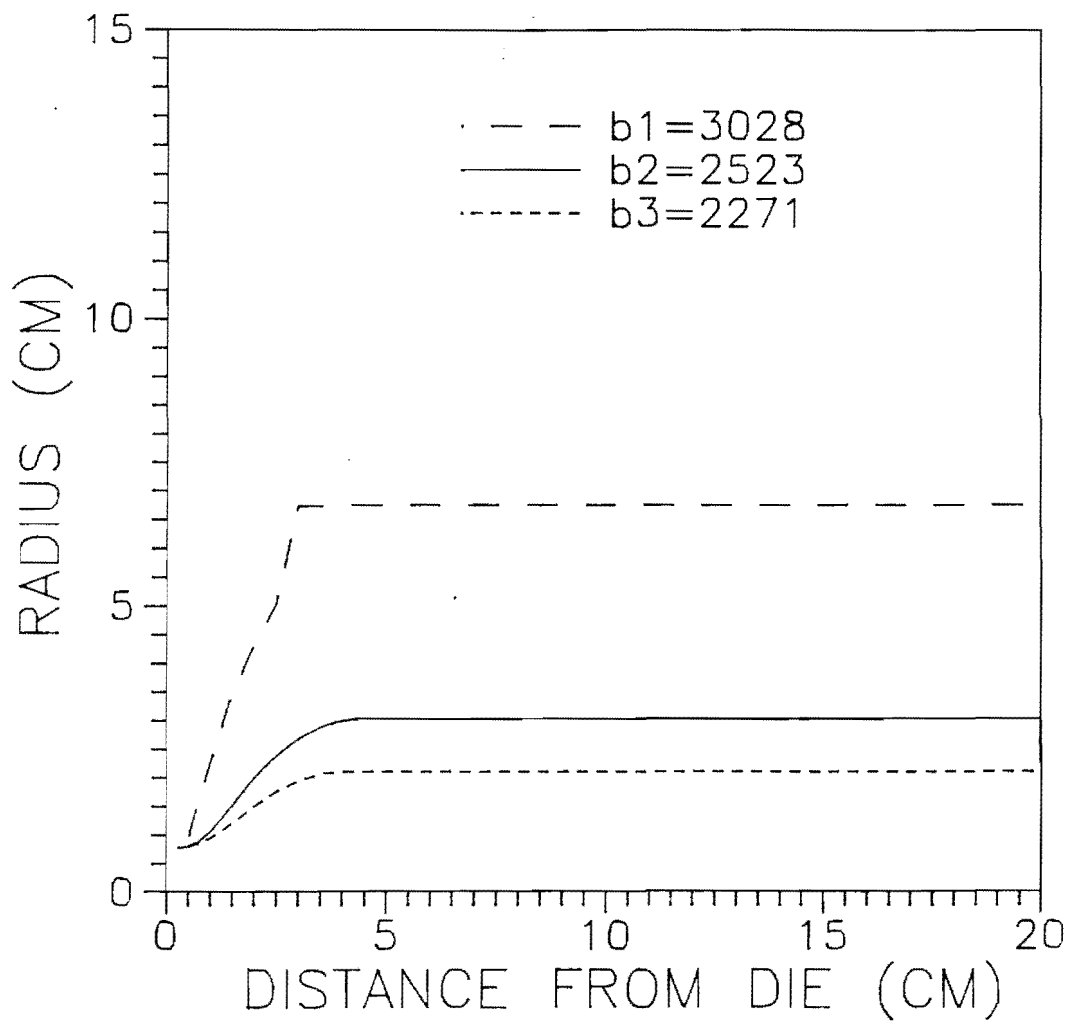


Figure 4-31 Comparison of the predicted radius profiles for different  $b$  values.

"neck". Furthermore, the other parameters, such as  $U$ ,  $Q$ ,  $H_0$ , ..., etc., which were varied also gave no help in resolving this discrepancy. Moreover, careful review of the predicted radius profiles in the literature [5,6,21], the length of the "neck" region of all those results also appeared to be not long enough to have a good agreement with the most of the practical bubble shapes for various polyethylene films [8,14,17]. Han and Park [5] also found that a discrepancy exists between the theoretically predicted and experimentally observed profiles.

A close look at Figure 4-27 through Figure 4-31 not only shows evident disagreement with the experimental profiles, but also exhibits behavior beyond our intuitive expectation. The most obvious case is that the radius decreases with the increase of  $\Delta P$ , shown as Figure 4-28. This kind of tendency was also found in the other studies [5,6,20]. This phenomenon was previously interpreted as due to the effects of the surface tension forces between the inflated bubble and the air, i.e., a larger  $\Delta P$  is required for a bubble with smaller radius ( $\Delta P = \text{surface tension} / \text{radius of a bubble}$ ) [5,20]. However, this explanation seems not satisfying enough, because the surface tension term was not considered when the force balance equations were established.

The experimental observations on the relationship between  $\Delta P$  and blow-up ratio are mixed. Kanai and White

[6,14] found that an inverse pressure effect both in their experimental data and theoretical analysis. However they [6,14] did not give a physical interpretation. Han and Park [11] found both situation (i.e., radius increasing and decreasing with the inside pressure); whereas Wagner [123] found the "intuitive" effect for most of his data (that is, small increases in the pressure caused large increases in the radius). There was not any analysis, however, in either of these studies. According to Wagner's results, a significant intuitive effect was shown in the cases of low blow-up ratio; however, a nearly constant pressure appeared in the cases of blow-up ratio greater than about two.

In the present work, a few observations for the relationship between  $\Delta P$  and blow-up ratio were made, as shown in Figure 4-32, in which the magnitude of the measured inside pressure is similar to that of Wagner [123]. Figure 4-32 shows that there is a significant fluctuation of the measured inside pressure and the radius is very sensitive to inside pressure difference. Nevertheless, Figure 4-32 appears to show the intuitive effect. Therefore, based on the above discussion, the mathematical model described in the previous sections appears to have some incapability. It seems important to theoretically reconsider the tubular film blowing process.



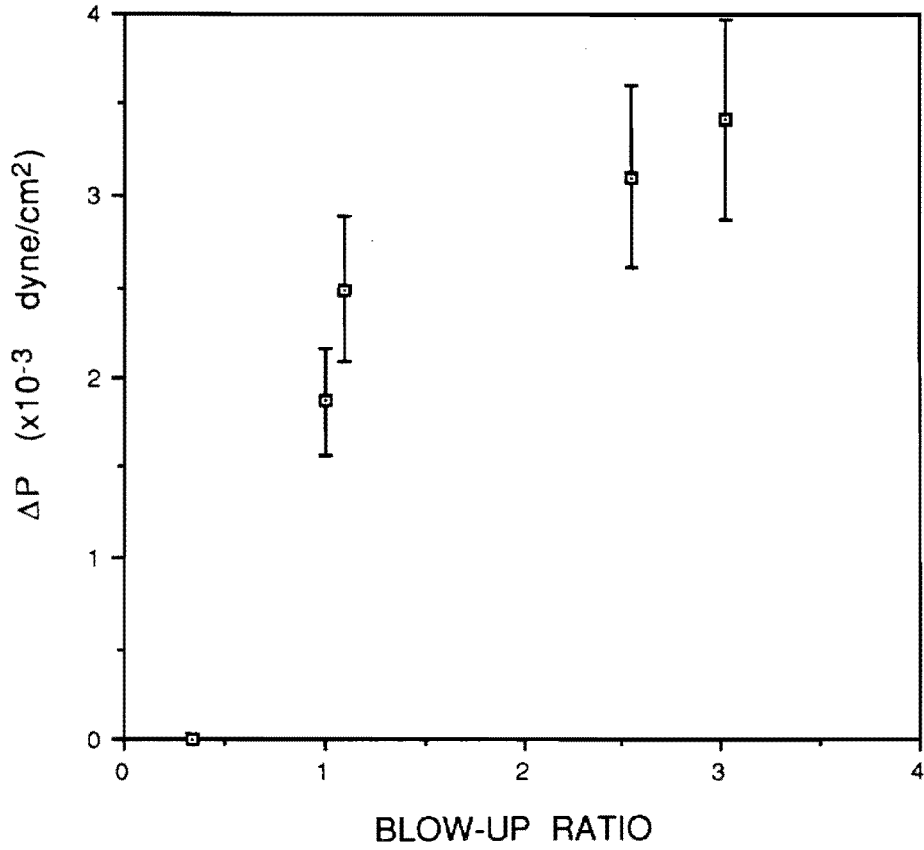


Figure 4-32 Experimentally observed relationship of  $\Delta P$  and blow-up ratio.

#### 4.4 Proposed Equations for the Simulation of Tubular Film Blowing Process

##### A Modified Approach to Describe Film Blowing Process

###### (1) Force Balance

The force balance equations in the original model were made between two certain points along the machine direction under the condition of the whole system reaching a steady state. Now, a consideration from another point of view will be made.

When the polymeric melt emerges from the exit of an annular die with a constant flow rate, its shape seems to be a small, short "tube" with constant radius. As the process is being carried out, this short "tube" is being acted on by two principal forces in different directions: one is a net force  $F$  in the machine direction; the other one is a pressure difference  $\Delta P$  across the wall of this "tube". In other words, the whole tubular film in processing is considered as being composed of many infinitesimal tubular elements, which are schematically shown as Figure 4-33. Thus, considering a tubular element with unit length, we have the following force balance equations

$$F = 2\pi R H \sigma_{11} \quad (4-39)$$

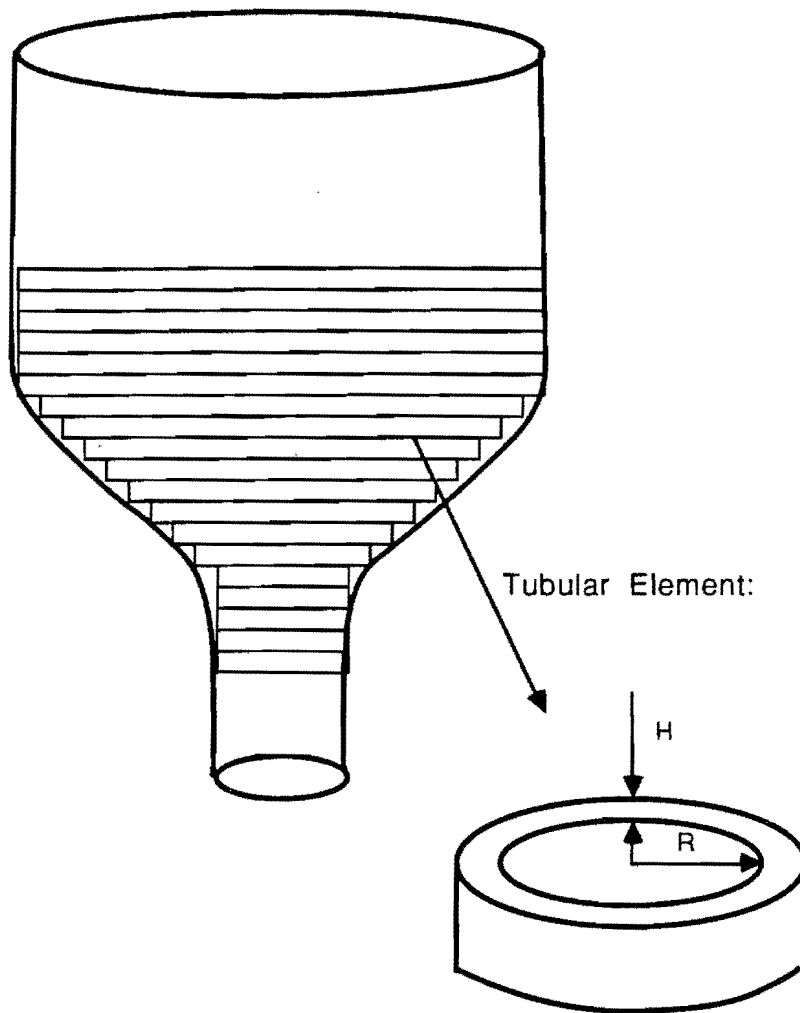


Figure 4-33 Schematic diagram of the modified physical approach to describe the tubular film blowing process.

$$\Delta P = \frac{H\sigma_{22}}{R} \quad (4-40)$$

where  $R$  and  $H$  are the radius and thickness of the tubular element, respectively, and the normal stresses,  $\sigma_{11}$  and  $\sigma_{22}$ , will be analyzed and derived in the following paragraphs.

(2) Kinematics

For an infinitesimal tubular element, let  $(V_1, V_2, V_3)$  be the corresponding velocity components in the coordinates  $(\xi_1, \xi_2, \xi_3)$  whose definition remains the same as that in Chapter 2. If Han and Park's assumption [11] is retained in which the shear components of the rate of strain is negligible for a plain film, then the rate-of-strain tensor is given by

$$d = \begin{vmatrix} d_{11} & 0 & 0 \\ 0 & d_{22} & 0 \\ 0 & 0 & d_{33} \end{vmatrix} \quad (4-41)$$

From the definition,  $d_{ij} = \frac{\partial v_j}{\partial x_i} + \frac{\partial v_i}{\partial x_j}$ , we have

$$d_{22} = \frac{2}{R} \frac{dR}{dt} \quad (4-42)$$

$$d_{33} = \frac{2}{H} \frac{dH}{dt} \quad (4-43)$$

Converting the above time derivative to a position derivative through the relationship  $(d/dt)=V_1(d/dZ)$ , Equations(4-42) and (4-43) become

$$d_{22} = \frac{2V_1}{R} \frac{dR}{dZ} \quad (4-44)$$

$$d_{33} = \frac{2V_1}{H} \frac{dH}{dZ} \quad (4-45)$$

Then, under the assumption of incompressible fluid, and by the continuity equation

$$d_{11} + d_{22} + d_{33} = 0 \quad (4-46)$$

we have

$$d_{11} = -2V_1 \left( \frac{1}{H} \frac{dH}{dZ} + \frac{1}{R} \frac{dR}{dZ} \right) \quad (4-47)$$

Moreover, with the aid of volumetric flow rate,  $Q=2\pi R H V_1$ , the  $d_{11}$ ,  $d_{22}$  and  $d_{33}$  are able to be rewritten as

$$d_{11} = \frac{-Q}{\pi R H} \left( \frac{1}{H} \frac{dH}{dZ} + \frac{1}{R} \frac{dR}{dZ} \right) \quad (4-48)$$

$$d_{22} = \frac{Q}{\pi R^2 H} \frac{dR}{dZ} \quad (4-49)$$

$$d_{33} = \frac{Q}{\pi R H^2} \frac{dH}{dZ} \quad (4-50)$$

In the direction "3", no external forces act on the outside surface of the bubble if the surface tension is negligible; thus, the stress at the outside surface, the free surface, is equal to the atmospheric pressure. However, the inside surface of the tubular film is not a free surface because of an inflating pressure acting on it. Hence, taking an average of the pressure difference,  $\Delta P$ , across the film, the total stress in the direction "3" is given by

$$\sigma_{33} = -p + \tau_{33} = \frac{-\Delta P}{2} \quad (4-51)$$

With the aid of Equation(4-51), it is easy to express the other two normal stresses as

$$\sigma_{11} = \frac{-\Delta P}{2} - \tau_{33} + \tau_{11} = \frac{-\Delta P}{2} + \eta ( d_{11}-d_{33} ) \quad (4-52)$$

$$\sigma_{22} = \frac{-\Delta P}{2} - \tau_{33} + \tau_{22} = \frac{-\Delta P}{2} + \eta ( d_{22}-d_{33} ) \quad (4-53)$$

where a Newtonian fluid is assumed. Combining Equations(4-39), (4-40), (4-48) - (4-50), (4-52) and (4-53), results in the following two first-order differential equations

$$\frac{dH}{dZ} = \frac{-H}{6\eta Q} [ 2\pi R \Delta P (R+H) + F ] \quad (4-54)$$

$$\frac{dR}{dZ} = \frac{R}{6\eta Q} [ \pi R \Delta P (4R+H) - F ] \quad (4-55)$$

### (3) Energy Balance

The energy balance established here is similar to that of Han and Park [5]. The following conditions are assumed:

(i) Compared with the major heat transfer by convection and radiation, the conductive heat transfer in the film is negligible.

(ii) The film is thin enough so that the temperature variation across it can be neglected.

(iii) The heat generation due to the frictional force and the viscous dissipation are small enough to be neglected. Thus, for an unit tubular element, shown as Figure 4-33, the energy balance equation is given by

$$\rho C_p \left( \frac{Q}{2\pi R} \right) \frac{dT}{dZ} = -U (T - T_{air}) - \epsilon \sigma (T^4 - T_r^4) + \rho \Delta H_f \left( \frac{Q}{2\pi R} \right) \frac{dX}{dZ} \quad (4-56)$$

where

$$\frac{dX}{dZ} = \frac{2\pi R H K X_f}{Q} \left( 1 - \frac{X}{X_f} \right) \quad (4-57)$$

Hence the energy balance equation can be expressed as a first-order differential equation with the aid of Equation(4-57)

$$\frac{dT}{dz} = -CR (T-T_{air}) - DR (T^4-T_r^4) + FX_fKRH \left(1 - \frac{X}{X_f}\right) \quad (4-58)$$

in which the definitions of the parameters C, D and F are all the same as Equations(4-28) - (4-30), respectively.

#### Numerical Procedure

From the above statements, the non-isothermal film blowing process for semi-crystalline material is governed by the four first-order differential equations, Equations(4-54), (4-55), (4-57) and (4-58). The fourth-order Runge-Kutta method was used to integrate these differential equations with the following initial conditions:

$$\text{at } Z=0: \quad R=R_0 \quad ; \quad H=H_0 \quad ; \quad T=T_0 \quad ; \quad X=0$$

Adjustment of the values of F and  $\Delta P$  allowed the calculated final radius and the frost line height to approach to the experimental results. Other details are the same as that for the old model.



## Comparison of New Mathematical Prediction and On-line Measurements

In the calculation of the new mathematical model, all the material parameters (such as  $\eta$ ,  $\rho$ ,  $K$ ,  $C_p$ ..., etc.,) and the processing parameters (such as  $U$ ,  $Q$ ,  $T_o$ ,  $T_{air}$ ..., etc.,) remain the same as those used in the old model. The values of  $\Delta P$  and  $F$  are adjusted to optimize the agreement between the predicted results and the on-line data. The comparison with the measured results for the radius, thickness, temperature and velocity profiles are shown in Figure 4-34 through Figure 4-37, and the theoretically predicted on-line crystallinity is also shown as Figure 4-38.

From Figures 4-34, 4-35 and 4-36, one is able to find that the theoretically predicted radius, thickness and temperature are in reasonable agreement with those measured, not only qualitatively but also quantitatively. Examining the calculated velocity profile, shown in Figure 4-37, a maximum appears around  $Z=10$  cm, and the final velocity is lower than the on-line value. This tendency of decreasing of the velocity at  $Z=10$  cm is due to the fact that at this position the predicted thickness almost approaches a constant value but the radius is still increasing. Hence, based on the equation of mass conservation,  $W=2\pi\rho R H V$ , it is easy to understand that a slight decrease of velocity occurs at  $Z=10$  cm.

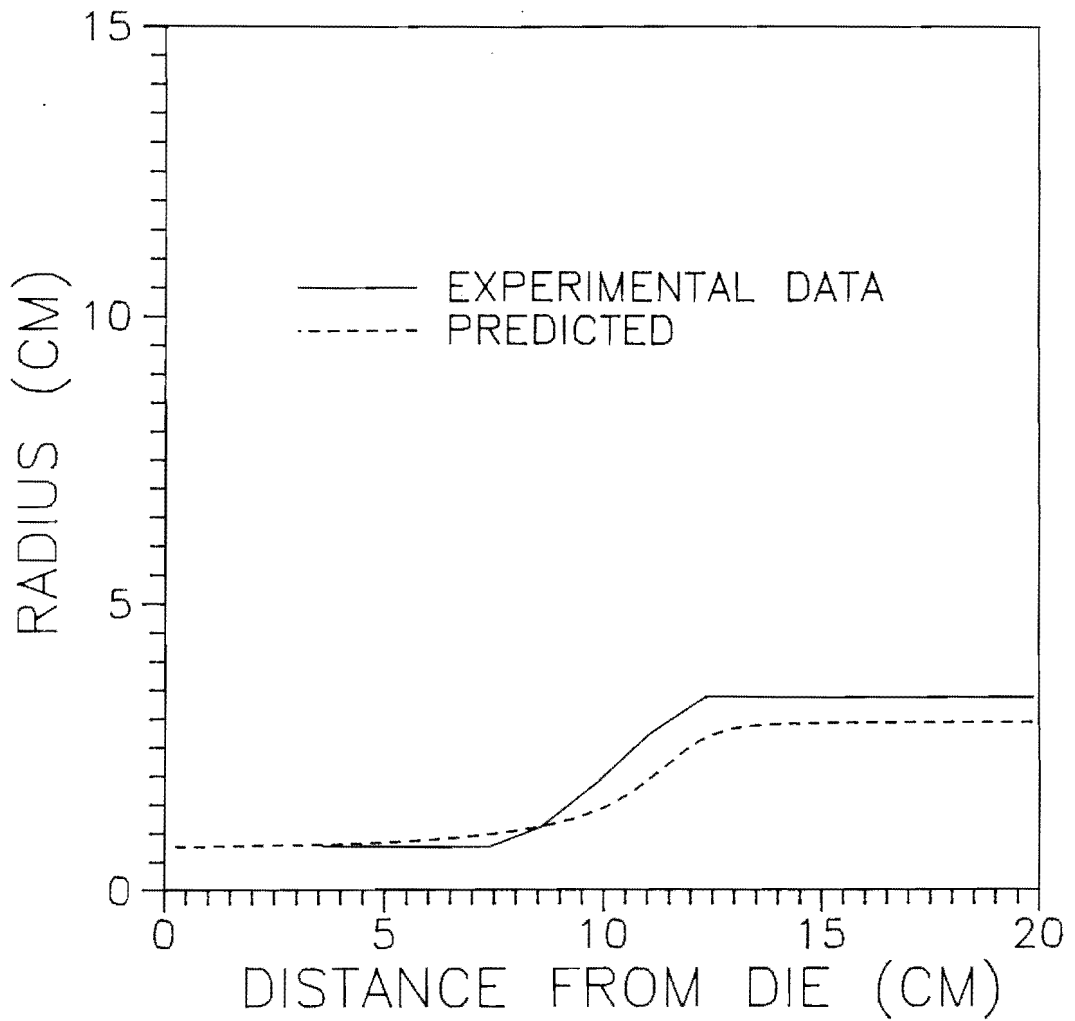


Figure 4-34 Comparison of the radius profile predicted by the proposed model with that from experimental measurement.

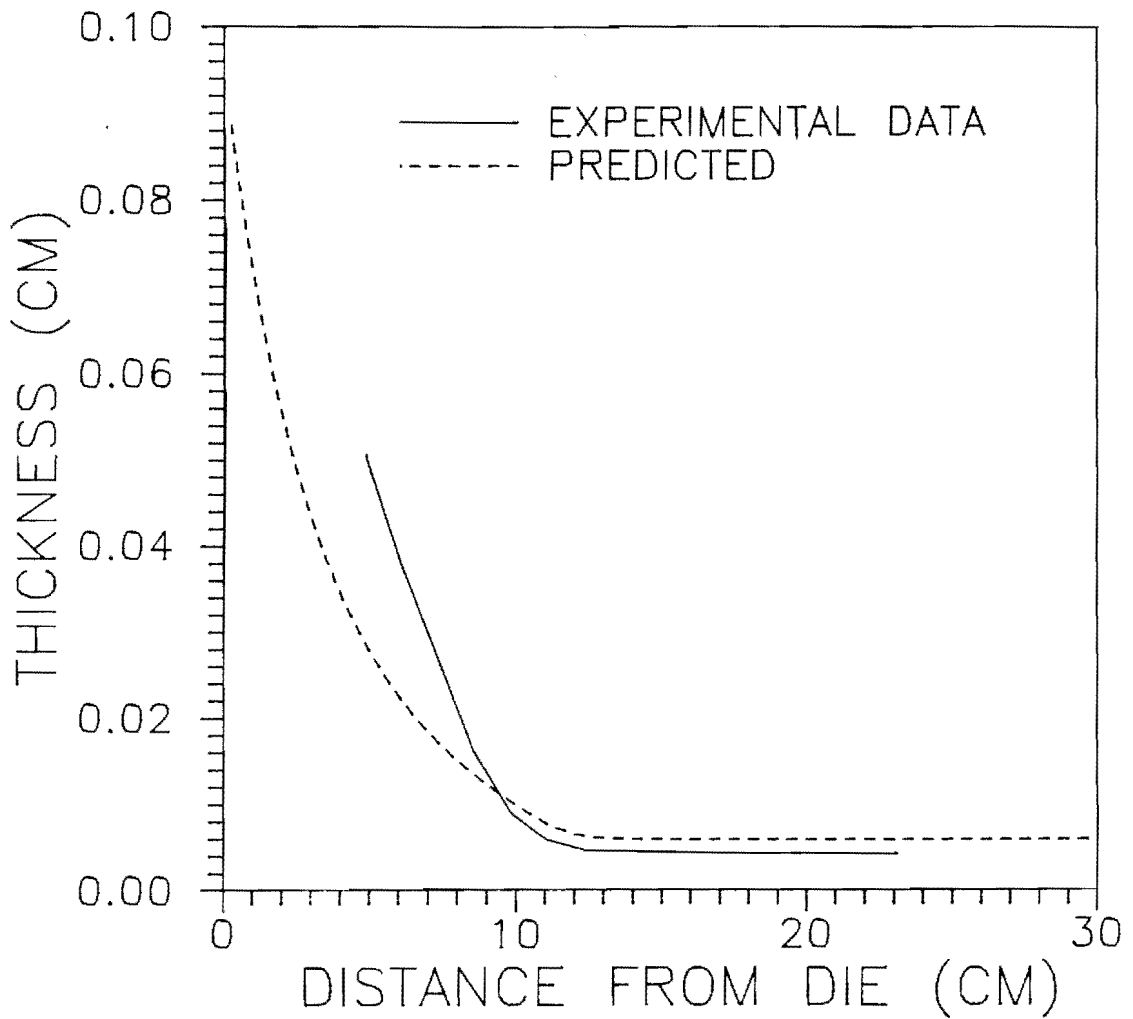


Figure 4-35 Comparison of the thickness profile predicted by the proposed model with that from experimental measurement.

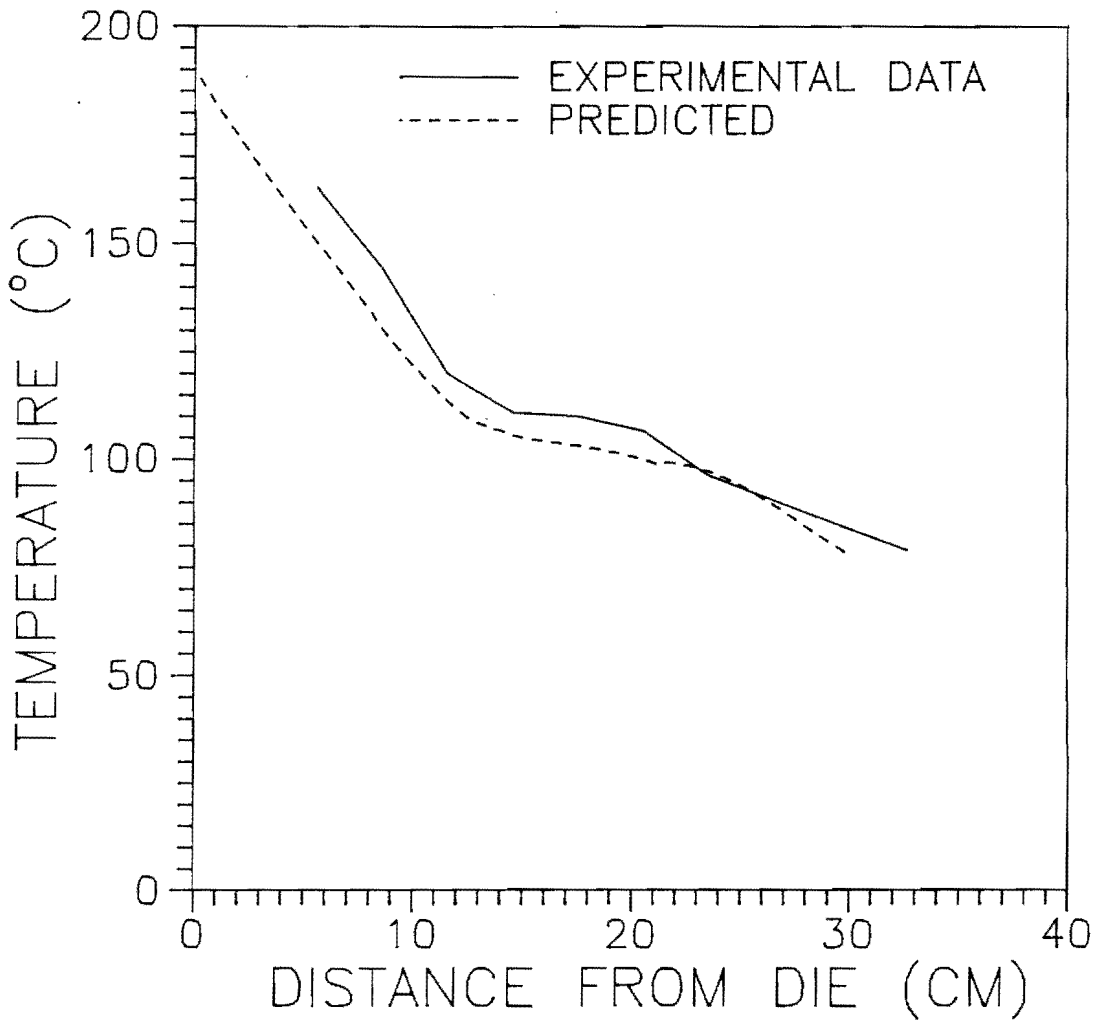


Figure 4-36 Comparison of the temperature profile predicted by the proposed model with that from experimental measurement.

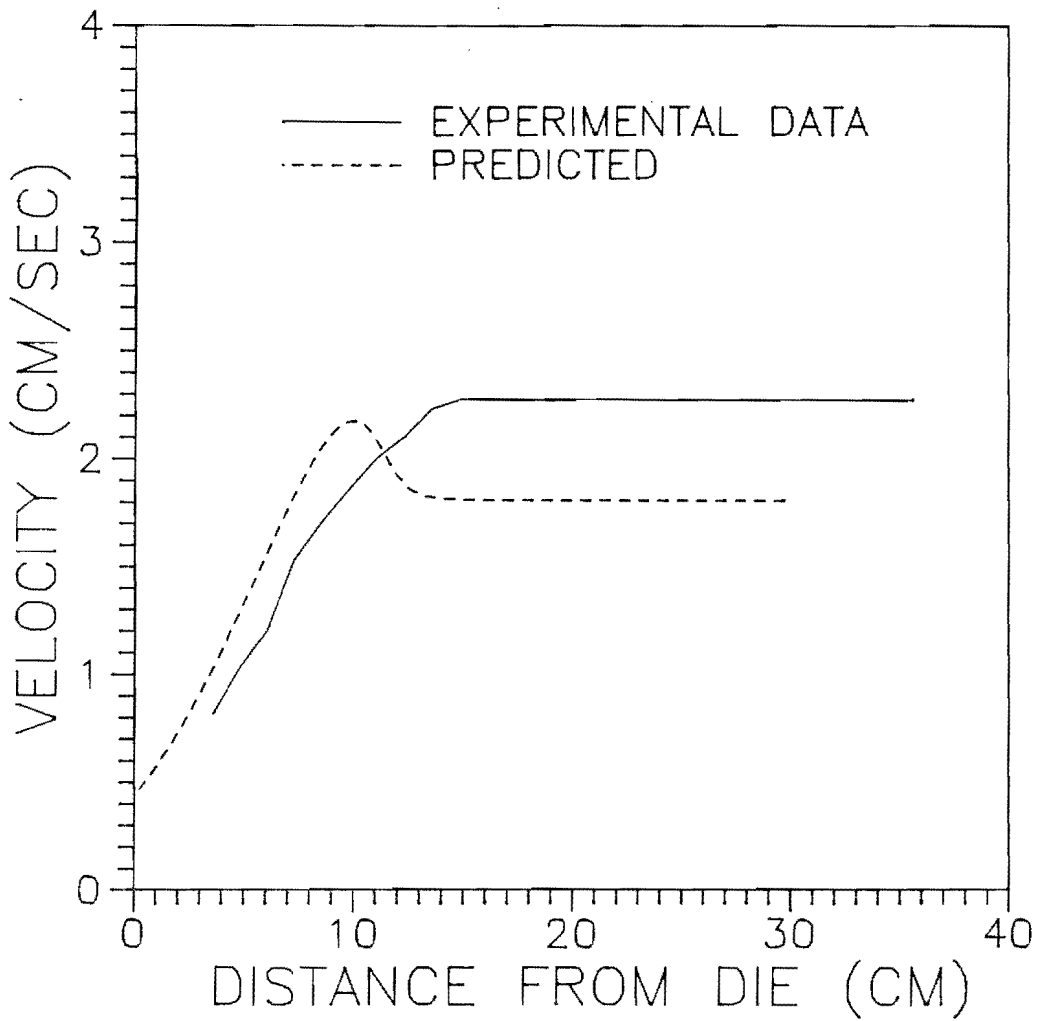


Figure 4-37 Comparison of the velocity profile predicted by the proposed model with that from experimental measurement.

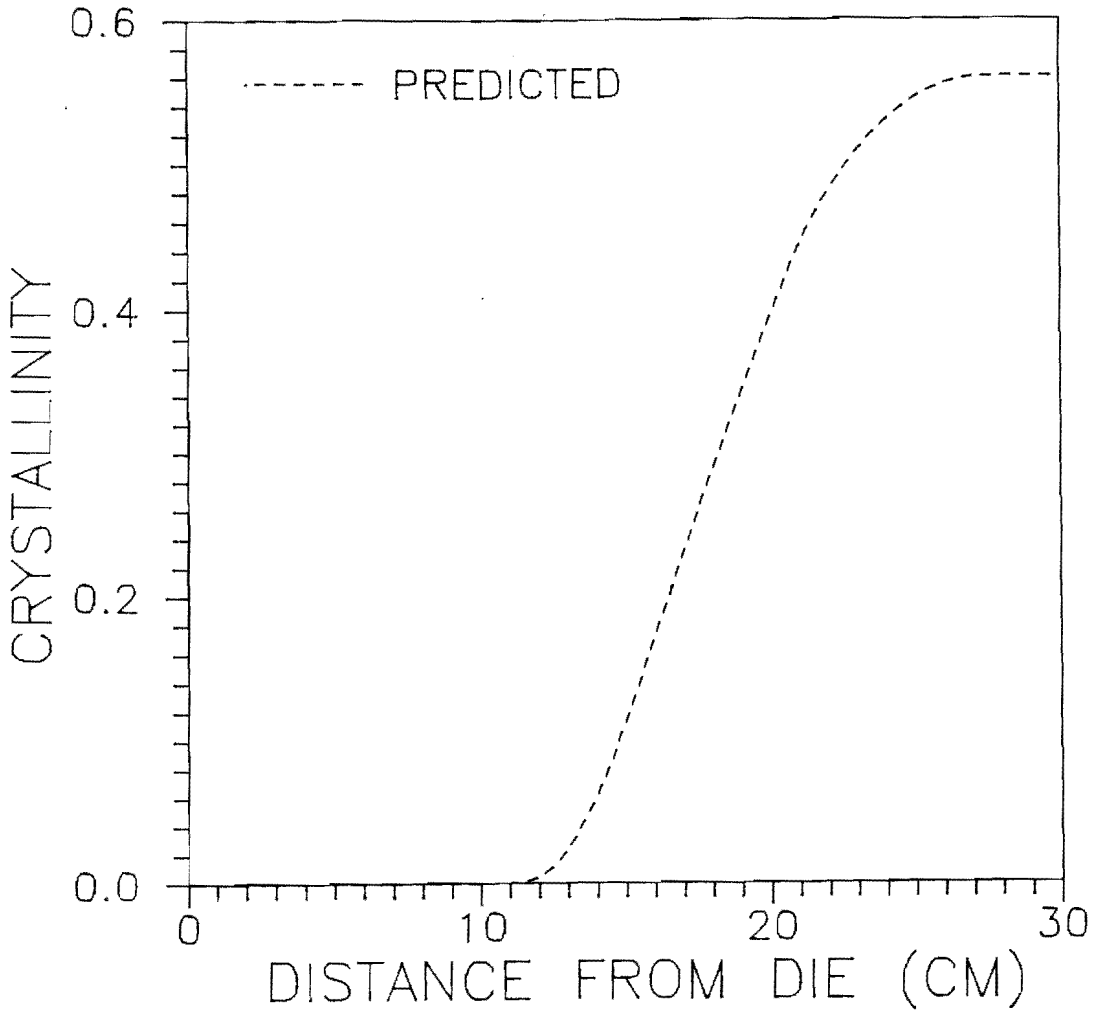


Figure 4-38 On-line crystallinity profile theoretically predicted by the proposed model.

Since practical values are used for all of the input parameters in this new model, it is necessary to know whether the adjusted and used values of  $\Delta P$  and  $F$  in this model are reasonable or not. The value of  $\Delta P$  used in the above theoretical computation is  $8500 \text{ dynes/cm}^2$ . The experimental  $\Delta P$  value measured by a water manometer in a steady state is about  $5900 \text{ dynes/cm}^2$ . Both of the  $\Delta P$  values are of the same order of magnitude. Hence, the  $\Delta P$  value used in the model is reasonable though not quantitative. With regard to the forces in the machine direction, a comparison is not possible because of the measured take-up force not being available in this study.

However, from the above comparison of  $\Delta P$  and from Figure 4-34 through Figure 4-37, it is clear that this new mathematical model provides a great improvement in the quantitative prediction of tubular film blowing process.

#### Characteristics of the New Equations

Carefully investigating Equations(4-54) and (4-55), several useful characteristics are observed:

- (1) Under either one of the following conditions
  - (i)  $F \geq 0$  and  $\Delta P > 0$
  - (ii)  $F > 0$  and  $\Delta P \geq 0$

the thickness of the molten film should always be decreasing, no matter how small the values of  $F$  and  $\Delta P$  are. Moreover, the

tendency of thickness decreasing ceases when the film reaches a solid state ( $\eta \rightarrow \infty$ ). It should be noticed that in film blowing process  $R_0$  is always larger than  $H_0$ .

(2) The way of radius change depends on the relative values of  $F$  and  $\Delta P$ . Under the assumption of  $R \gg H$ , Equation(4-55) can be simplified to

$$\frac{dR}{dZ} = \frac{R}{6\eta Q} ( 4\pi R^2 \Delta P - F ) \quad (4-59)$$

For a certain annular die with a fixed die radius  $R_0$ ,

(i) if  $\frac{F}{\Delta P} < 4\pi R_0^2$ , the bubble will be inflated and the

blow-up ratio is larger than unity;

(ii) if  $\frac{F}{\Delta P} = 4\pi R_0^2$ , the radius will remain the same as

that of the annular die, and the blow-up ratio is equal to one;

(iii) if  $\frac{F}{\Delta P} > 4\pi R_0^2$ , the bubble will be contracted and

the blow-up ratio is smaller than unity.

In this study  $R_0$  is equal to 0.7461 cm; then,  $4\pi R_0^2 = 6.995 \text{ cm}^2$ .

The radius profiles for the above three critical cases are shown as Figure 4-39. Furthermore, the effects of these three critical cases on the on-line thickness, temperature, velocity and crystallinity of the film are shown in Figures 4-40 through 4-43, respectively. From Figure 4-41, since the heat transfer effect decreases with the decrease of the the



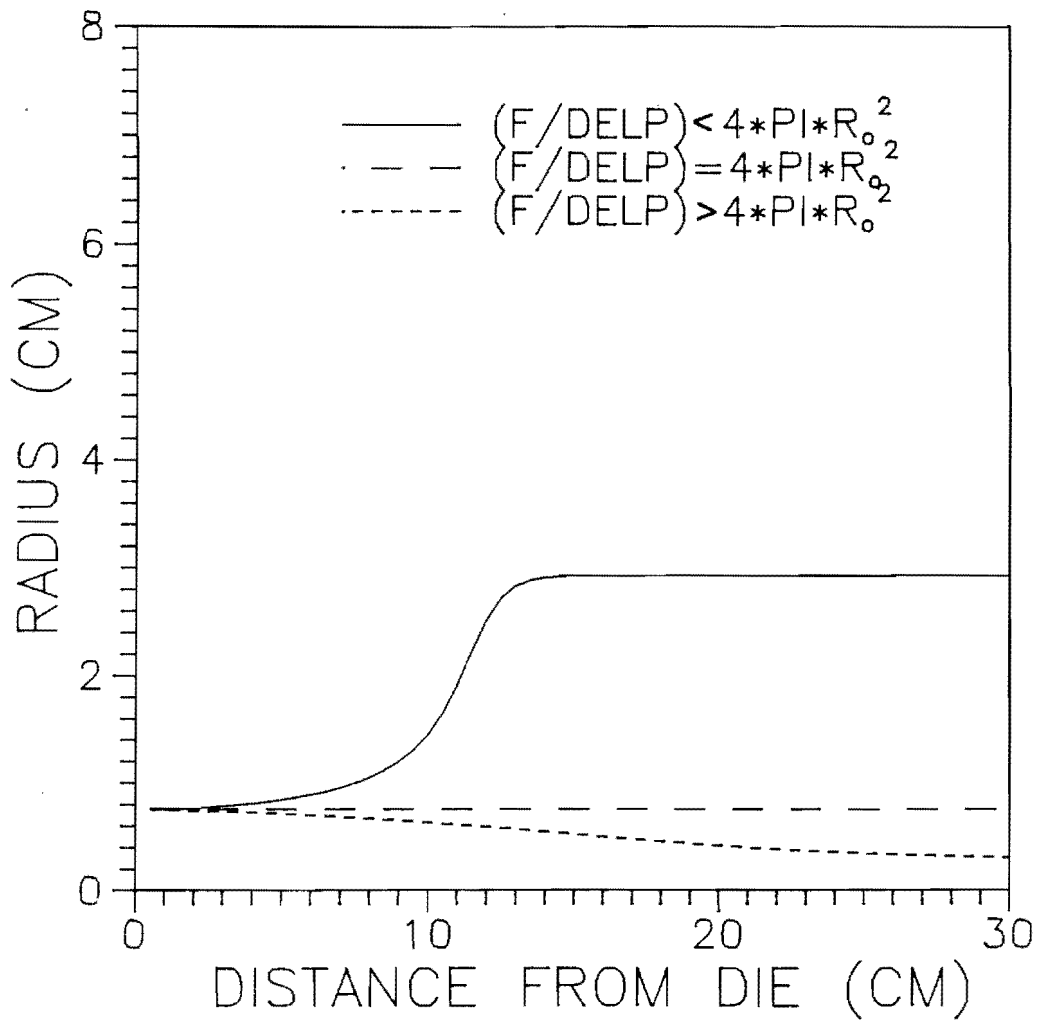


Figure 4-39 Radius profiles of the three critical cases of  $F/\Delta P$  theoretically predicted by the proposed model.

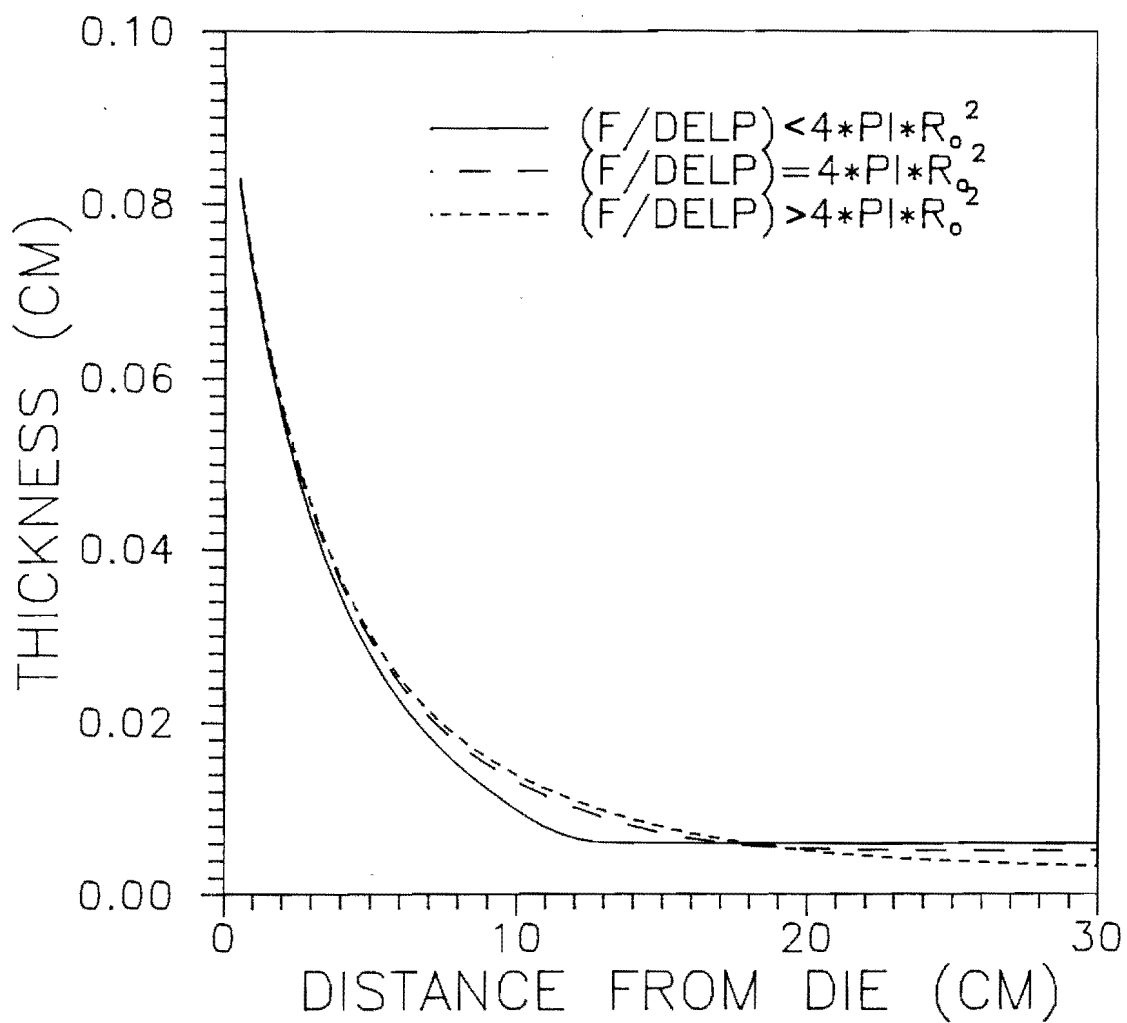


Figure 4-40 Thickness profiles of the three critical cases of  $F/\Delta P$  theoretically predicted by the proposed model.

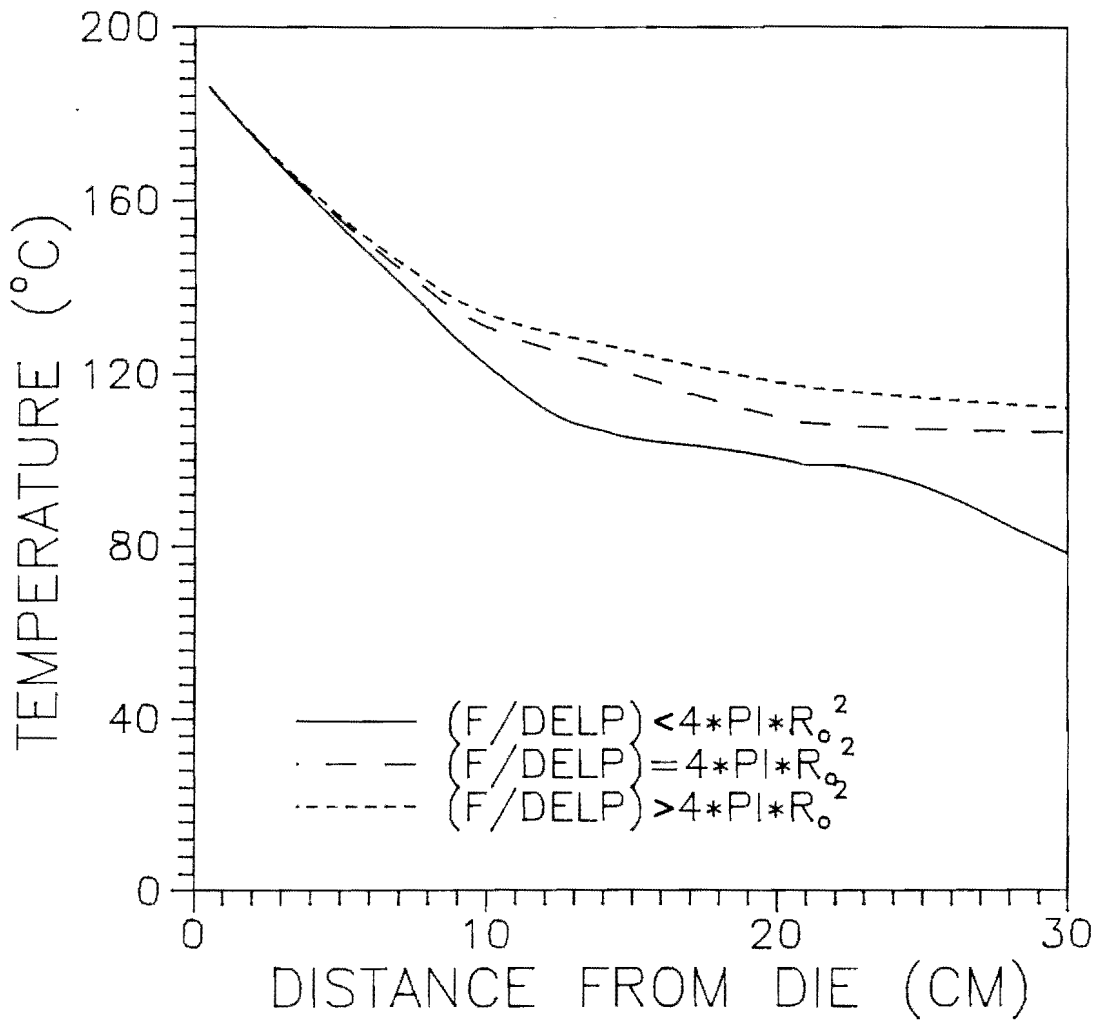


Figure 4-41 Temperature profiles of the three critical cases of  $F/\Delta P$  theoretically predicted by the proposed model.

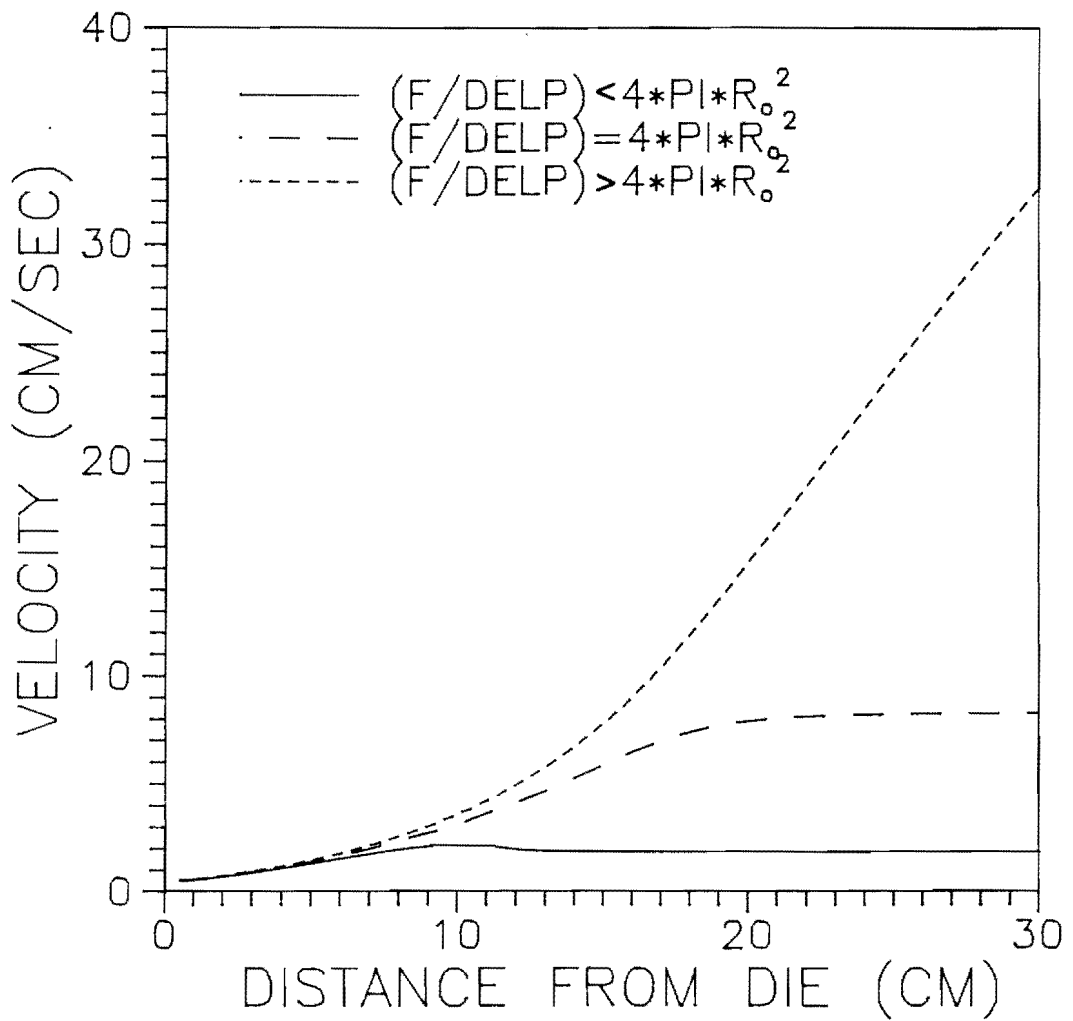


Figure 4-42 Velocity profiles of the three critical cases of  $F/\Delta P$  theoretically predicted by the proposed model.

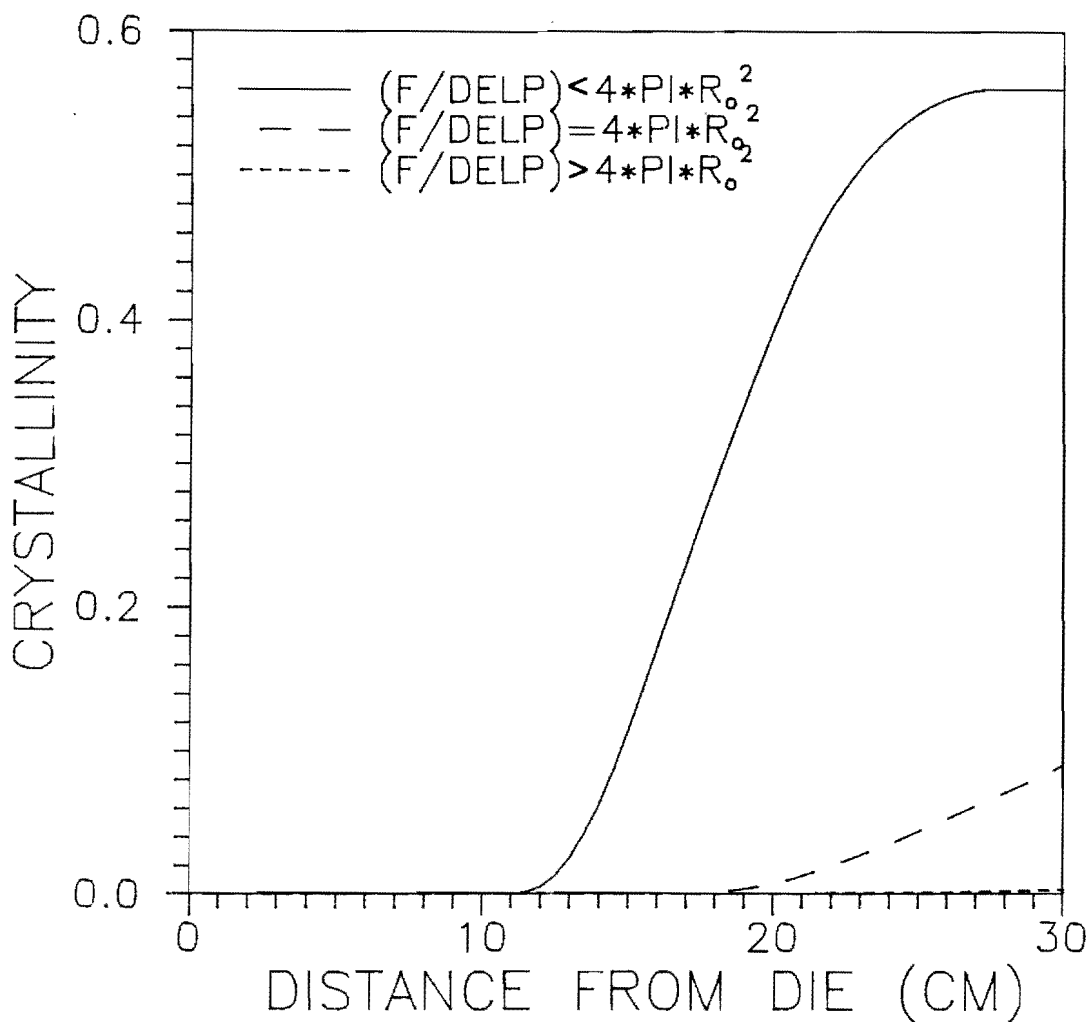


Figure 4-43 Crystallinity profiles of the three critical cases of  $F/\Delta P$  theoretically predicted by the proposed model.

total surface area, the on-line temperatures increase with the decrease of blow-up ratio.

The on-line temperature change, due to the ratio of  $F/\Delta P$ , will directly affect the thickness and crystallinity profile. First, the on-line thickness is inspected. According to the mass conservation, the film should be thicker under the condition of smaller blow-up ratio (i.e., smaller final radius). The initial part of the three thickness profiles in Figure 4-40 certainly have this tendency. However, the final thickness of the three cases is opposite to the above prediction. The main reason why is that the film with smaller blow-up ratio is more difficult to reach its solidification temperature; thus, the thickness will continue to decrease (under the effects of the constant external forces) until the solidification occurs. Hence, in case(2)(iii), the film is thinnest and has a highest final velocity, shown as Figure 4-42. Secondly, for the case of lower blow-up ratio, its local (on-line) crystallinity is smaller, shown in Figure 4-43, just due to its higher local temperature.

(3) Even under a certain special processing condition, Equations(4-54) and (4-55) are also able to successfully give a qualitative description of the processing system. For example, if  $\Delta P$  is equal to zero and the take-up force cannot overcome the downward force (such as the gravitational force), then the whole tubular film will "collapse" and

become thicker and thicker due to the continuous accumulation of the melt from the extruder. From Equation(4-54), the thickness of the film increases when  $\Delta P=0$ , and  $F$  is negative.

#### Comparison of the Modified Model and the Original One

Although Equations(4-54) and (4-59) are derived directly from a physical picture, they can be also obtained as a special case of the original model proposed by Petrie and Pearson [3,4]. This is done by omitting consideration of the variable  $\theta$  and the second derivative of radius  $d^2R/dZ^2$  in Equations(4-14) - (4-16).

Viewing these two mathematical models, the original one seems to have a better and more complete geometrical consideration of the tubular film. However, a difference exists between the behavior of these two models. Under a special processing condition - uniaxial stretching, i.e.,  $\Delta P=0$ , the predicted radius profiles by different models are compared in Figure 4-44. The solid line in Figure 4-44, the radius profile predicted by the proposed equations, shows that a tubular film will be contracted due to the pulling of the take-up force; moreover, this result is qualitatively consistent with the photographs shown in the literature by Han and Park [11]. However, the trend of the radius change predicted by the original model, the dashed line in Figure 4-

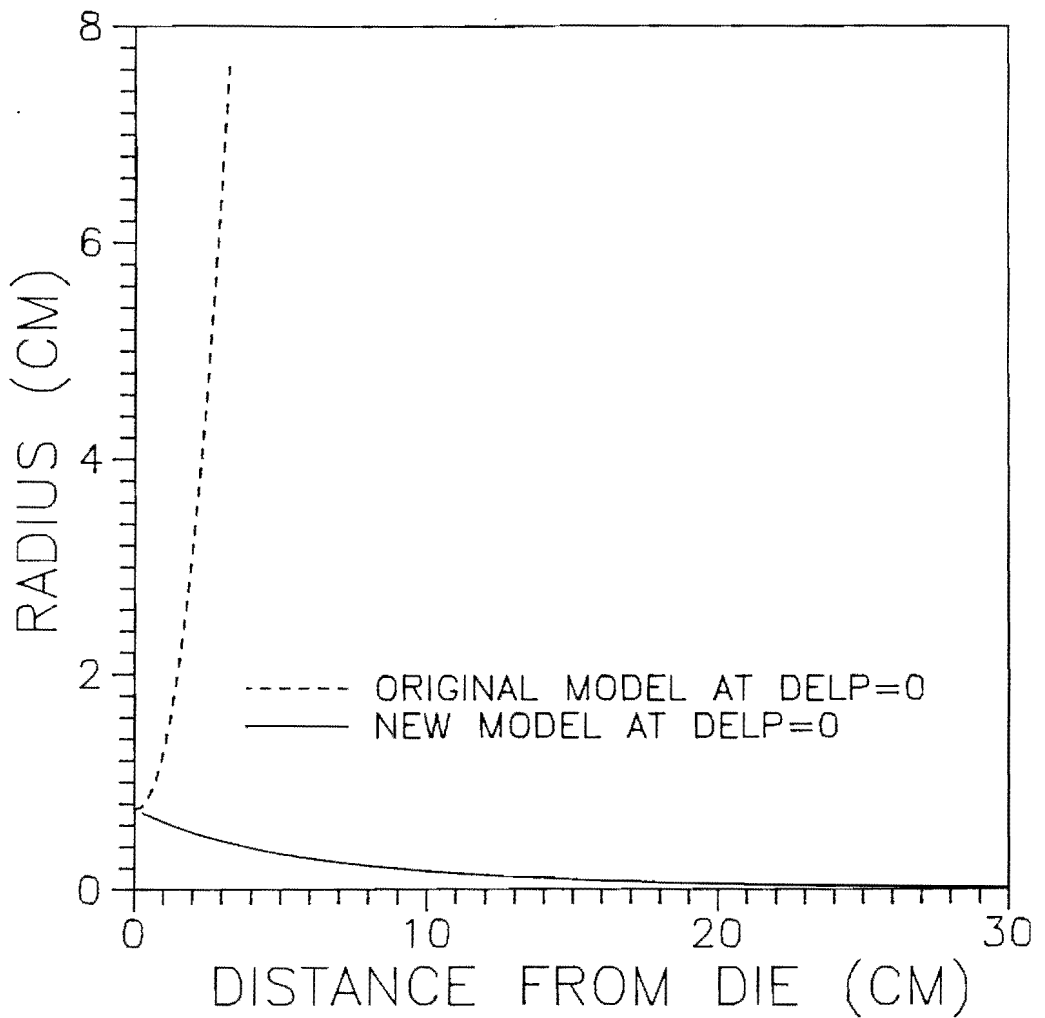


Figure 4-44 Comparison of the radius profiles predicted by the original model and by the proposed model under the condition of  $\Delta P = 0$ .



44, is not only opposite to the practical picture but also not expected physically.

The physical reason for the inverse effect of  $\Delta P$ , which was shown in Section 4.2 and the above statements, is not at all clear. When there is a significant radius of curvature in the machine direction (i.e., when the second derivative  $d^2R/d^2Z$  is large)  $\Delta P$  contributes to the stress in the machine direction as well as to the stress in the hoop direction. Under these conditions  $\Delta P$  tends to add or subtract from the applied force in the machine direction, depending on the sign of the second derivative. Therefore, probably the geometric formulation involving the radius of curvature must be modified. In any case the failure of the curvature term to act in a manner consistent with the data needs to be considered carefully in future work.

#### Predictions of the New Mathematical Model

The proper performance of this proposed model has been shown by a good agreement with the experimental observations in the preceding paragraphs. Since a proper mathematical model was obtained, it is important to realize how the radius, thickness, temperature and crystallinity profiles vary with the variations in processing conditions and with the characteristics of the material. These effects are examined in the following paragraphs.

### (1) Influence of Take-up Force

The influences of the net take-up force  $F$  on radius, thickness, temperature and crystallinity are shown in Figures 4-45 to 4-48, in which  $F_1 > F_2 > F_3$ . For larger  $F$ , the final films become thinner and the frost line is higher. Owing to the largest deformation of thickness for  $F_1$ , the final radius in the case of  $F_1$  becomes smallest (the values of  $\Delta P$  in the three cases are all the same). Moreover, as was mentioned in the previous chapter, the heat transfer is mainly controlled by convection and radiation. Since the total surface area of a tubular film is the key factor for heat convection and radiation, the larger radius (i.e., the higher blow-up ratio) will have a lower on-line temperature and this will produce an increase in the crystallization rate (due to the larger supercooling).

### (2) Influence of Inflating Pressure

Figures 4-49 through 4-52 show that  $R(Z)$ ,  $H(Z)$ ,  $T(Z)$  and  $X(Z)$  profiles as a function of inflating pressure  $\Delta P$ , in which  $\Delta P_1 > \Delta P_2 > \Delta P_3$ . At fixed values of the other parameters, a higher pressure difference across the film will produce a larger tubular film; moreover, the initial inflated position is closer to the die exit. These predicted results just agree with our intuitive expectation. For the different  $\Delta P$ , the final thickness is a result of competition between the continuity equation and the temperature-dependent viscosity

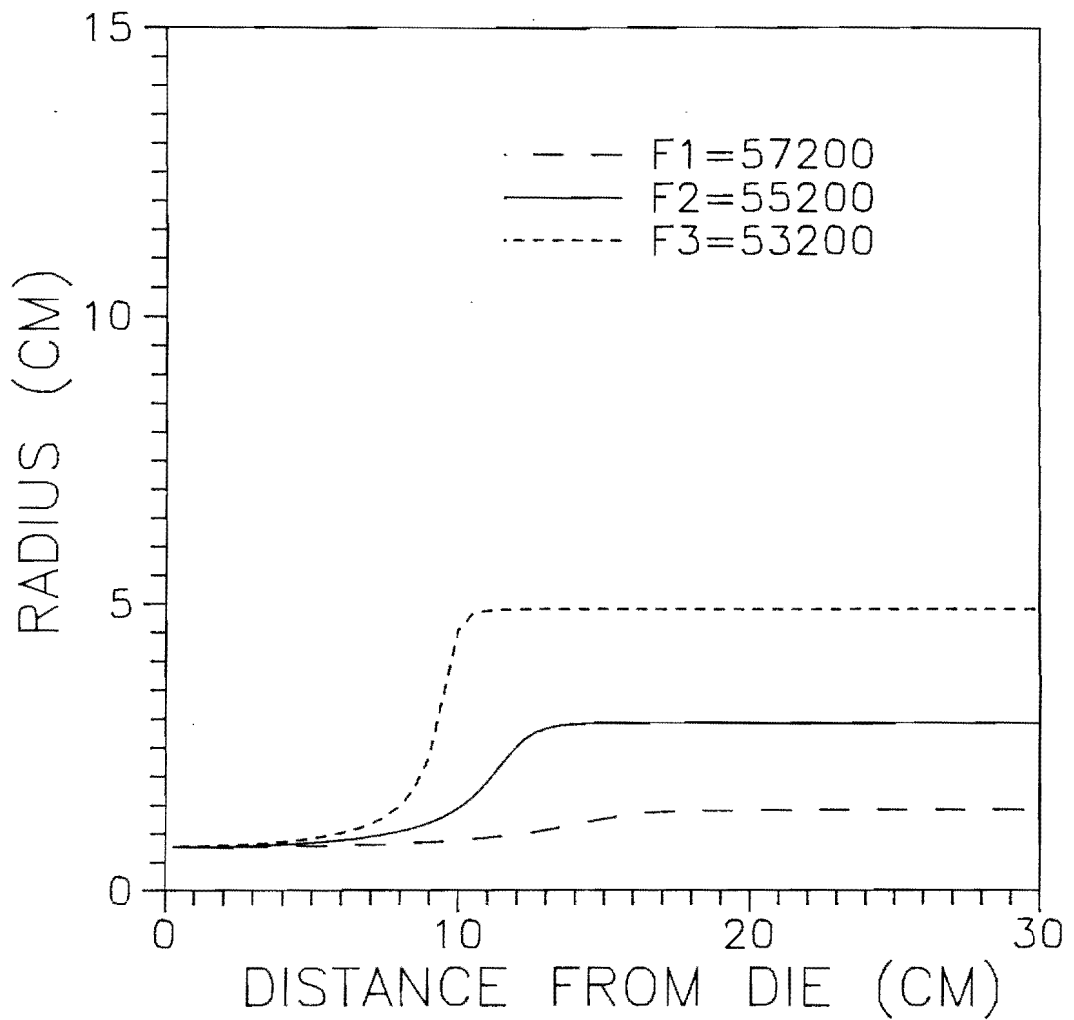


Figure 4-45 Comparison of the predicted radius profiles by the proposed model for different F values.

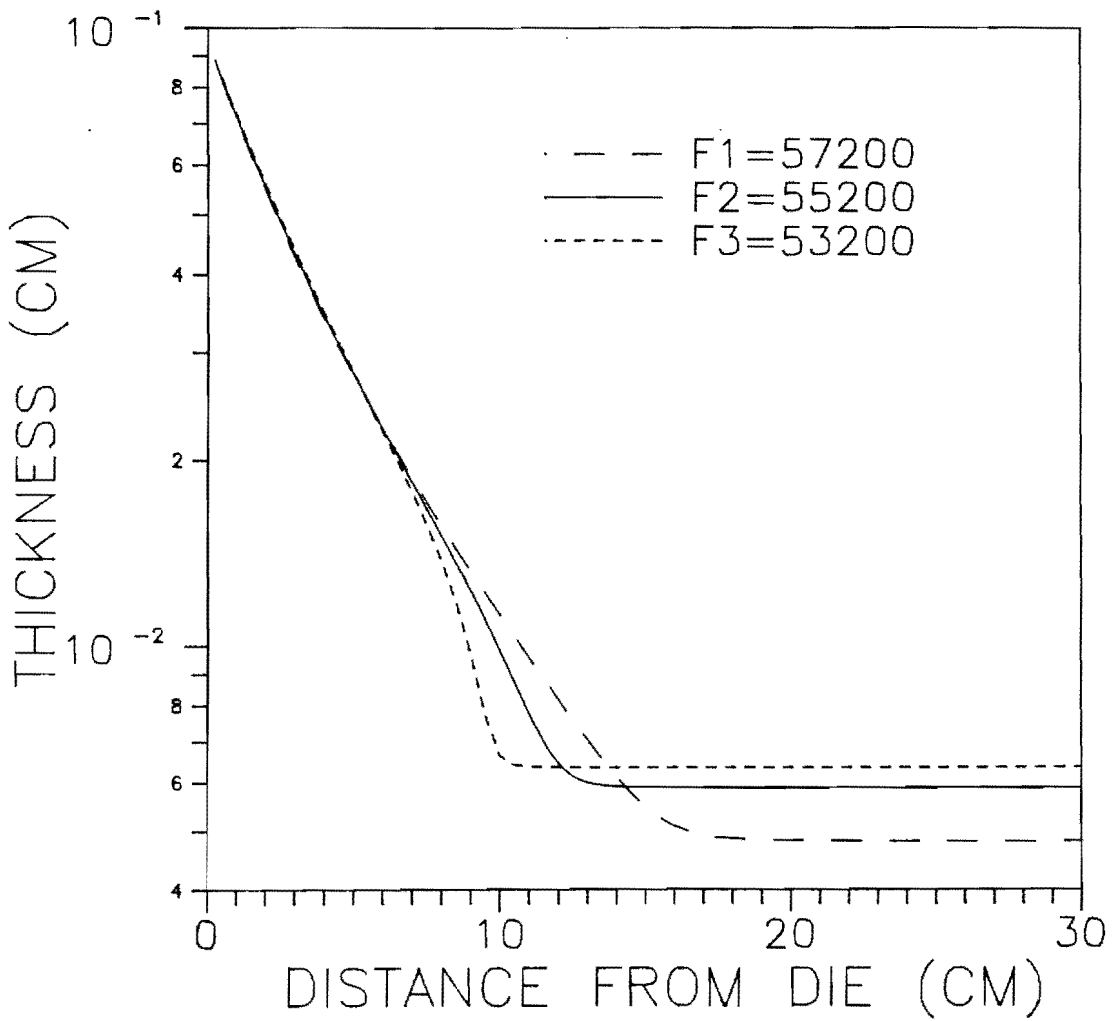


Figure 4-46 Comparison of the predicted thickness profiles by the proposed model for different F values.

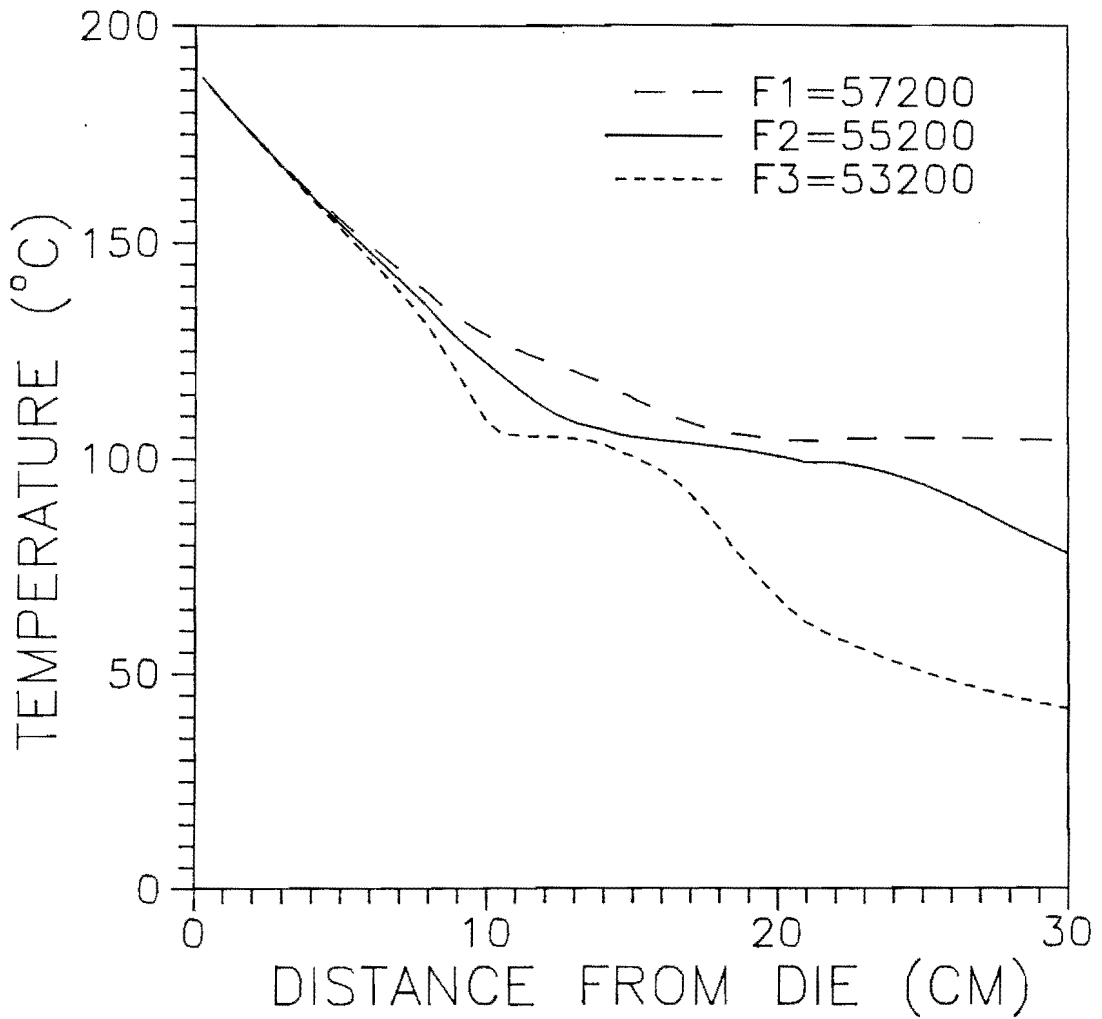


Figure 4-47 Comparison of the predicted temperature profiles by the proposed model for different F values.

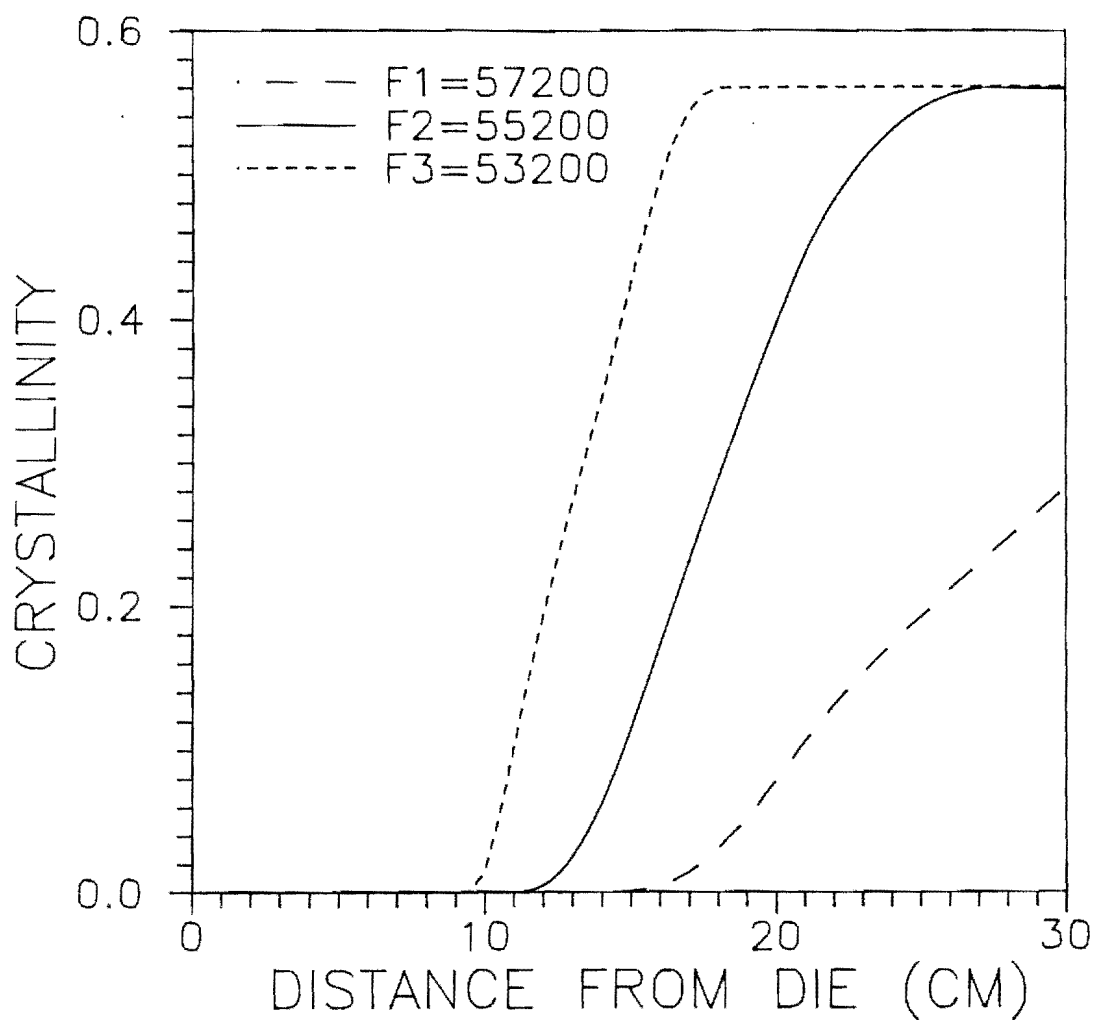


Figure 4-48 Comparison of the predicted crystallinity profiles by the proposed model for different F values.

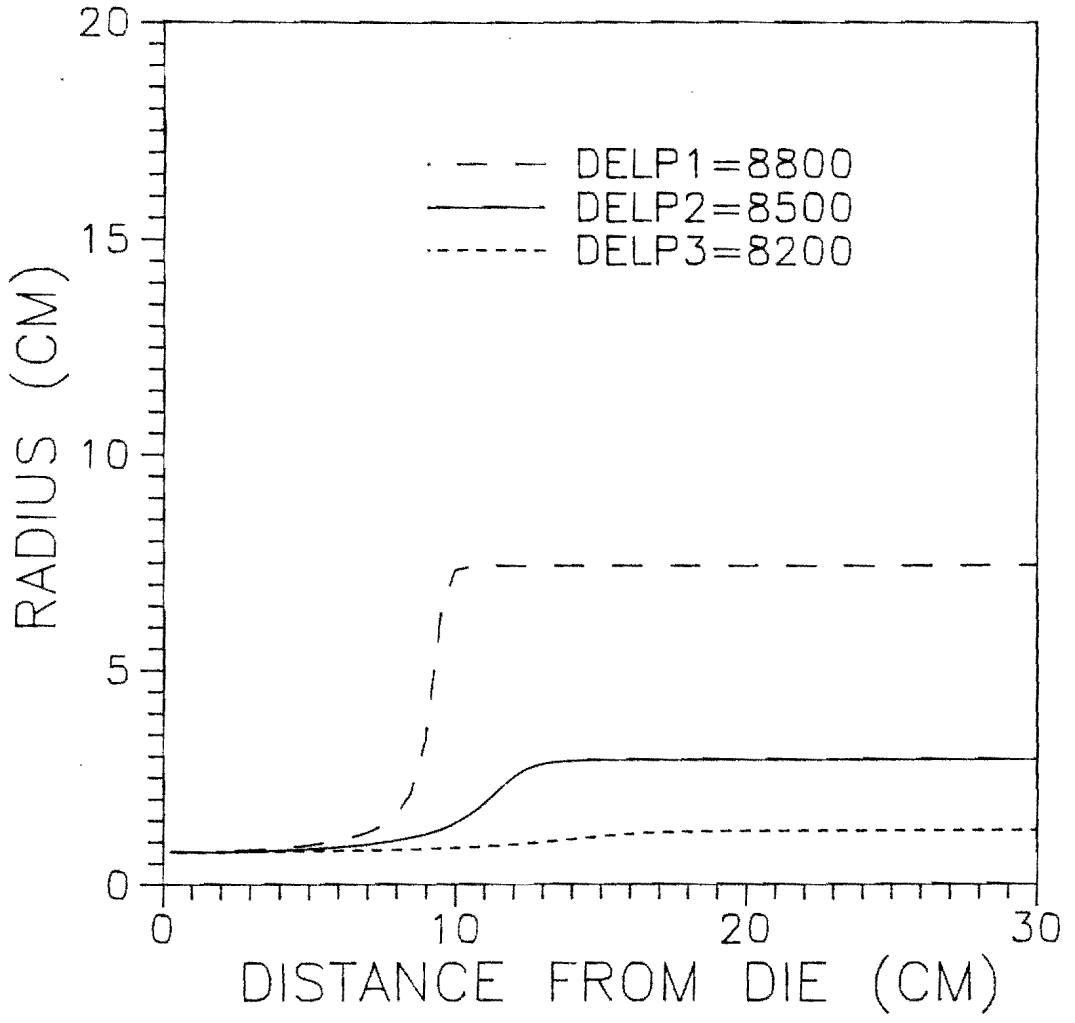


Figure 4-49 Comparison of the predicted radius profiles by the proposed model for different  $\Delta P$  values.

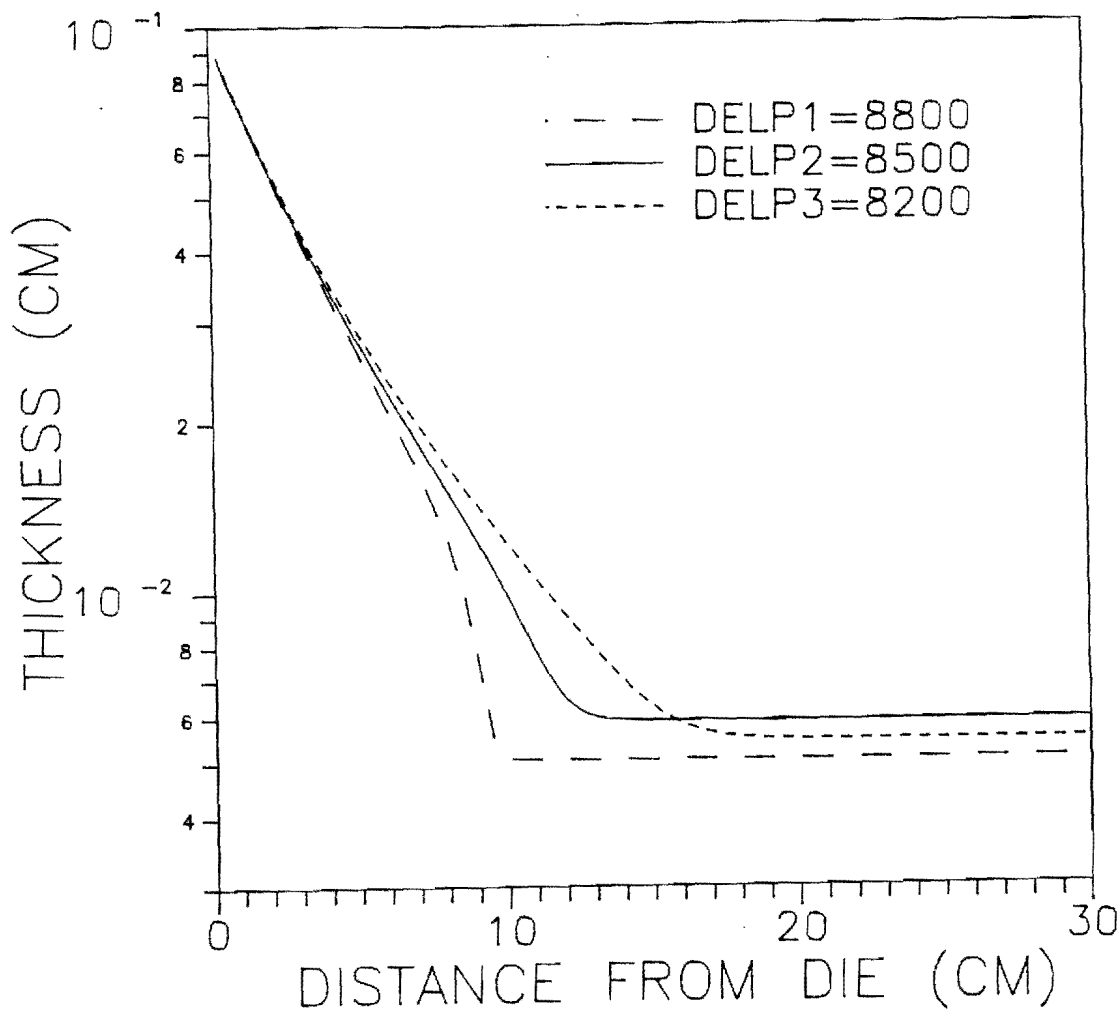


Figure 4-50 Comparison of the predicted thickness profiles by the proposed model for different  $\Delta P$  values.



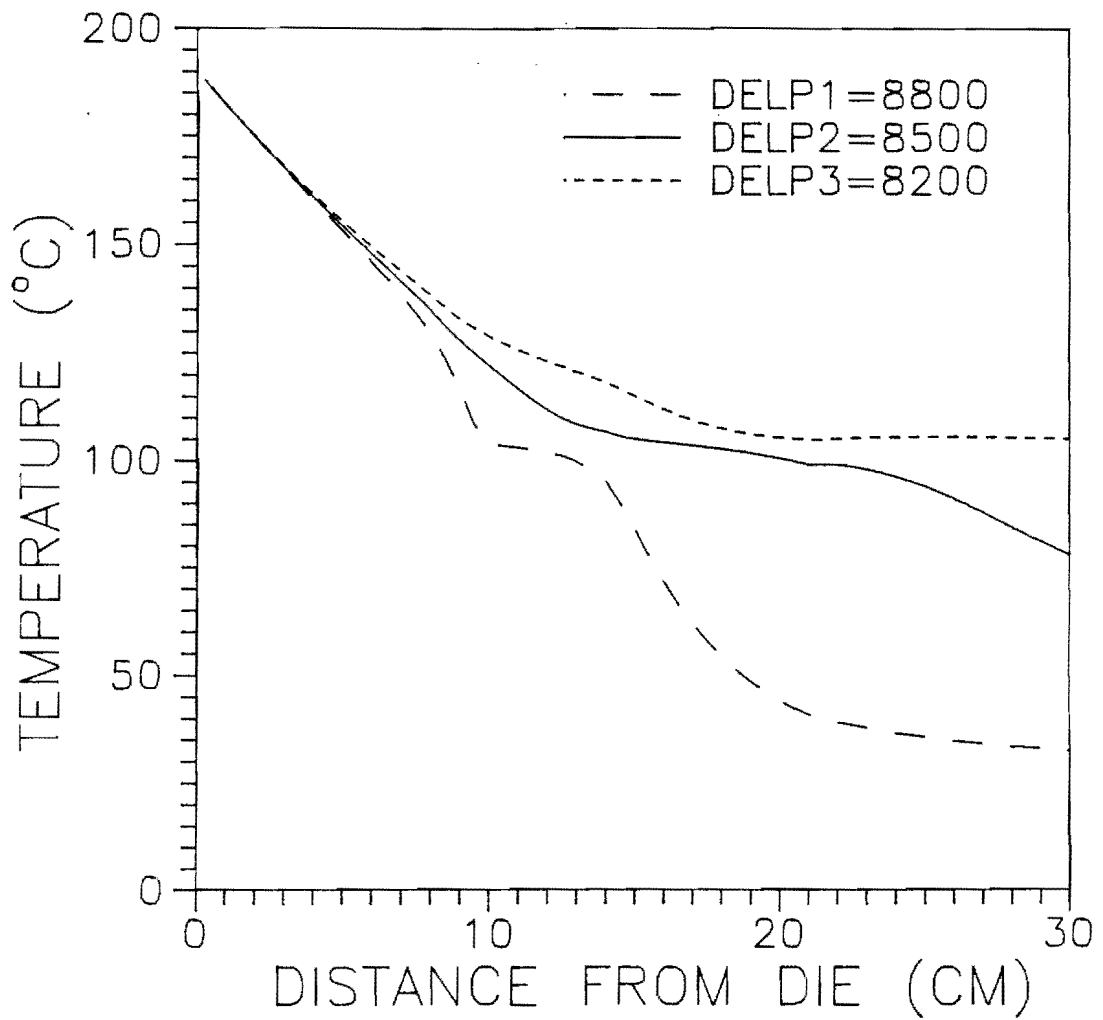


Figure 4-51 Comparison of the predicted temperature profiles by the proposed model for different  $\Delta P$  values.

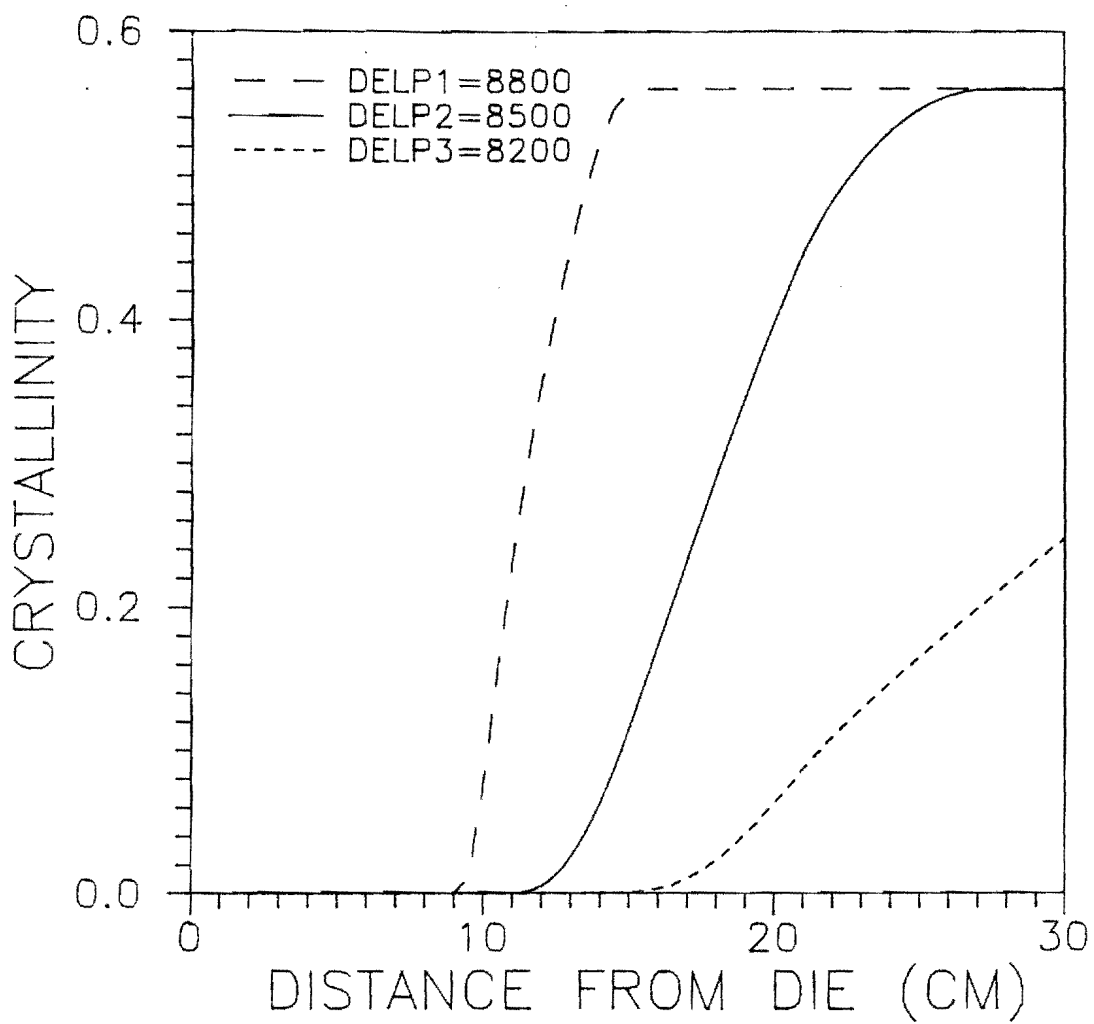


Figure 4-52 Comparison of the predicted crystallinity profiles by the proposed model for different  $\Delta P$  values.

equation. According to mass conservation, a larger radius causes a thinner film, but a larger radius would cease the deformation of thickness more quickly due to a higher cooling rate. Thus, the case of  $\Delta P_1$  is the one which has the lowest frost line, and the order of the final thickness for those three different  $\Delta P$  is  $H_2 > H_3 > H_1$ .

### (3) Influence of Initial Temperature

The extrusion temperature is one of the most important processing conditions. The temperature at the die will affect all of the other on-line quantities. For different initial temperatures  $T_{01} > T_{02} > T_{03}$ , the on-line profiles of  $R(Z)$ ,  $H(Z)$ ,  $T(Z)$  and  $X(Z)$  are shown as Figures 4-53 to 4-56. Since, for most polymeric materials their viscosities are strongly dependent on temperature, the higher initial temperature will cause a smaller viscosity and a larger deformation of radius and thickness under the condition of fixed  $F$  and  $\Delta P$ . Hence, for the final radius and thickness, we have  $R_{L1} > R_{L2} > R_{L3}$  and  $H_{L1} < H_{L2} < H_{L3}$ . However, although the initial temperatures are  $T_{01} > T_{02} > T_{03}$ , the local temperatures beyond the position where the bubble has been inflated, around  $Z=10$  cm, are  $T_3 > T_2 > T_1$ , which is owing to the radius-dependent heat transfer. Hence the case of  $T_{01}$  provides the largest supercooling condition for the development of crystallinity in the film. The crystallization rates for these three cases are shown as Figure 4-56.

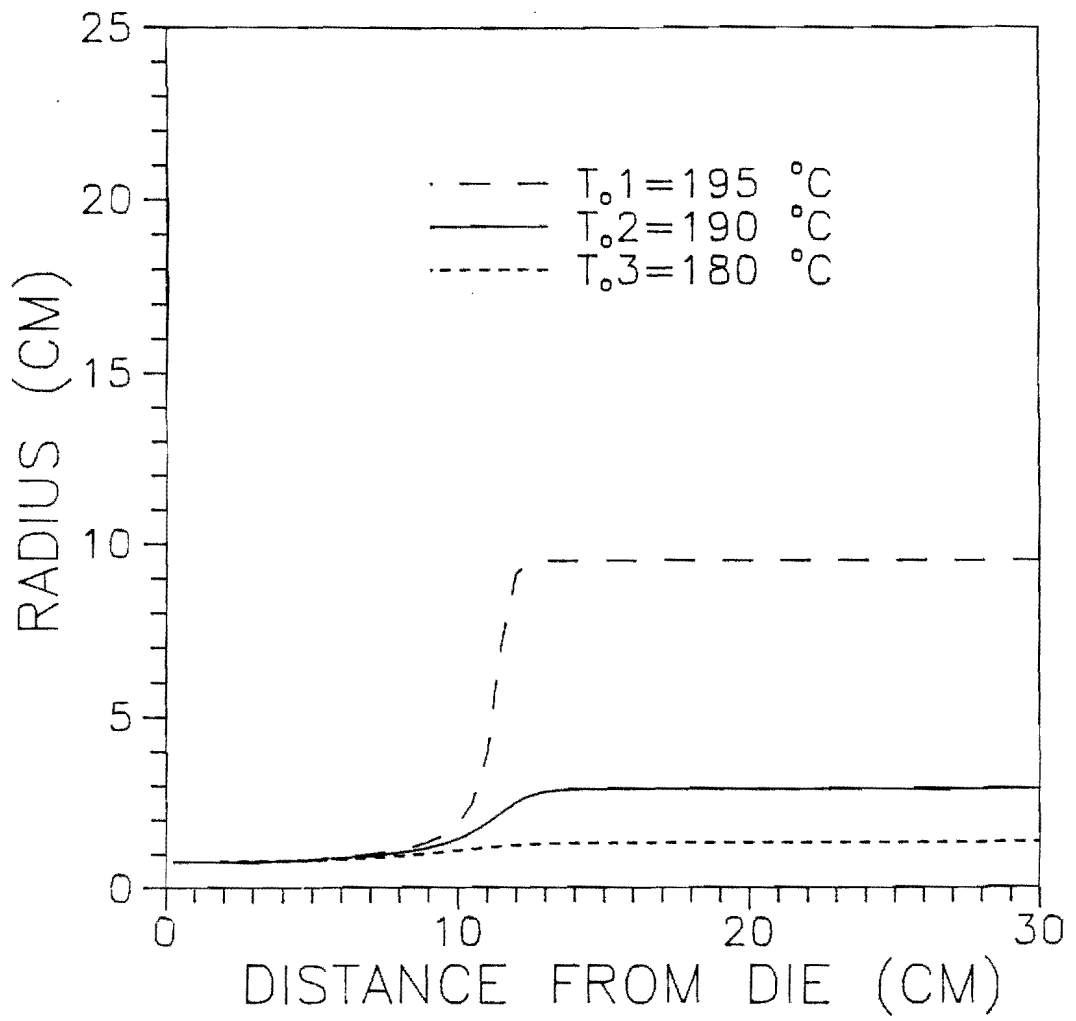


Figure 4-53 Comparison of the predicted radius profiles by the proposed model for different  $T_o$  values.

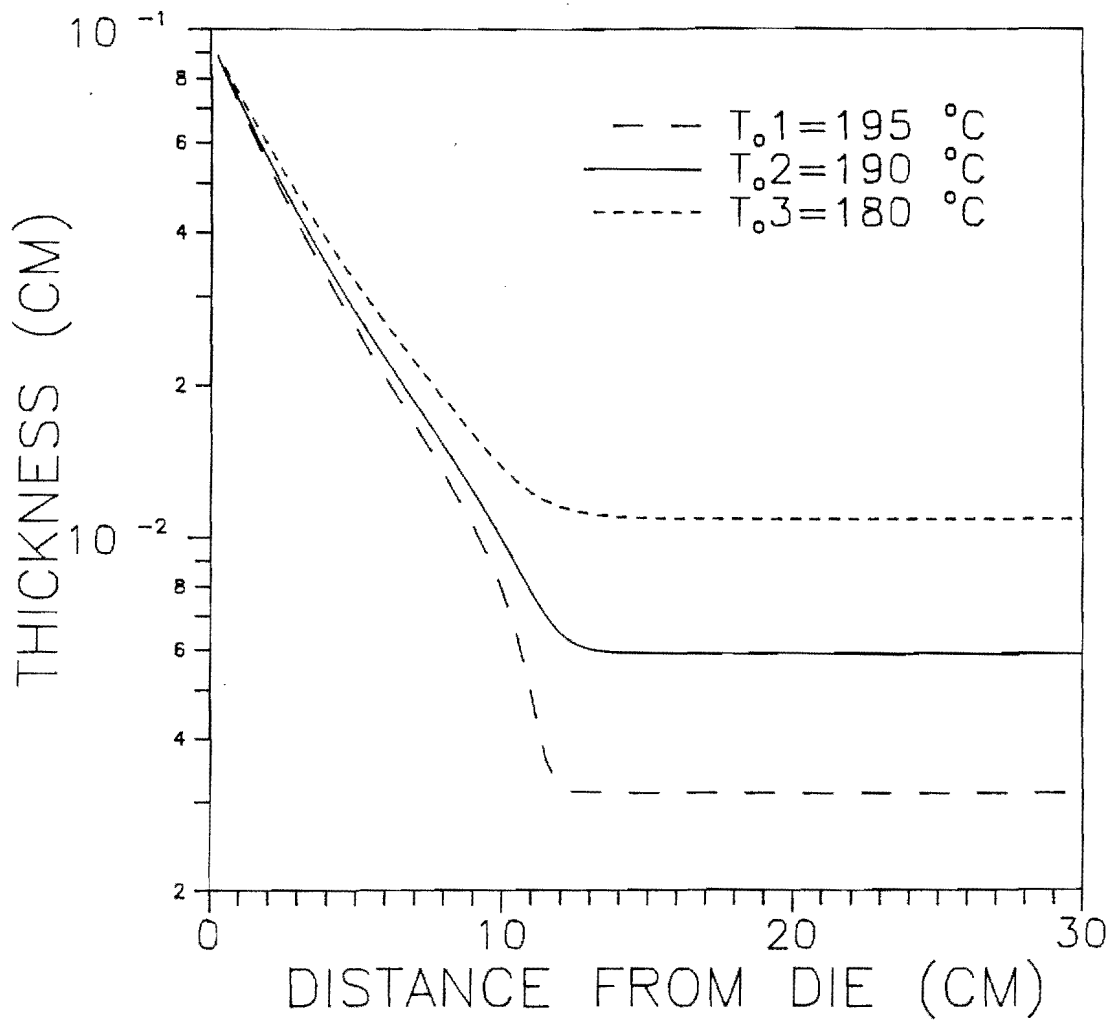


Figure 4-54 Comparison of the predicted thickness profiles by the proposed model for different  $T_o$  values.

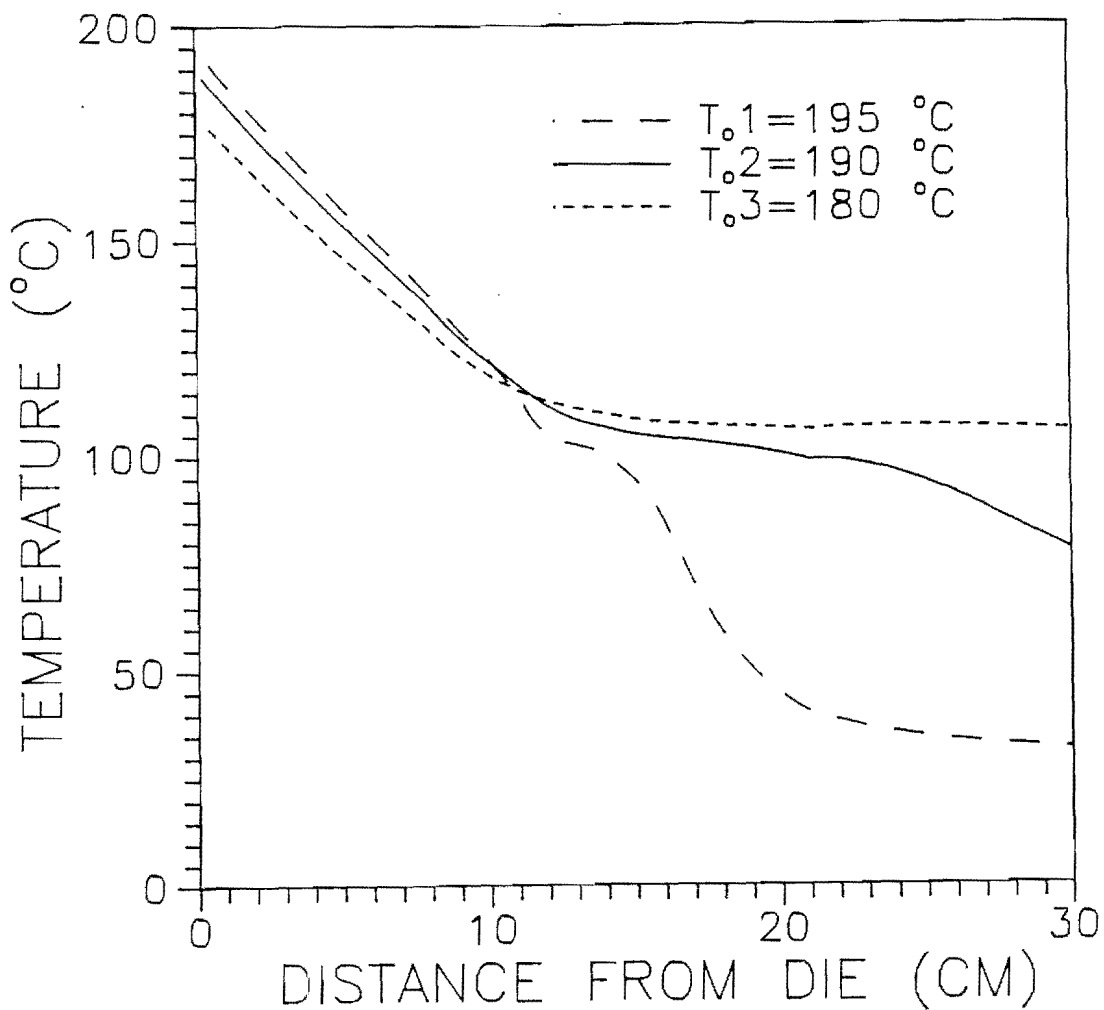


Figure 4-55 Comparison of the predicted temperature profiles by the proposed model for different  $T_0$  values.

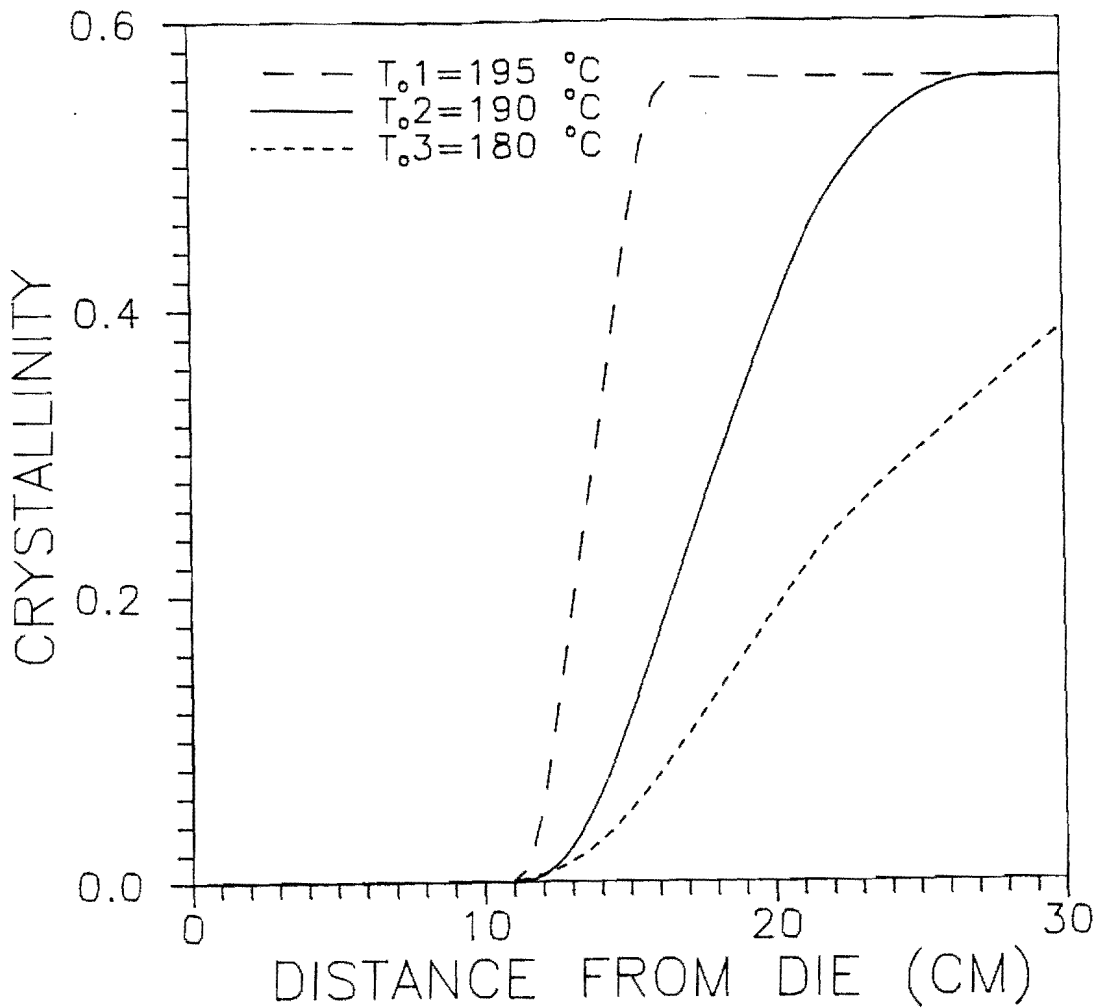


Figure 4-56 Comparison of the predicted crystallinity profiles by the proposed model for different  $T_0$  values.

#### (4) Influence of the Rheological Activation Energy

The activation energy of viscous flow  $E_a$  is directly related to the parameter  $b$  in Equation(4-31), i.e.,  $b=E_a/R_g$ , where  $R_g$  is the gas constant. A higher  $b$  value means that the viscosity has a stronger dependence on the the variation of temperature. Under the same processing conditions, the influence of activation energy on  $R(Z)$ ,  $H(Z)$ ,  $T(Z)$  and  $X(Z)$  profiles are shown as Figures 4-57 - 4-60, where  $b_1>b_2>b_3$ . For a fixed apparent heat transfer coefficient, since the apparent viscosity in the case of  $b_1$  increases the most quickly than that in the other two cases, the case of  $b_1$  has the largest radius and the thinnest film. The order of the radius and thickness for these three cases are  $R_3>R_2>R_1$  and  $H_1>H_2>H_3$ , respectively. Moreover, the different blow-up ratios will make the case of  $b_3$  have the lowest local temperature in the upper part of the bubble and the earliest development of crystallinity in the film.

#### (5) Influence of Crystallization Rate

Figures 4-61 through 4-64 show that the rate of crystallization affects the  $R(Z)$ ,  $H(Z)$ ,  $T(Z)$  and  $X(Z)$  profiles. At the beginning of building a bubble, there is no influence on the tubular film for different  $K$  values because of the temperature being still higher than the crystallization temperature  $T_c$  and no occurrence of crystallization. When temperature approaches the  $T_c$ , the



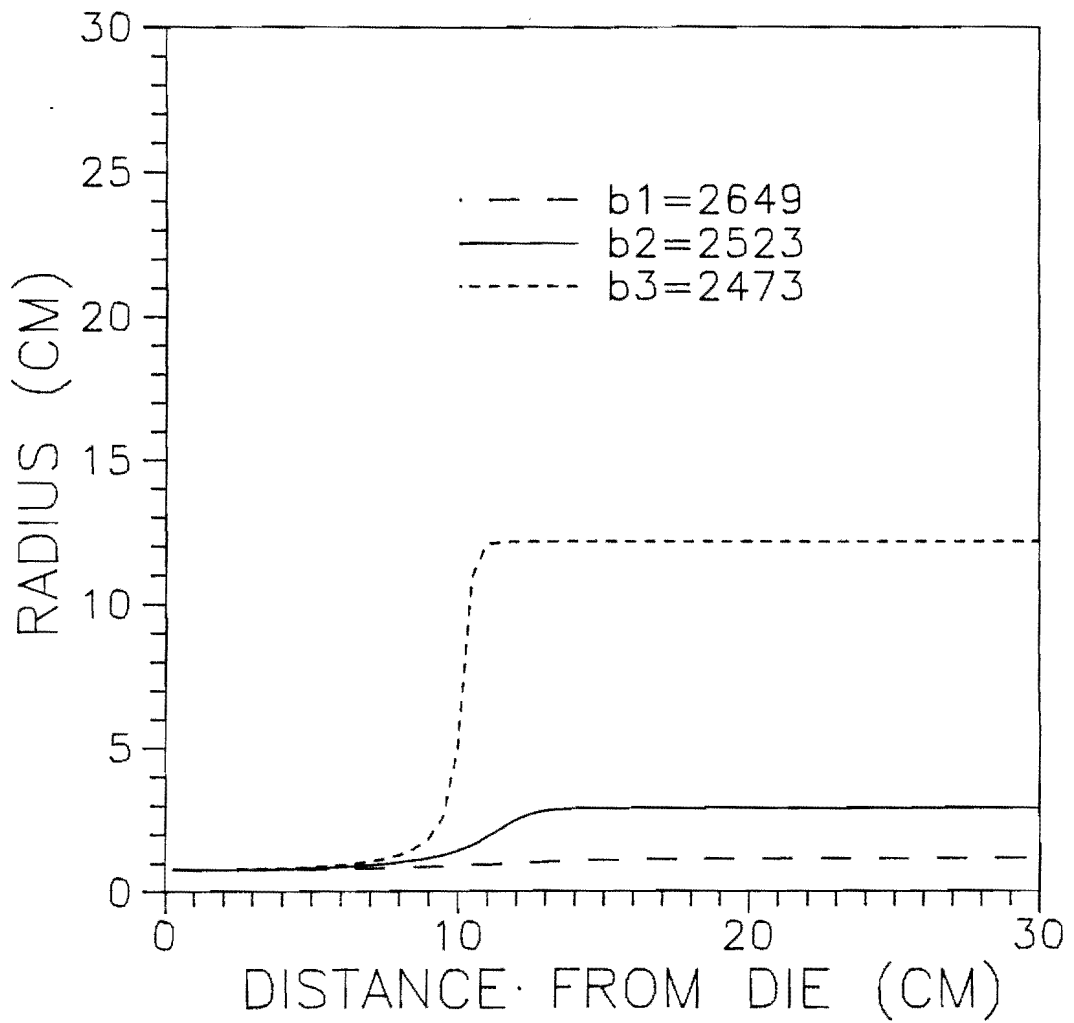


Figure 4-57 Comparison of the predicted radius profiles by the proposed model for different  $b$  values.

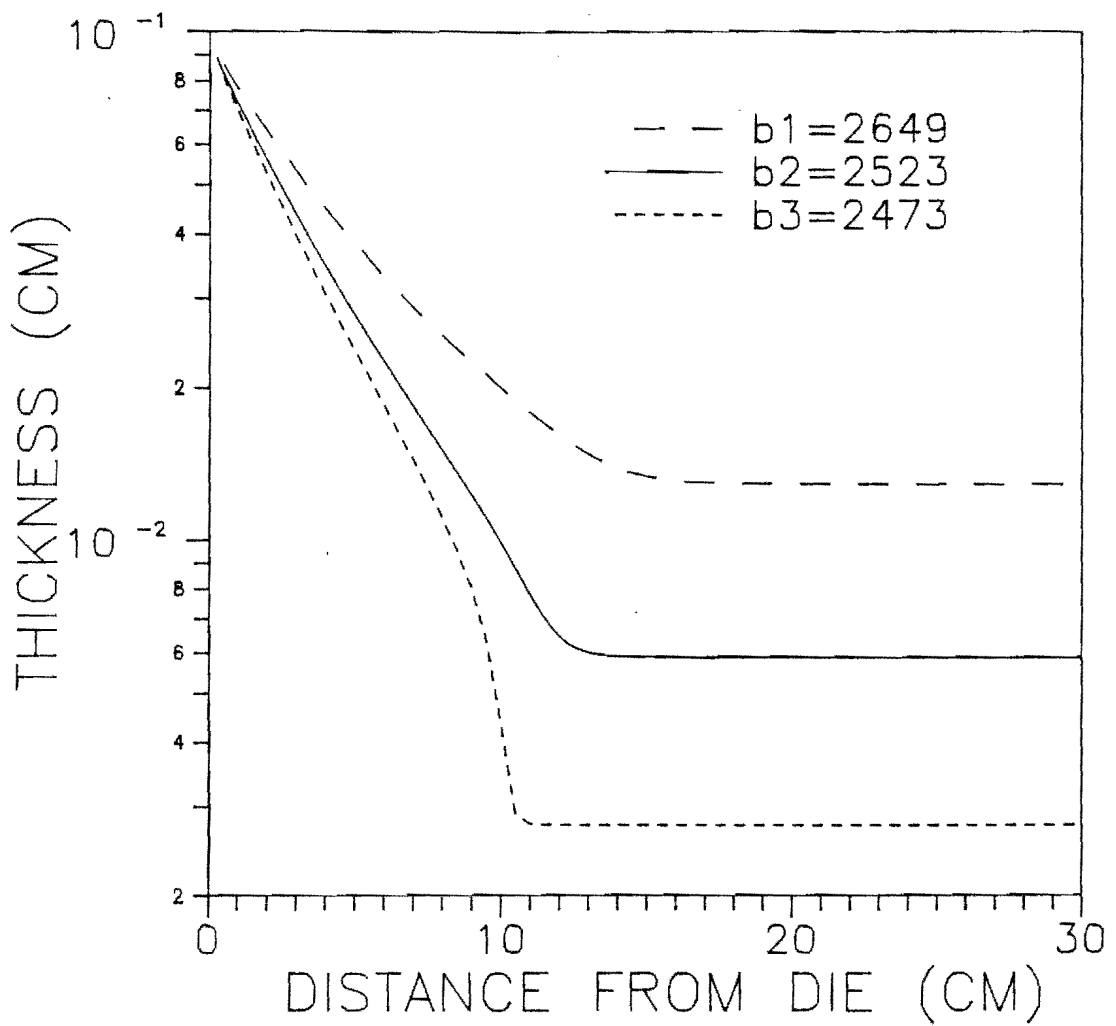


Figure 4-58 Comparison of the predicted thickness profiles by the proposed model for different  $b$  values.

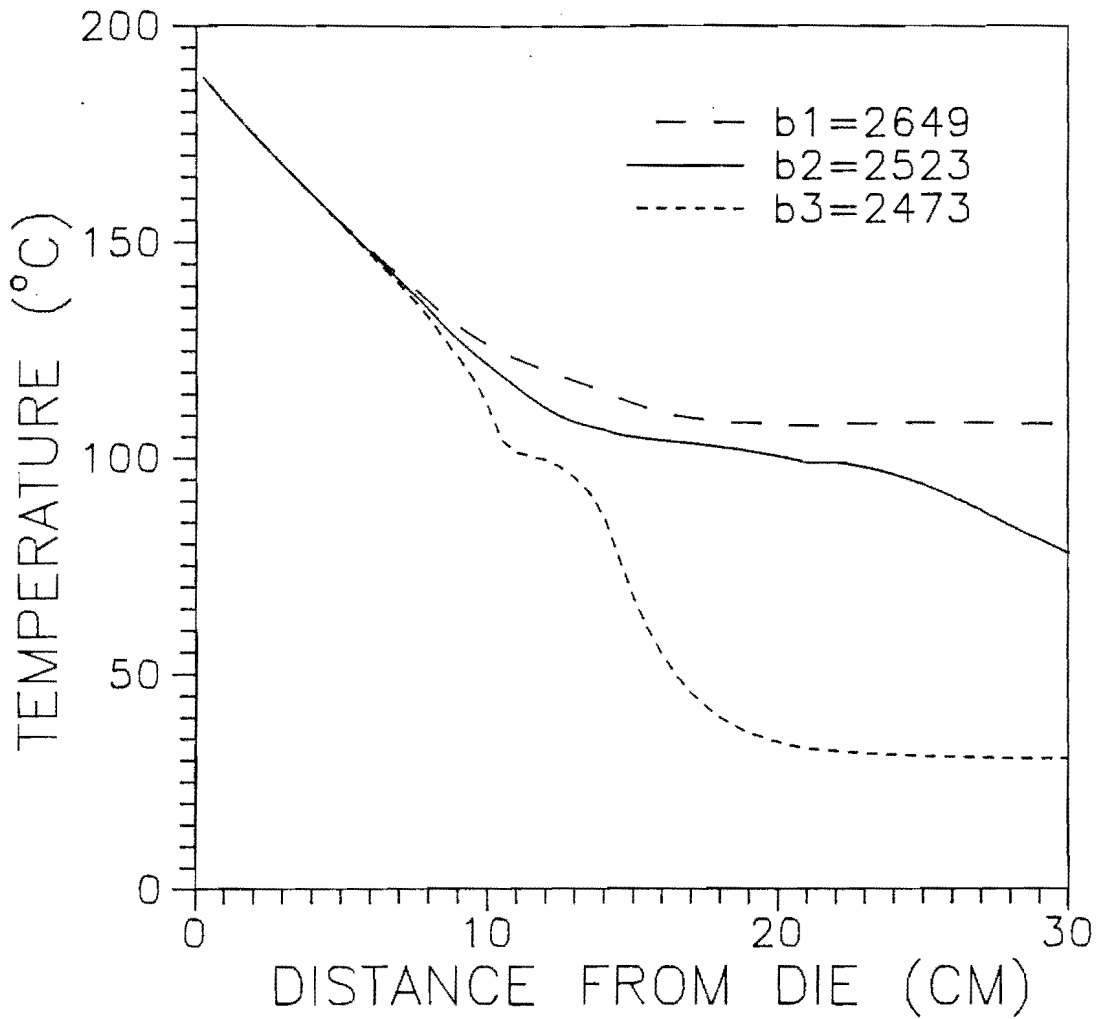


Figure 4-59 Comparison of the predicted temperature profiles by the proposed model for different  $b$  values.

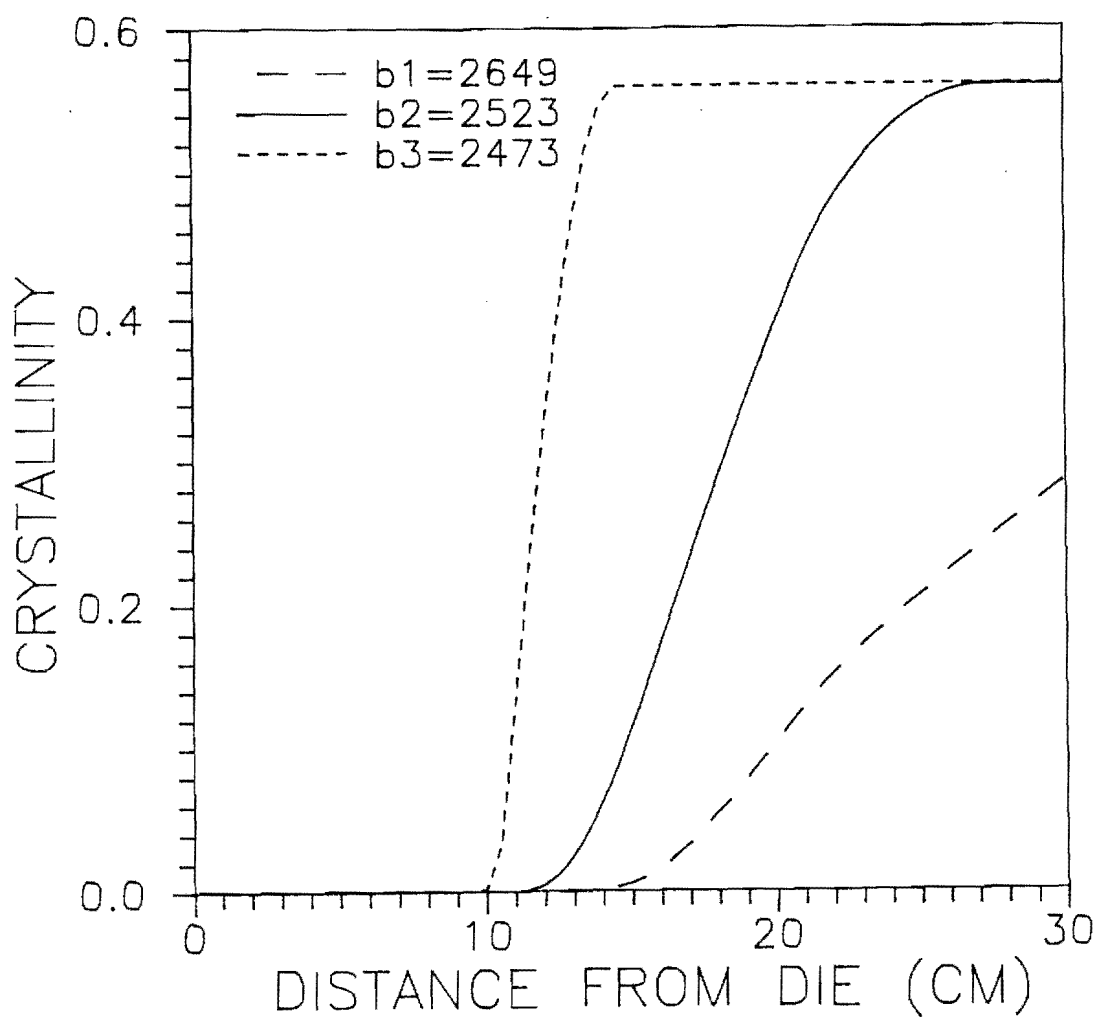


Figure 4-60 Comparison of the predicted crystallinity profiles by the proposed model for different  $b$  values.

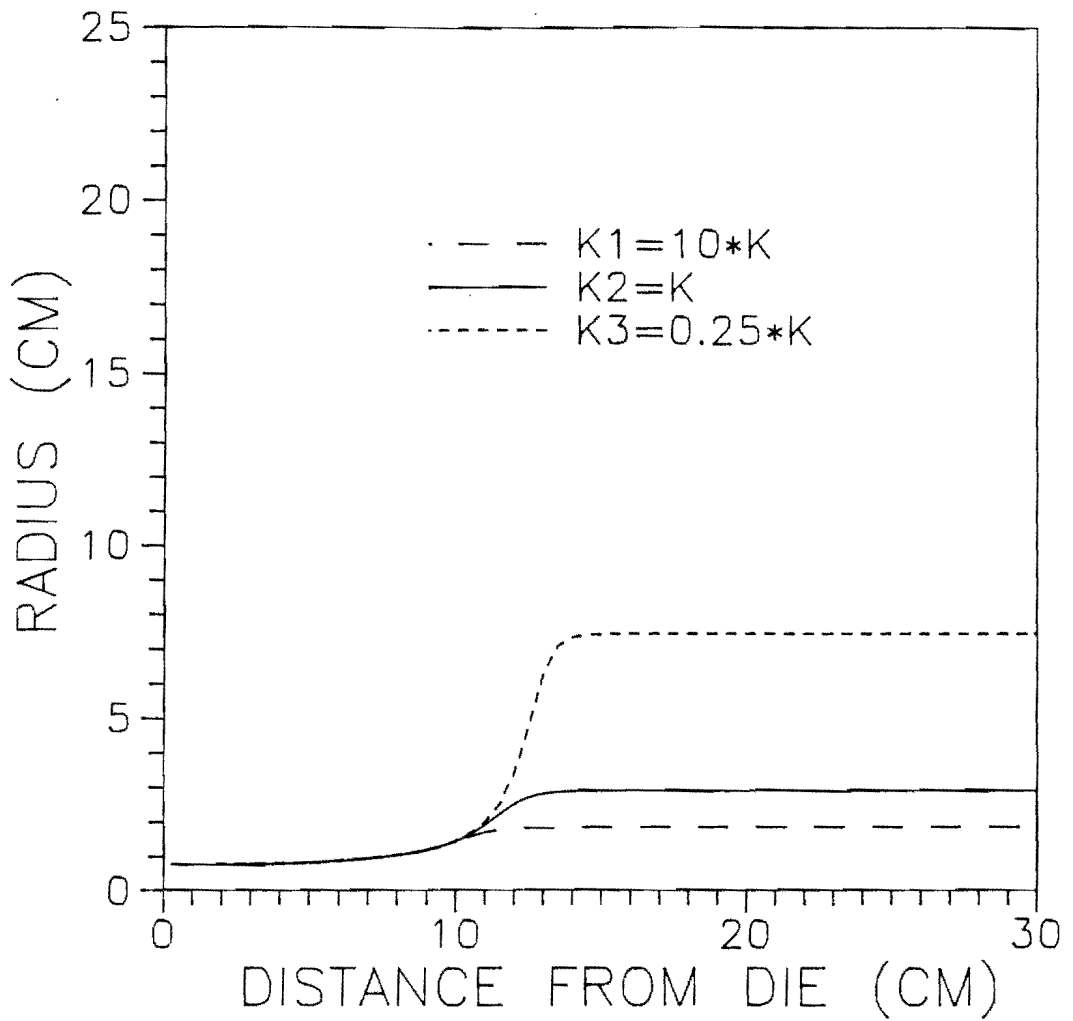


Figure 4-61 Comparison of the predicted radius profiles by the proposed model for different K values.

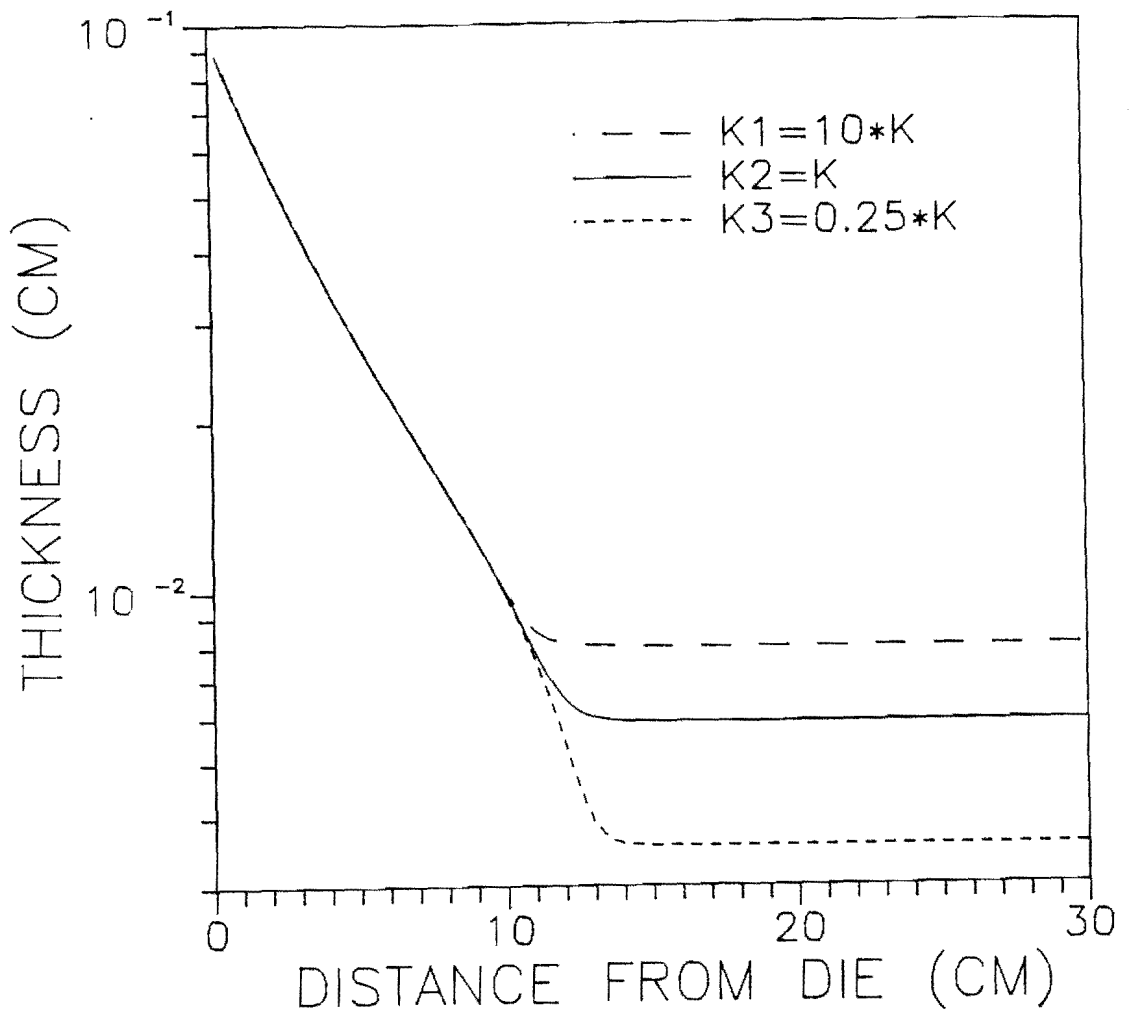


Figure 4-62 Comparison of the predicted thickness profiles by the proposed model for different K values.

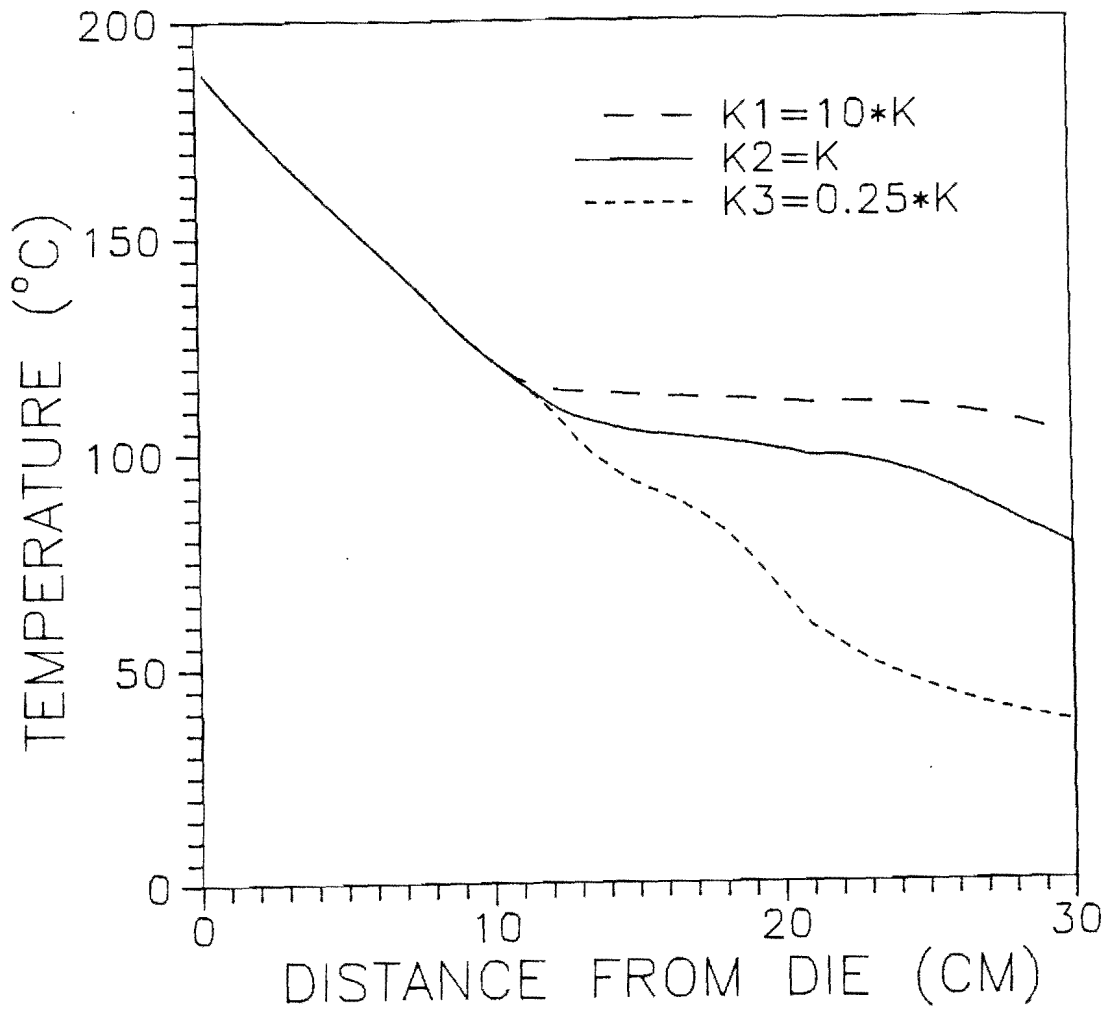


Figure 4-63 Comparison of the predicted temperature profiles by the proposed model for different K values.

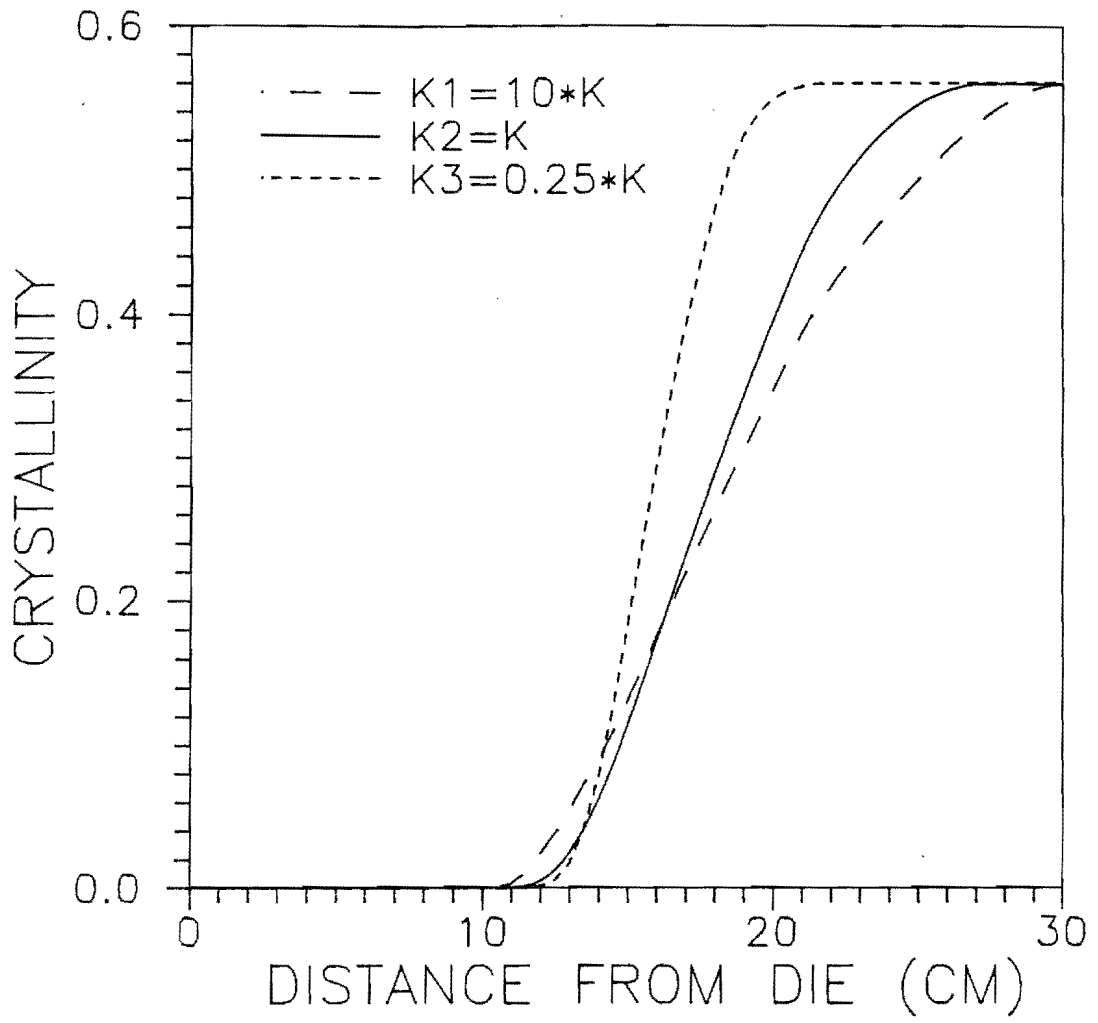


Figure 4-64 Comparison of the predicted crystallinity profiles by the proposed model for different K values.



higher K value causes faster formation of solid phase, which makes the apparent viscosity increase sharply and stops the deformation of R and H. Hence, for three different values of K ( $K_1 > K_2 > K_3$ ), we have  $R_3 > R_2 > R_1$  in Figure 4-61 and  $H_1 > H_2 > H_3$  in Figure 4-62. Nevertheless, although  $K_1 > K_2 > K_3$ , the theoretical prediction shows that the case of  $K_3$  achieves the final crystallinity most quickly, shown as Figure 4-64. It seems opposite to our intuitive expectation, but it is reasonable. The case of  $K_3$  has a higher heat convection and radiation due to its larger radius though  $K_3$  has the smallest crystallization rate. This explanation can be supported by the temperature profiles shown as Figure 4-63, in which the temperature profile for the case of  $K_3$  shows the highest cooling rate. Therefore, we can know that the degree of crystallinity during processing is not only decided by the value of K but also decided by the influences of crystalline phase on the rheological performance.

## CHAPTER 5

### SUMMARY AND CONCLUSIONS

The important conclusions from this study can be summarized as follows:

#### Experimental

(1) Since accurate on-line experimental data are essential to test the mathematical model for the tubular film blowing process, the measuring techniques were carefully studied, and their reliability was also examined. The results indicated that these measuring techniques were sufficiently accurate to make the collection of on-line data a useful analytical tool. Moreover, all of the on-line profiles (radius, thickness, velocity and temperature) showed their frost lines at the same position as observed by a change in the translucence of the bubble. It is noted that the above measurements of frost line are independent.

(2) A useful relationship between the emissivity and thickness of the film was generated by the on-line temperature measurement. For future work, combining the above empirical equation for the emissivity and on-line thickness

profile, the complicated procedures for monitoring the on-line temperatures could be simplified.

(3) Monitoring on-line temperature would be helpful in controlling the process because the temperature of the bubble strongly affects the rheological and crystallization process.

### Mathematical Analysis

(1) In 1970 Pearson and Petrie [3,4] set down equations for modeling the tubular film blowing process and their analysis has been used in all subsequent work. Two aspects of the theoretical predictions have caused difficulty, or at least are not fully understood. Firstly, a long initial "neck", i.e., a tubular film of nearly constant radius near the die, is observed experimentally for some materials under some conditions, but is not predicted correctly by the theory. And secondly, the theory predicts an "inverse" (i.e., counterintuitive) effect of internal air pressure on the blow-up ratio; that is, the theory predicts that increasing the pressure will cause the radius (the blow-up ratio) to decrease. Experimental observations on this point are mixed. Kanai and White [6,14] note an inverse effect both in their data and in the analysis, but do not attempt a physical interpretation. Han and Park [11] find both situations (radius increasing and decreasing with pressure), depending on the material; whereas Wagner [123] finds the "intuitive"

effect for most of his data (that is, increasing pressure showed an increase in radius), except a nearly constant pressure seemed to occur at blow-up ratios greater than about two. There was not any analysis, however, in either of these studies. Finally, in the present work a few qualitative observations showed the intuitive effect, but the effect of pressure is so sensitive as to cast doubt on the general validity of the conclusion.

(2) In an attempt to understand these two effects more thoroughly, especially the production of the long initial neck, a simplified theory has been formulated. The simplified theory is obtained from a direct physical argument by neglecting curvature effects in the force balance. Using it, the fit of theory to data for the initial neck is greatly improved.

(3) The simplified theory also produces a dimensionless grouping  $(F/\Delta P 4\pi R_0^2)$  which governs the nature of the subsequent film behavior. If this group is less than unity, the radius increases (i.e., the film blows-up); if it is equal to unity, the radius remains constant; and if it is greater than unity, radius decreases. The simplified theory also predicts the intuitive effect of pressure on radius. No quantitative evaluation of these various predictions was made in the present work, however. Testing such predictions, or

analogous predictions from a modified theory, should be an important objective of future studies.

(4) The general formulation of Pearson and Petrie does not reduce to the simplified theory of the present work, as it should. There is, then, a conceptual error (or inappropriate approximation) either in the general theory or in the simplified theory. In that regard it seems likely that the effect of pressure on radius (whether intuitive or inverse) will depend on variables other than pressure. The reconciliation of a general formulation (either that of Pearson and Petrie or a modified version of it) and suitable simplified theories (asymptotes) is an essential requirement of any future work in this area.

LIST OF REFERENCES

## LIST OF REFERENCES

1. R. R. Knittel, in "Modern Plastics Encyclopedia," R. J. Martino, Ed., Mc Graw-Hill, New York (1990).
2. R. A. Weeks, in "Modern Plastics Encyclopedia," R. J. Martino, Ed., Mc Graw-Hill, New York (1991).
3. J. R. A. Pearson, and C. J. S. Petrie, J. Fluid Mech., 40, 1 (1970).
4. J. R. A. Pearson, and C. J. S. Petrie, J. Fluid Mech., 42, 609 (1970).
5. C. D. Han and J. Y. Park, J. Appl. Polym. Sci., 19, 3277 (1975).
6. T. Kanai and J. L. white, J. Polym. Eng., 5, 135 (1985).
7. B. Cao, P. Sweeney and G. A. Campbell, ANTEC, New York, 35 (1989).
8. R. Farber and J. Dealy, Polym. Eng. Sci., 14, 435 (1974).
9. E. Fisher, Kunststoffe, 70, 541 (1980).
10. R. K. Gupta, A. B. Metzner and K. F. Wissbrun, Polym. Eng. Sci., 22, 172 (1982).
11. C. D. Han and J. Y. Park, J. Appl. Polym. Sci., 19, 3257 (1975).
12. C. D. Han and R. Shetty, Ind. Eng. Chem., Fundam., 16, 49 (1977).
13. T. A. Huang and G. A. Campbell, ANTEC, Washington, D.C. (1985).
14. T. Kanai and J. L. White, Polym. Eng. Sci., 24, 1185 (1984).
15. G. Menges and W. O. Predohl, Polym. Eng. Sci., 15, 394 (1975).

16. T. Nagasawa, T. Matsumura, S. Hoshino and K. Kobayashi, Appl. Polym. Symp. 20, 275 (1973).
17. H. H. Winter, Pure and Appl. Chem., 55, 943 (1983).
18. J. W. Taylor, in "Modern Plastics Encyclopedia," R. J. Martino, Ed., Mc Graw-Hill, New York (1991).
19. B. Cao and G. A. Campbell, AIChE. J., 36, 420 (1990).
20. J. R. A. Pearson, and C. J. S. Petrie, Plast. Polym., 38, 85 (1970).
21. C. J. S. Petrie, AIChE J., 21, 275 (1975).
22. J. R. A. Pearson, "Mechanical Principles of Polymer Melt Processing", Pergamon Press, London (1966).
23. K. J. Choi, J. L. White and J. E. Spruiell, J. Appl. Polym. Sci., 25, 2777 (1980).
24. T. Alfrey, S. P. E. Trans., 5, 68 (1965).
25. C. J. S. Petrie, Rheol. Acta, 12, 92 (1973).
26. W. Ast, Kunststoffe, 63, 427 (1973).
27. W. Ast, Kunststoffe, 64, 146 (1974).
28. R. Farber, M. Eng. thesis, Mc Gill University, Montreal (1973).
29. V. V. Nonozhilov, "The Theory of Thin Shells", Noordhoff, Groningen (1959).
30. P. A. Small, Ad. Polym. Sci., 18, 1 (1975).
31. F. J. Bueche, Chem. Phys., 40, 484 (1964).
32. T. G. Fox and P. J. Flory, J. Am. Chem. Soc., 70, 2384 (1948).
33. T. G. Fox and P. J. Flory, J. Phys. Chem., 21, 581 (1950).
34. G. Atalla and D. Romanini, Rheo. Acta, 22, 471 (1983).
35. D. Constantin, Polym. Eng. Sci., 24, 268 (1984).



36. D. Acierno, D. Curto, F. P. La Mantia and A. Valenza, *Polym. Eng. Sci.*, 26, 28 (1986).
37. F. P. La Mantia and D. Acierno, *Polym. Eng. Sci.*, 25, 279 (1985).
38. C. D. Han, Y. J. Kim, H. K. Chuang and T. H. Kwack, *J. Appl. Polym. Sci.*, 28, 3435 (1983).
39. C. D. Han and T. H. Kwack, *J. Appl. Polym. Sci.*, 28, 3399 (1983).
40. T. H. Kwack and C. D. Han, *J. Appl. Polym. Sci.*, 28, 3419 (1983).
41. R. I. Tanner, "Engineering Rheology," Clarendon Press, Oxford (1985).
42. S. Middleman, "Fundamental of Polymer Processing", Mc Graw Hill, New York (1977).
43. D. Acierno, J. N. Dalton, J. M. Rodriguez and J. L. White, *J. Appl. Polym. Sci.*, 15, 2395 (1965).
44. I. Chen, G. E. Haggler, L. E. Abbott, J. N. Dalton, D. C. Bogue, and J. L. White, *Trans. Soc. Rheol.* 16, 473 (1972).
45. C. D. Han and R. R. Lamonte, *Trans. Soc. Rheol.*, 16, 447 (1972).
46. C. D. Han and L. Segal, *J. Appl. Polym. Sci.*, 14, 2973 (1970).
47. M. Zida, *Rheol. Acta*, 8, 89 (1969).
48. C. D. Han, "Rheology in Polymer Processing," Academic Press, New York (1976).
49. H. Yamane, Ph.D. Dissertation, University of Tennessee, Knoxville, 1985.
50. T. Kanai, *Intern. Polymer Processing*, 1, 137 (1987).
51. C. J. S. Petrie, *Plast. Polym.*, 42, 259 (1974).
52. G. Menges and W. Predohl, *Plastverarbeiter Bd.*, 23, 338 (1972).

53. E. R. G. Eckert and R. M. Drake, "Heat and Mass Transfer," 2nd ed., Mc Graw-Hill, New York (1959).
54. J. R. Holman, "Heat Transfer," 5th ed., Mc Graw-Hill, New York (1981).
55. J. Frenkel, J. Physics, 1, 315 (1939).
56. D. Turnbull and J. E. Fisher, J. Chem. Phys., 17, 71 (1949).
57. J. D. Hoffman and J. I. Lauritzen, J. Res. Natl. Bur. Stds., 65A, 297 (1961).
58. L. Mandelkern, F. A. Quinn and P. J. Flory, J. Appl. Phys., 25, 830 (1954).
59. F. P. Price, in "Nucleation," Zettlemayer, Marcel and Dekker Ed., New York (1969).
60. D. Turnbull, J. Chem. Phys., 20, 411 (1952).
61. J. D. Hoffman and J. J. Weeks, J. Chem. Phys., 37, 1721 (1962).
62. M. L. Williams, R. F. Landel and J. D. Ferry, J. Amer. Chem. Soc., 77, 3701 (1955).
63. D. C. Bassett, "Principles of Polymer Morphology," Cambridge University Press, Oxford (1981).
64. M. J. Avrami, J. Chem. Phys., 7, 1103 (1939).
65. M. J. Avrami, J. Chem. Phys., 8, 212 (1940).
66. M. J. Avrami, J. Chem. Phys., 9, 177 (1941).
67. L. Mandelkern, "Crystallization of Polymers," Mc Graw-Hill, New York (1964).
68. T. Kawai, M. Iguchi and H. Tonami, Kolloid Z. Z., 221, 28 (1967).
69. V. G. Wilhelm, Kolloid Z. Z. Polym., 208, 97 (1966).
70. K. J. Nakamura, J. Appl. Polym. Sci., 16, 1077 (1972).
71. K. J. Nakamura, J. Appl. Polym. Sci., 17, 1031 (1972).

72. K. J. Nakamura, *J. Appl. Polym. Sci.*, 18, 615 (1974).
73. A. Ziabicki, *Polimery*, 12, 405 (1967).
74. A. Ziabicki, *J. Chem. Phys.*, 48, 4368 (1968).
75. A. Ziabicki, *J. Chem. Phys.*, 48, 4374 (1968).
76. A. Ziabicki, *Polimery*, 18, 615 (1973).
77. A. Ziabicki, "Fundamentals of Fiber Formation," Interscience, New York (1976).
78. H. P. Nadella, M. M. Henson, J. E. Spruiell, and J. L. White, *J. Appl. Polym. Sci.*, 21, 3003 (1977).
79. K. Kobayashi and T. Nagasawa, *J. Macromol. Sci.* B4, 331 (1970).
80. J. D. Hoffman, G. T. Davis and J. I. Lauritzen, in "Treatise on Solid State Chemistry," Vol. 3, N. B. Hannay Ed., Plenum, New York (1976).
81. K. Katayama and M-G. Yoon, in "High Speed Fiber Spinning," Wiley, New York, 1985.
82. J. Zhou, M.S. Thesis, University of Tennessee, Knoxville, 1988.
83. D. R. Holmes and R. P. Palmer, *J. Polym. Sci.*, 31, 345 (1958).
84. P. H. Lindenmeyer and S. Lustig. *J. Appl. Sci.*, 9, 227 (1965).
85. W. F. Maddams and J. E. Preedy, *J. Appl. Polym. Sci.* 22, 2721 (1978).
86. W. F. Maddams and J. E. Preedy, *J. Appl. Polym. Sci.* 22, 2739 (1978).
87. W. F. Maddams and J. E. Preedy, *J. Appl. Polym. Sci.* 22, 2751 (1978).
88. K. J. Choi, J. E. Spruiell and J. L. White *J. Polym. Sci.: Polym. Phys. Ed.* 20, 27 (1982).

89. J. R. Dees and J. E. Spruiell, *J. Appl. Polym. Sci.*, 18, 1053 (1974).
90. C. D. Han and J. Y. Park, *J. Appl. Polym. Sci.*, 19, 3291 (1975).
91. W. Minoshima and J. L. White, *J. Non-Newtonian Fluid Mech.*, 19, 275 (1986).
92. J. J. Cain and M. M. Denn, *Polym. Eng. Sci.*, 28, 1527 (1988).
93. Y. L. Yeow, *J. Fluid Mech.*, 75, 577 (1976).
94. X. L. Luo and R. I. Tanner, *Polym. Eng. Sci.*, 25, 620 (1985).
95. M. H. Wagenr, *Rheol. Acta*, 15, 40 (1976).
96. R. K. Gupta, Ph.D. Thesis, University of Delaware (1981).
97. W. Minoshima, Ph.D. Dessertation, University of Tennessee, Knoxville, 1983.
98. T. A. Huang and G. A. Campbell, *Advances in Polymer Technology*, 5, 181 (1985).
99. M. Pivovonsky and M. R. Nagel, "Tables of Blackbody Radiation Functions," Macmillan, New York (1961).
100. N. Hajji, Ph.D. Proposal, The University of Tennessee, Knoxville, May (1989).
101. Operation for PROBEYE Thermal Video System Series 3000, Hughes Aircraft Company.
102. D. Halliday and R. Resnick, "Fundamentals of Physics," Revised Ed., John Wiley & Sons, Inc., New York, 1974.
103. J. L. Lambach, M.S. Thesis, University of Tennessee, Knoxville, 1988.
104. F. Grum and R. J. Becherer, "Optical Radiation Measurements, Vol. 1, Radiometry," Academic Press, New York (1979).
105. J. Brandrup and E. H. Immergut, *Polymer Handbook*, 3rd Ed., John Wiley & Sons, Inc., New York (1989).

106. IRCON, Inc., Plastic Film Measurement, Technical Notes (1979).
107. H. H. George and M. H. G. Deeg, Paper presented at the Second Annual Meeting of the International Polymer Processing Society, Montreal, Canada (1986).
108. J. H. Bheda, Ph.D. Dissertation, University of Tennessee, Knoxville, 1987.
109. L. S. Hood, M.S. Thesis, University of Tennessee, Knoxville, 1990.
110. J. Zhou and N. Hajji, unpublished work, University of Tennessee, Knoxville, 1990.
111. R. M. Patel, J. H. Bheda and J. E. Spruiell, J. Appl. Polym. Sci., 42, 1671 (1991).
112. R. G. Griskey and G. N. Foster III, S. P. E. Ann. Tech. Conf., 26, 546 (1968).
113. L. Mandelkern, Rubber. Chem. Technol., 32 (1959).
114. R. F. Westover, in "Processing of Thermoplastic Material," E. C. Bernhardt Ed., Kreiger, New York (1974).
115. G. T. Davis, R. K. Eby and J. P. Colson, J. Appl. Phys., 41, 4316 (1970).
116. R. B. Bird, W. E. Stewart and E. N. Lightfoot, "Transport Phenomena," John Wiley & Sons, New York (1971).
117. B. Wunderlich and M. Dole, J. Polym. Sci., 24, 201 (1957).
118. T. Kikutani, Ph.D. Dissertation, Tokyo University of Technology, 1982.
119. F. T. Trouton, Proc. R. Soc., A77, 426 (1906).
120. K. F. Zieminski and J. E. Spruiell, J. Appl. Polym. Sci., 35, 2223 (1988).
121. K. H. Illers and H. Hendus, Makromol. Chem., 113, 1 (1968).

122. J. C. Butcher, "Numerical Analysis of Ordinary Differential Equations," John Wiley & Sons, New York (1987).
123. M. H. Wagner, *Kunststoffe*, 68, 362, (1978).

## VITA

Cheng-Chien Liu (劉誠健) was born in Taiwan, Republic of China, on October 19, 1963. From September 1981 to June 1985, Mr. Liu studied in the Chemical Engineering Department at the Tatung Institute of Technology in Taipei, Taiwan and received a Bachelor degree. During his undergraduate studies, he won several scholarships, including Chinese Technical Service Association Scholarship and Teacher's Project Scholarship of the Tatung Institute of Technology. Fulfilling the military service in Taiwan, he served as a Second Lieutenant in the Chinese Garrison Commander from 1985 to 1987, and then he worked as a teaching assistant at the Tatung Institute of Technology for one year.

In the fall of 1988, he left Taiwan and began his graduate studies toward the Master of Science in Polymer Engineering at the University of Tennessee, Knoxville. While in that program, he also worked as a research assistant in the Department of Materials Science and Engineering. The Master's degree was awarded in August 1991.

Mr. Liu is a member of the Society of Plastic Engineers. After graduation, he will continue study toward the Ph.D. degree at the University of Tennessee, Knoxville.